

University of Wollongong - Research Online

Thesis Collection

Title: Electronic and Optical Properties of Graphene

Author: Anthony Wright

Year: 2010

Repository DOI:

Copyright Warning

You may print or download ONE copy of this document for the purpose of your own research or study. The University does not authorise you to copy, communicate or otherwise make available electronically to any other person any copyright material contained on this site.

You are reminded of the following: This work is copyright. Apart from any use permitted under the Copyright Act 1968, no part of this work may be reproduced by any process, nor may any other exclusive right be exercised, without the permission of the author. Copyright owners are entitled to take legal action against persons who infringe their copyright. A reproduction of material that is protected by copyright may be a copyright infringement. A court may impose penalties and award damages in relation to offences and infringements relating to copyright material.

Higher penalties may apply, and higher damages may be awarded, for offences and infringements involving the conversion of material into digital or electronic form.

Unless otherwise indicated, the views expressed in this thesis are those of the author and do not necessarily represent the views of the University of Wollongong.

Research Online is the open access repository for the University of Wollongong. For further information contact the UOW Library: research-pubs@uow.edu.au

University of Wollongong Thesis Collections

University of Wollongong Thesis Collection

University of Wollongong

Year 2010

Electronic and Optical Properties of Graphene

Anthony Wright
University of Wollongong

Wright, Anthony, Electronic and Optical Properties of Graphene, Doctor of Philosophy thesis, School of Engineering Physics, University of Wollongong, 2010.
<http://ro.uow.edu.au/theses/3123>

This paper is posted at Research Online.

NOTE

This online version of the thesis may have different page formatting and pagination from the paper copy held in the University of Wollongong Library.

UNIVERSITY OF WOLLONGONG

COPYRIGHT WARNING

You may print or download ONE copy of this document for the purpose of your own research or study. The University does not authorise you to copy, communicate or otherwise make available electronically to any other person any copyright material contained on this site. You are reminded of the following:

Copyright owners are entitled to take legal action against persons who infringe their copyright. A reproduction of material that is protected by copyright may be a copyright infringement. A court may impose penalties and award damages in relation to offences and infringements relating to copyright material. Higher penalties may apply, and higher damages may be awarded, for offences and infringements involving the conversion of material into digital or electronic form.

Electronic and Optical Properties of Graphene



Anthony Wright

University of Wollongong

A thesis submitted for the degree of

Doctor of Philosophy

Certification

I, Anthony R. Wright, declare that this thesis, submitted in partial fulfilment of the requirements for the award of Doctor of Philosophy, in the School of Engineering Physics, University of Wollongong, is wholly my own work unless otherwise referenced or acknowledged. The document has not been submitted for qualifications at any other academic institution.

Anthony R. Wright

Contents

Certification	i
List of Figures	iv
Dedication	xiii
List of Publications	xvi
Acknowledgements	xix
Introduction	1
1 Electronic Properties of Graphene	16
1.1 Single Layer Graphene (SLG)	18
1.1.1 Full Energy Description	19
1.1.2 Low Energy Approximation	21
1.2 Bilayer Graphene (BLG)	23
1.3 Graphene Nanoribbons (GNRs)	26
1.4 Bilayer Graphene Nanoribbons (BLGNRs)	30
1.5 Stretched Single Layer Graphene	34
1.6 Conclusion	38
2 Dielectric Properties of Graphene Systems	40
2.1 Dielectric Function	40
2.2 Collective Excitation Spectra of Armchair Graphene Nanoribbons	43

3	Optical Conductivity of Graphene	49
3.1	Single Layer Graphene	51
3.2	Bilayer Graphene	52
3.3	Graphene Nanoribbons	59
3.4	Layered Graphene Nanoribbons	60
3.5	Stretched Graphene	67
3.6	Conclusions	72
4	Nonlinear Optical Conductivity of Graphene	73
4.1	Formalism	73
4.2	Results	75
4.2.1	Temperature Dependence of Results	82
5	High Frequency Conductivity of Graphene	88
5.1	Phonon Spectrum	89
5.2	Many Particle Formalism	91
5.3	Momentum Frequency Summation (ξ_l)	95
5.3.1	Diagrams two and three	96
5.4	Form Factor Determination	99
5.5	Momentum Transfer Summations (α_m)	101
5.6	Results and Discussions	102
5.7	Conclusion	108
	Conclusion	109
	Bibliography	112

List of Figures

1	The fermions in graphene are described by the conical massless Dirac dispersion which is a low energy manifestation of an ultra-relativistic equivalent dispersion. The fermions in bilayer graphene have no known equivalent, and can be described as massive chiral fermions with a symmetrical bandstructure.	5
2	The proposed setup to demonstrate the Klein paradox. An incoming Dirac Fermion hits a finite potential well of magnitude V_0 and width D . The transmission is calculated as usual in elementary quantum mechanics by demanding the continuity of the wavefunctions. Figure from reference (1)	6
3	The transmission results from equation 7 for different values of V_0 , where $D = 110\text{nm}$ (top), and $D = 50\text{nm}$ (bottom). Aside from normal incidence there are potentially other points of absolute transmission as well. This absolute transmission is a manifestation of the Klein paradox. Figure from reference (1)	7
4	Laughlin's proposed experiment to probe the quantum Hall effect in graphene. He suggested a carbon nanotube type configuration with a magnetic field passing through the surface of the tube, and a current passing circumferentially around the tube such that there is a flux ϕ down the axis of the tube, and a Hall voltage V_H is induced perpendicular to the field. Figure from reference (1) . . .	9

5	The measurement of the anomalous integer Quantum Hall Effect for graphene. As reasoned by several authors, there is no Hall plateau at $N = 0$. The peak of the blue line at $n = 0$ shows that there is a Landau level when the chemical potential at the neutrality point which draws states equally from the conduction and valence bands. Figure from reference (1)	10
6	The measurement of the universal conductivity of graphene performed by Nair et al and published in Science magazine ???. Amazingly, the universal conductivity is directly proportional to the fine structure constant, and provides an alternative (albeit less accurate) method for determining it.	11
7	The optical conductivity of graphene outside the Dirac regime contains significant structure which is lost when confined to the linear approximation to the Hamiltonian. The peak corresponds to a van-Hove singularity in the density of states. The full energetic range is $0 < \hbar\omega < 9\text{eV}$. The Dirac formalism is roughly applicable up to $\approx 1\text{eV}$	12
1.1	Single layer graphene contains two atoms per unit cell, generally denoted by A and B. The first nearest neighbour vectors are shown ($\hat{\delta}_i$), as well as the lattice vectors (\mathbf{a}_{\pm}). The electronic structure is investigated via the tight binding approximation.	18
1.2	The three interlayer terms included in the BLG Hamiltonian, as well as the next nearest neighbour coupling term. γ_2 and γ_3 differ in that they connect, respectively, different and equivalent points in the SLG Brillouin Zone. Whilst γ_1 and γ_2 both represent coupling between different sites in the Brillouin zone, γ_1 is a directly vertical transition, and so the overlap of the wavefunctions is much larger ($\approx 3\times$ larger)	24
1.3	The k_x dependence of the bandstructure near the K/K' points with all coupling terms included. The two arrows show the approximately constant (at low energies) gap between similar bands.	25

1.4	The k_x dependence of the two inner bands near the K/K' points zoomed right in to see the effects of γ_2 and γ_3 . The NNN interaction has shifted these features well below the Fermi level. γ_2 causes the second dirac point to emerge, and γ_3 causes one of the two Dirac points to occur at a lower energy.	25
1.5	The two most typical GNRs are $q = 0$, corresponding to zig-zag ribbons, and $q = 1$, corresponding to armchair ribbons. The elegance of Ezawa's construction is the simplicity of constructing infinite ribbons by placing consecutive stacks of hexagon layers on top of each other, offset by q hexagons. The zig-zag and armchair edges can be readily seen. These are what determine the unique electronic properties of each class of ribbon. The index p essentially determines the width, and does not alter the electronic properties <i>as much</i> as q	26
1.6	(a) A typical zig-zag nanoribbon bandstructure ($p = 2$). Note that at the brillouin zone edges the energy gap becomes zero. This is the case for all ZZ-GNRs. The linear Dirac dispersion is, however, not present, in these structures. (b) A typical armchair nanoribbon bandstructure ($p = 2$). The low energy linear Dirac dispersion occurs in armchair ribbons where $p + 1 \subset N$. For all other AC-GNRs, there is a small band gap. (c) A $\langle 3, 3 \rangle$ chiral GNR. A small number of GNRs with $q > 1$ have a linear Dirac-like dispersion with no energy gap, but in general this will not be the case, and the bandgaps and curvature of the bands will vary dramatically from ribbon to ribbon.	28
1.7	A selection of armchair and zig-zag lgnrs with the two distinct possible stacking orientations. These cause different edge sites to couple between layers in slightly different ways, leading to subtle changes in the electronic bandstructure.	30

1.8	The bandstructures for the high symmetry bilayer ribbons ($q = 0, 1$), with $p = 2$. In general, when going from a single to a bilayer ribbon, each single layer subband becomes a subband pair which are separated from each other by some amount determined by the interlayer edge state coupling. Note in particular the key differences depending on stacking orientation are at the K and Γ points.	32
1.9	The effect of stretching on the three nearest neighbour bond directions when F is applied along various high symmetry directions. The dotted lines in b,c and d are the regular unstretched orientations. The magnitude of F has been chosen to be very large ($F \approx 15$) to emphasise the effect of stretching, however our numerical results will only go as high as $F = 2.5$	36
2.1	A hand waving approach to the screened interaction of an electronic system. The infinite sum of intermediate interactions leads to a denominator which is the RPA dielectric function of the system.	41
2.2	The collective excitation spectrum for Dirac armchair ($q = 1$) ribbons. The linear behaviour akin to collective excitation in metals is present for low widths, and low momentum transfers, as expected. At higher transfers and widths, the non-metallic subbands are no longer suppressed and cause the spectra to become curved.	44
2.3	Top: The collective excitation spectrum for non-Dirac armchair ($q = 1$) ribbons. The roton mode emerges here for $p = 18$, and for $p \geq 21$ there is a region where no excitations occur. Bottom: The frequency and wavevector dependent intensity distribution for a non-Dirac armchair (19,1) ribbon.	45

2.4	The dielectric function of the armchair ribbon exhibiting a roton mode is shown here for two values of $\hbar\omega/t$. (a) is that for $\hbar\omega/t = 0.35$ which is within the roton section of the spectrum. The two excitation peaks are clearly visible. For higher energies, the imaginary part is no longer negligible, and suppresses the excitations. This is seen in (b) where $\hbar\omega/t = 1$. Note that the collective excitation peaks have been normalized by the maximum magnitude of the real and imaginary parts of ϵ	47
3.1	The single loop diagram descibing the linear optical conductivity in the absence of interactions.	50
3.2	The k_x dependence of the bandstructure near the K/K' points. The effect of the NNN coupling is to shift the Fermi level (here $\epsilon_F = 0$) off the bands-crossing points. The other noticeable effect here is that of the dominant interlayer coupling γ_1 which causes the gap of $\Delta \approx \gamma_1$ between similar bands. The red dashed arrow represents a transition which is permitted in an intrinsic bilayer calculation if NNN coupling is neglected in the model, but becomes forbidden when it is included. The black solid arrow is the opposite: a previously forbidden transition becomes allowed when NNNs are included in the model. The effect of doping is to raise or lower the Fermi level, making the inclusion of NNNs partly equivalent to doping.	57
3.3	The optical conductance (in units of $\sigma_1 = e^2/\hbar$) vs the normalized frequency $\Omega = \hbar\omega/t$ for bilayer graphene. Generally, σ_{xx} (the zigzag direction) has a larger optical response than σ_{yy} (the armchair direction). When NNN and γ_4 are neglected, and at low energies, $\sigma_{xx} = \sigma_{yy}$. This is no longer the case here, with NNNs and γ_4 included. The grey shaded area indicates the low energy region plotted in Fig.3.4.	57

3.4	<p>The low energy optical conductance at two different doping levels. The blue dash-dot and black dashed lines are the optical conductance of intrinsic BLG along the x and y directions respectively. The black solid and blue dotted lines represent the optical conductance of a sample which is doped such that the chemical potential is shifted to the bands crossing point. The NNN-γ_4 coupling causes a new peak to emerge, and suppresses the previously reported one. This new peak is much larger and shifted to a lower photon energy. In a suitably doped sample, however, the $t' = 0$ (no NNN) peak has been retrieved by an effective shifting of the Fermi level. The inset shows the sensitivity of the intrinsic zig-zag peak to the Fermi energy. Δ is the bands crossing point. If the Fermi energy lies at least $0.6t'$ from the bands-crossing points (in either direction), the peak conductance lies within 15% of our result.</p>	58
3.5	<p>The optical conductivity for the ZZ-BLGNR (a) and the AC-BLGNR (b). The low energy activity in the bilayer ribbons is particularly significant, especially in the Dirac AC-BLGNR where the optical conductivity is approximately $150\sigma_0$. The temperature dependence of the large peak observed in all armchair bilayer ribbons is shown in the inset. The peak is robust all the way up to room temperature, decreasing rapidly to $\approx 80\sigma_0$ at $10K$ then decreasing very slowly with increasing energy.</p>	61
3.6	<p>The width dependence of the energy of the low-energy peak for BLGNRs with $q = [1, 4]$. The strongest peaks occur in the lowest energy gaps in the Dirac armchair ribbons. The inset shows the width dependence of the band gap for Dirac BLGNRs with strong low energy optical response. This gap eventually disappears, but in the 2D limit with no edges, it re-emerges at γ.</p>	63

3.7	The p dependence of the low energy peaks for a (p,1) BLG NR. In Dirac ribbons the symmetric transitions are suppressed and the non-symmetric ones dominate. For non-Dirac ribbons the opposite is the case. Notice that the strength of the peak in the Dirac cases is constant (within the specified computational accuracy of the calculation).	64
3.8	The width dependence of the magnitude of the low energy peak for the ZZ-BLG NRs decreases quickly with increasing width, and then increases steadily for $p > 6$	65
3.9	The stretching induced anisotropy in the longitudinal conductivity for three small pseudo force values. These correspond to bond stretching angles of $\approx 0.4, 1.2, 2$ degrees for $F = 0.5, 1.5, 2.5$ respectively. Despite the relatively small stretching angle, the induced anisotropy is as much as 10%. The angular dependence of this quantity is quite well behaved. When stretching along the zig-zag direction, the zig-zag longitudinal conductivity is increased, and similarly for stretching along the armchair direction. For stretching of $\pi/4$, the system remains isotropic.	69
3.10	The transverse optical conductivity as a function of stretching angle. Interestingly, even though the C_3 symmetry is broken for stretching along the high symmetry directions, the transverse conductivity remains zero. For chiral stretching this is not the case. Maximum stretching is reached for the longitudinally isotropic value of $\phi = \pi/4$	70
3.11	The transverse (Hall) conductivity for $\phi = 45^\circ$ and $F = 2.5$. The transverse conductivity reaches a maximum of $\approx 0.85\sigma_0$ at the high density of states saddle point $\Omega = 2$	71
4.1	A schematic illustration of linear and nonlinear optical processes in intrinsic graphene. The universal conductance described by \mathbf{J}_1 . The two third order terms $\mathbf{J}_3(\omega)$ and $\mathbf{J}_3(3\omega)$ are shown in blue and green colour. The latter is a frequency tripling term which is the dominant nonlinear current.	75

LIST OF FIGURES

4.2	The frequency dependent nonlinear current. Both the single frequency and frequency tripling terms decrease as ω^{-4} , and also with increasing temperature. At low frequencies, low temperatures, and sufficiently high field strengths, the nonlinear terms will contribute to the optical conductance of graphene. In particular, the single frequency term will abolish the universality of the ‘universal conductance’ under the right conditions.	85
4.3	(a) The difference between the critical fields at 0K and 300K as a function of frequency (ie. $\Delta E_c = E_c(0K) - E_c(300K)$). There is a maximum discrepancy for each nonlinear contribution which indicates the frequency where thermal effects are most significant. (b) The temperature dependence of the critical field strength at fixed frequency. At low temperatures the single frequency nonlinear current dominates over the frequency tripling term. At $\approx 180K$ however, the situation is reversed such that at room temperature, the frequency tripling term is the dominant nonlinear contribution.	87
5.1	The fourth nearest neighbours for graphene. We include up to fourth nearest neighbours so that the bond-bending effect of the third and fourth neighbours will be included.	90
5.2	The phonon spectrum of graphene obtained using the fourth nearest neighbour force constant tensor method.	91
5.3	The five diagrams which contribute to the high frequency correction to the optical conductivity.	93
5.4	The effective interaction is given by the bare phonon propagator plus an intermediate electron-phonon interaction, which causes a density fluctuation described by the electron propagator loop, followed by an effective interaction. This diagram describes the infinite sum implied by equations 5.14 & 5.16. Taking the effective interaction to be of this form is equivalent to adopting the RPA approximation.	94

5.5	The electron-phonon scattering mediated conductivity of graphene. In (a) we present both the intraband and interband contributions. It is found that for $T > 100K$ the intraband contributions dominate. The $T = 30K$ results are shown in the inset due to their relatively small magnitude. In (b) we show the interband part which is shown to have several multi-phonon processes, but the magnitude of this contribution is relatively negligible except at very low and very high temperatures.	105
5.6	The temperature dependence of the magnitude of the conductivity at $\omega = \omega_{LO}/2$ (the continuum peak), and $\omega = \omega_{LO}$, (the dominant resonant peak) from figure 5.5. In (a) we show the inter- and intraband contributions together and obtain a roughly linear relationship. When plotted in log-log form (inset), we see that there is a significant ‘kink’ at $T \approx 30K$. When considering only interband transitions as in (b), both peaks display an exponential temperature dependence.	106
5.7	The two dominant response peaks increase in magnitude for doped samples, and are symmetric about zero doping due to electron-hole symmetry. This can be attributed to the increased availability of intraband transitions, which are the dominant mechanism. . . .	107

To my beautiful wife Ally – friend, companion, comrade

Abstract

We investigate the electronic and optical properties of various one and two dimensional graphene based materials. Using the tight binding approximation, we calculate the electronic dispersions of these systems. Using Green's functions, we then evaluate the dielectric function within the random phase approximation (RPA), and the corresponding collective excitation spectrum for armchair graphene nanoribbons. We also calculate the Kubo formula-based optical conductivity of single layer graphene, bilayer graphene, graphene nanoribbons, bilayer graphene nanoribbons, and stretched graphene. For single layer graphene within the Dirac approximation we also calculate the third order nonlinear optical conductance (a nonlinear correction to the 'universal' conductivity, as well as a frequency tripling term) and finally the effect of electron-LO phonon scattering on the 'universal' conductivity at various temperatures and doping levels.

There are several results of particular interest. We predict a roton-like mode in the collective excitation spectrum of non-Dirac armchair graphene nanoribbons. We also demonstrate a two order of magnitude enhancement to the optical conductivity of an entire subclass of bilayer graphene nanoribbons in the terahertz-far infrared regime. A strong nonlinear conductance of single layer graphene under moderate field strengths at room temperature is derived. Finally, stretching induced hall optical conductivity and chirality dependent anisotropy in single layer graphene under conservative stretching conditions are predicted.

We find that the optical properties of graphene based materials are remarkably robust and highly tunable, particularly within the terahertz

to far-infrared regime. Furthermore, the prediction of a roton-like minimum in the collective excitation spectra of a subclass of armchair ribbons makes these particular graphene based materials part of an extremely small subclass of materials, and represents the opening of a potentially huge new field of fundamental research.

List of Publications

Refereed Journal Articles

1. Wright A.R., and Zhang C. “Dynamic conductivity of graphene with electron-LO-phonon interaction” Phys. Rev. B. **81**, 165413 (2010).
2. Wright A.R., Cao J.C., and Zhang C. “Enhanced optical conductivity of bilayer graphene nanoribbons in the terahertz regime” Phys. Rev. Lett. **103**, 207401 (2009).
3. Wright A.R. and Zhang C. “Stretching induced conductance anisotropy and Hall current in graphene” App. Phys. Lett. **95**, 163104 (2009), selected for the November 2, 2009 issue of Virtual Journal of Nanoscale Science & Technology.
4. Wright A. R., Xu X. G., Cao J. C., and Zhang C., “Strong nonlinear optical response of graphene in the terahertz regime”, Applied Physics Letters **95**, 072101 (2009), selected for the August 31, 2009 issue of Virtual Journal of Nanoscale Science & Technology.
5. Wright A. R., Liu F., and Zhang C., “The effect of next nearest neighbour coupling on the optical spectra in bilayer graphene” Nanotechnology **20**, 405203 (2009).
6. Liu J., Wright A. R., Zhang C. and Ma Z., “Strong terahertz conductance of graphene nanoribbons under a magnetic field”, Applied Physics Letters **93** (4), 041106, (2008).

7. Liu J., Ma Z., Wright A. R. and Zhang C., “Orbital magnetization of graphene and graphene nanoribbons”, *Journal of Applied Physics* **103**, 103711 (2008).
8. Li Z., Ma Z., Wright A.R., Zhang C., “Spin-orbit interaction enhanced polaron effect in two-dimensional semiconductors”, *Applied Physics Letters* **90**, 112103 (2007).
9. Yang C.H., Wright A.R., Gao F., Zhang C., Zeng Z., Xu W., “Two colour plasmon excitation in an electron-hole bilayer structure controlled by the spin-orbit interaction”, *Applied Physics Letters* **88**, 223102 (2006).

Submitted Manuscripts

1. Wright A.R. and Zhang C., “Roton Mode in the Collective Excitation Spectrum of Graphene Nanoribbons”, Submitted to *Physical Review Letters*.
2. Wright A.R. T. E. O’Brien, D. Beavan, and Zhang C., “Band-gap scaling and gapless insulator in semi-hydrogenated graphene”, Submitted to *Physical Review Letters*.

Refereed Conference Papers

1. Wright A.R. and Zhang C., “Strong optical absorption of bilayer graphene in THz-FIR regime”, to be published in proceedings of IRMMW’09 - Invited Talk upgraded to Keynote Presentation based on this manuscript.
2. Wright A.R. and Zhang C., “Optical absorption of bilayer graphene nanoribbons”, to be published in proceedings of CLEO-Asia ’09
3. Wright A.R., Wang G.X., Xu W., Zeng Z., and Zhang C., “The spin-orbit interaction enhanced terahertz absorption in graphene around the K point”, *Microelectronics Journal* **40**, 857 (2009).
4. Wright A.R., Liu J., Ma Z., Zeng Z., Xu W., Zhang C., “Thermodynamic properties of graphene nanoribbons under zero and quantizing magnetic fields”, *Microelectronics Journal* **40**, 716 (2009).

5. Li L.L., Xu W., Zeng Z., Wright A.R., Zhang C., Zhang J., Shi Y.L.,
“Mid-infrared absorption by short-period InAs/GaSb type II superlattices”
Microelectronics Journal **40**, 815 (2009).
6. Xu W., Zeng Z., Wright A.R., Zhang C., Zhang J., Lu T.C., “Exchange-
induced band hybridization in InAs/GaSb based type II and broken-gap
quantum well systems”, Microelectronics Journal **40**, 809 (2009).
7. Li L. L., Xu. W., Zeng Z., Wright A. R., Zhang C., Zhang J., Shi Y.
L., Lu T. C., “Terahertz band-gap in InAs/GaSb type-II superlattices”,
Microelectronics Journal **40**, 812 (2009)

Acknowledgements

When sitting alone in the office I sometimes feel very isolated. However, friendship and collaboration have been found through the following people. I am greatly indebted to my supervisor, Prof. Chao Zhang. I defy anyone to show me a better supervisor. Chao has treated me with respect and generosity. He is always available for a chat, and knows everything about everything. I have thoroughly enjoyed working with him on projects since 3rd year, and have only come to respect him more with time.

Thankyou to the rest of the faculty, particularly Dr David Martin for being a dedicated teacher who is always keen for a chat about interesting things and is always very encouraging, Dr George Takacs for being another dedicated teacher, and a good bloke who cares about more than just physics, Mr Duncan Fischer for being another good guy and role model for good teaching, and Prof. Roger Lewis for being ever encouraging and enthusiastic especially when it comes to 'Christian' matters.

Thanks to Mr Daniel Bell for being an extremely good friend throughout my university years, especially for keeping on coming back to the uni even after graduating, and especially for sticking around in Wollongong. Thanks also to Mr Pete Reeve for being a good mate who loves physics, homebrew, and most of all, Jesus.

Thanks to my family for loving and caring for me. Thanks for taking an interest in my ostensibly boring work. Thanks particularly to Mavis for the blanket for my knees.

Thankyou to my beautiful wife Ally who I love. Thankyou for growing up with me. Thanks for trying to be interested in my work. Thanks

for proof-reading everything even though it can't have been interesting. Thankyou for loving me and caring for me, even when I didn't do the same for you. And thankyou to Rose for being a beautiful ray of sunshine in this last year. It has been wonderful watching you grow up and learn to do all sorts of wonderful new things.

And most importantly thankyou to the God and Father of my Lord Jesus Christ, who has blessed me in the heavenly realms with every spiritual blessing, and will save me on the last day from my rottenness because He said he would through the death of his Son. This is more love than I know what to do with. It is for his glory that this work was undertaken.

Introduction

The field of graphene research is *huge* (1; 2; 3). Since the invention of carbon nanotubes in 1991 (4), research into hexagonally arrayed graphitic carbon systems has escalated. Despite being a simpler and more versatile system to consider theoretically, graphene's rise took place more than a decade later in 2003, when the group of Novoselov and Geim reported that they had managed to create and detect single and few layer graphite (5). Since this first seminal work was performed, publications in the field of graphene based structures has exploded.

In 1946, long before its intentional fabrication, P.R. Wallace developed the tight binding bandstructure theory of graphene and demonstrated its unusual properties (6). The motivation for this work was the extension to a superlattice which he would use to describe the properties of bulk graphite. In 2003 however, this work took on new significance, and Wallace's pioneering work turned out to be 60 years ahead of its time. 20 years after this seminal work, Slonczewski, Weiss, and McClure (SWM) developed the interlayer coupling theory for stacked graphene (7; 8). The collective work of these three was remarkably successful at the time, and again has resurfaced in the context of stacked graphene layers. Utilising the theories of Wallace and SWM, single layer graphene, bilayer graphene, graphene nanoribbons, layered graphene nanoribbons, and the curved, rolled, crumpled, rippled, stretched (and any other deformation imaginable) variations on these materials have been successfully and extensively studied over the last few years.

The focus of much of the current research on graphene structures is concerned with so-called 'Dirac fermions' (although the recent review by Geim expounds the ever growing volume of work in other areas (2)). The low energy bandstructure of graphene is conical, which immediately implies a constant density of states

(DOS), a constant group velocity akin to the behaviour of photons or neutrinos, and electron hole symmetry. The latter two have been confirmed experimentally (9). This unusual ‘massless’ low energy bandstructure makes graphene a veritable treasure-trove of never before seen properties, and also a potential low energy, solid state laboratory for experiments in relativistic quantum electrodynamics in $2 + 1$ dimensions. Therefore, since 2003 many interesting properties of graphene have been predicted and observed, such as the half-integer quantum Hall effect (9; 10), finite conductivity at zero charge-carrier concentration (9), the strong suppression of weak localization (11; 12; 13), and the prediction of almost perfect fluidity (14), to name just a few. These properties can be attributed to the linear ‘Dirac’ bandstructure, and low dimensionality, which lead to aforementioned QED-like effects, rather than particulate ones (15; 16).

There is a plethora of interesting phenomena pertaining to the unique properties of graphene based systems. They are outlined in detail in the excellent review articles available on the subject (1; 2; 3).

The ‘universal’ conductance of graphene is a remarkable ac phenomenon (17). It is a direct result of the linear energy dispersion of graphene. As already mentioned, linear subbands imply a constant density of states, but also consistent transition matrix elements, which means that for as long as the Dirac approximation is valid, the conductance is a constant. The value of the universal conductance of single layer graphene is $\sigma_0 = e^2/4\hbar$. This result is easily achieved by several methods. In particular the Kubo formula yields this result for an intrinsic system and neglecting electron-electron (or any other) interactions.

Deviations from ‘universal’ conductance have been shown to occur due to variations in geometry (18; 19), field energy (20; 21), and field intensity (22; 23). It need not be demonstrated that the effect of finite temperature on the distribution functions, as well as doping to create an effective band gap between available states, will also alter the value of σ_0 , especially at lower energies.

In fact, the optical properties of graphene based systems has become quite an active field of research. After the initial flurry of excitement that followed the demonstration of the universal conductivity at energies as high as the optical regime – a direct demonstration of the accuracy of the Dirac bandstructure – there has been increasing interest in graphene based materials for photonic applications,

as well as the realization of graphene's potential in the THz-FIR regime, which have lead to some very interesting results.

With all these predictions and observations having emerged, the optical properties of graphene based systems appear to be more significant and more versatile than perhaps previously believed. With this trend in mind we have proceeded to calculate the optical properties of various graphene based systems under different conditions. The motivation being based on the premise that the 'interesting' optical properties of graphene based systems have not yet been exhausted. As it turns out, our intuition is confirmed, and graphene-based systems produce a rich tapestry of optical properties which are often able to be tuned to one's specific needs, and are often quite unique in the broader field of the optical properties of condensed matter systems.

Our focus has been largely restricted to the THz-FIR regime. The motivation for this choice is the potential use of graphene in photonic device applications in the increasingly important THz band, and the ubiquitous infrared, which is so important for telecommunications purposes. The universal conductivity of graphene has a value of $\sigma_0 = e^2/4\hbar$, which leads to an optical absorption of $\approx 3\%$. Although a remarkably strong value for a single atomic layer system, in absolute terms this is a very weak response, which severely limits the potential applicability of graphene based systems in photonic devices. Therefore we have calculated the optical response for various graphene based systems to determine whether this response can be improved, or whether interesting effects such as anisotropy, nonlinear effects, or non-zero transverse conductivity can be obtained. These results will be presented in due course.

Before delving into the main results of the thesis, we must discuss the geometry of the different graphene systems investigated in this thesis. We will discuss their various electronic properties within the tight binding formalism. This will be the subject of chapter one. After this we will talk briefly about the dielectric properties of one particular graphene system: non-Dirac armchair graphene nanoribbons. This will be the subject of chapter two. The remaining chapters will be devoted to the optical conductance of graphene based systems. We will end with some concluding remarks.

Some Interesting Properties

Unique Dispersions

Firstly however, it may be interesting to summarize some of the more striking properties of graphene-based materials which make them so fascinating to study. The obvious starting point is the electronic dispersions of single and bi-layer graphene. These will be discussed in more detail in the next chapter, and so for now we will consider just the results. The electronic dispersion of graphene near the vertices of the hexagonal Brillouin zone (the K points), is

$$\epsilon_{s,\mathbf{k}} = s v_F |\mathbf{k}|, \quad (1)$$

Where $s = \pm$, and v_F is the Fermi velocity which is $\approx 10^6 \text{ms}^{-1}$. This conical dispersion, which is applicable up to energies of $\approx 1\text{eV}$, makes the fermions in graphene behave as massless particles like photons or neutrinos, and make the Dirac equation, rather than the Schrodinger equation, the natural formalism to use to describe the system. As already mentioned, this opens the gateway to potential “QED-in-a-lab” experiments (1), and also may well revolutionize modern electronics.

Bilayer graphene, near the K points, also has a unique band structure in materials science. The fermions in bilayer graphene can be described as massive Chiral fermions with a symmetrical bandstructure about the neutrality point. The low energy dispersion can be given by

$$\epsilon_{s,\mathbf{k}} = s v_F^2 k^2 / t_{\perp} \quad (2)$$

Where t_{\perp} site-equivalent interlayer coupling (see next chapter). The uniqueness of these two systems can be seen in the figure from the excellent recent review article by A.K. Geim (2) which has been reproduced here in figure 1

The interlayer term in bilayer graphene can be viewed as contributing a mass term to the Dirac equation in making the transition from one to two layers.

With these dispersions in mind, let’s look at a few of the interesting consequences of these unique materials.

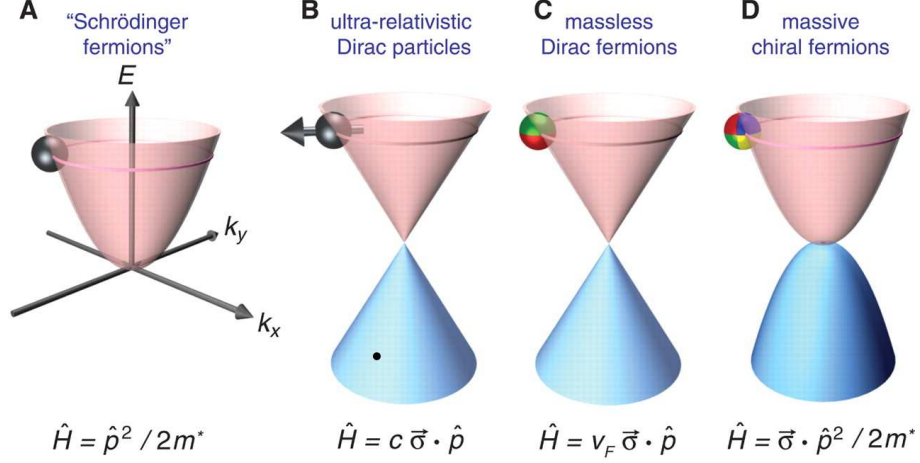


Figure 1: The fermions in graphene are described by the conical massless Dirac dispersion which is a low energy manifestation of an ultra-relativistic equivalent dispersion. The fermions in bilayer graphene have no known equivalent, and can be described as massive chiral fermions with a symmetrical bandstructure.

The Klein Paradox

An elegant example of the unusual chiral properties of graphene is in the derivation of the Klein paradox (16; 24). We first note that the wavefunction for Dirac fermions in graphene can be given by

$$\psi(\mathbf{k}) = \frac{1}{\sqrt{2}} \begin{pmatrix} 1 \\ \pm e^{i\phi(\mathbf{k})} \end{pmatrix} \quad (3)$$

Where $\phi(\mathbf{k}) = \tan^{-1} k_y/k_x$. We now consider scattering by a finite potential well of magnitude V_0 and width D , as shown in figure 2. There are thus three regions as marked in the figure. In region I, we have

$$\psi_I(\mathbf{r}) = \frac{1}{\sqrt{2}} \begin{pmatrix} 1 \\ s e^{i\phi(\mathbf{k})} \end{pmatrix} e^{i(k_x x + k_y y)} + \frac{r}{\sqrt{2}} \begin{pmatrix} 1 \\ s e^{i(\pi - \phi(\mathbf{k}))} \end{pmatrix} e^{i(-k_x x + k_y y)} \quad (4)$$

Which has a right and left moving component, where $s = \pm 1$, and in polar coordinates, and considering fermions with Fermi momentum k_F , we have $k_y = k_F \sin \phi(\mathbf{k})$ and $k_x = k_F \cos \phi(\mathbf{k})$. In region II

$$\psi_{II}(\mathbf{r}) = \frac{a}{\sqrt{2}} \begin{pmatrix} 1 \\ s' e^{i\theta} \end{pmatrix} e^{i(q_x x + k_y y)} + \frac{b}{\sqrt{2}} \begin{pmatrix} 1 \\ s' e^{i(\pi - \theta)} \end{pmatrix} e^{i(-q_x x + k_y y)} \quad (5)$$

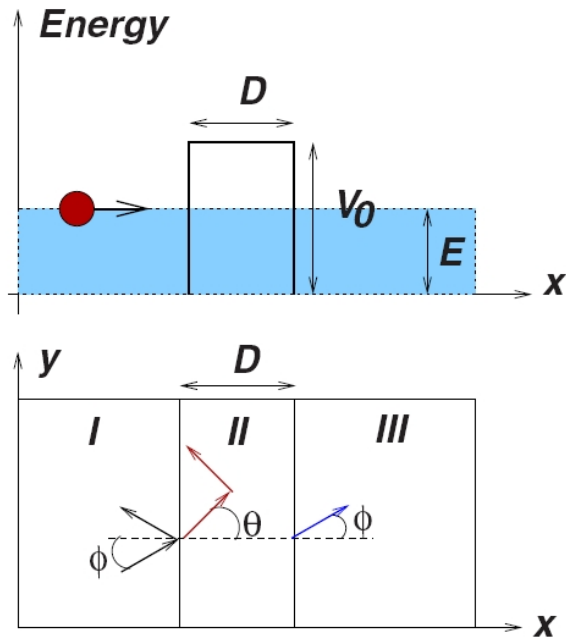


Figure 2: The proposed setup to demonstrate the Klein paradox. An incoming Dirac Fermion hits a finite potential well of magnitude V_0 and width D . The transmission is calculated as usual in elementary quantum mechanics by demanding the continuity of the wavefunctions. Figure from reference (1)

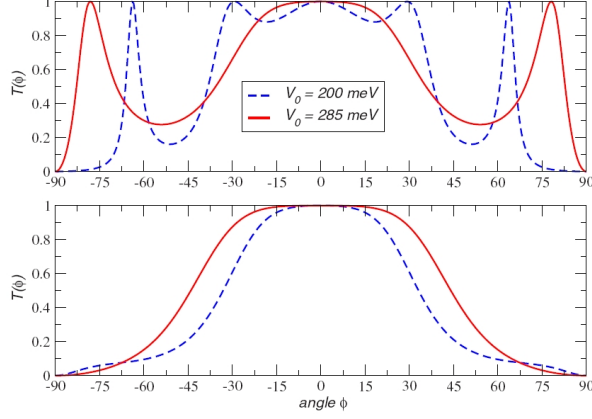


Figure 3: The transmission results from equation 7 for different values of V_0 , where $D = 110\text{nm}$ (top), and $D = 50\text{nm}$ (bottom). Aside from normal incidence there are potentially other points of absolute transmission as well. This absolute transmission is a manifestation of the Klein paradox. Figure from reference (1)

Were $\theta = \tan^{-1}(ky/qx)$, and $q_x = \sqrt{(V_0 - E)^2/(v_F)^2 - k_y^2}$, and for region III we have only a right moving component

$$\psi_{III}(\mathbf{r}) = \frac{t}{\sqrt{2}} \begin{pmatrix} 1 \\ s e^{i\phi(\mathbf{k})} \end{pmatrix} e^{i(k_x x + k_y y)} \quad (6)$$

Where $s = \text{sgn}(E)$ and $s' = \text{sgn}(E - V_0)$. According to the standard prescription, the coefficients of the wavefunctions must be determined such that continuity is preserved at the boundaries $x = 0, D$, but the derivative need not be matched in this case, unlike with the Schrodinger equation. The transmission as a function of incident angle is $T(\phi) = tt^*$, and is given by

$$T(\phi) = \frac{\cos^2 \theta \cos^2 \phi}{(\cos(Dq_x) \cos \phi \cos \theta)^2 + \sin^2(Dq_x)(1 - ss' \sin \phi \sin \theta)^2} \quad (7)$$

What is unusual about this result is that for $Dq_x = n\pi$, the barrier becomes completely transparent ($T(\phi) = 1$), which includes normal incidence ($\phi \rightarrow 0$). This is the Klein paradox, and is unique for relativistic electrons. Some nice results are reported in figure 3, where, depending on the value of V_0 , there are several points with complete transmission. This unusual behaviour is discussed in some detail in reference (1), and most of the discussion up to here has followed this reference closely.

Anomalous Integer Quantum Hall Effect

The components of the resistivity and conductivity tensors are given by

$$\begin{aligned}\rho_{xx} &= \frac{\sigma_{xx}}{\sigma_{xx}^2 + \sigma_{xy}^2} \\ \rho_{xy} &= \frac{\sigma_{xy}}{\sigma_{xx}^2 + \sigma_{xy}^2}\end{aligned}\tag{8}$$

Where σ_{xx} is the longitudinal conductivity and σ_{xy} is the Hall conductivity. When the chemical potential is inside a region of localized states, there is no longitudinal component to the conductivity. However, when the chemical potential crosses a Landau level, it is in a region of de-localized states, and $\sigma_{xx} \neq 0$, and σ_{xy} varies continuously. Imagine an experimental setup of (essentially) a carbon nanotube as proposed by Laughlin (25), and shown in figure 4. A magnetic field passes normally through the surface of the tube, and a current passes circumferentially around the loop. From the Lorentz force, the magnetic field induces a Hall voltage perpendicular to both the field and current. There is thus a magnetic flux travelling down the tube. The current is given by

$$I = c \frac{\partial E}{\partial \phi}\tag{9}$$

Where E is the total energy of the system, and ϕ is the flux. The localized states do not respond to changes in ϕ , only the delocalized ones. Imagine we now changed the flux by a single flux quantum $\Delta\phi = hc/e$. During the change of flux, an integer number of states enter the cylinder at one edge and leave at the opposite edge.

In general, due to the four fold degeneracy of the system (two equivalent K points, and assuming spin degeneracy), when the flux changes by a single quantum, the change in energy is $\pm 4NeV_H$ where V_H is the induced Hall voltage, and the \pm comes from whether they are holes or electrons. However what happens when the chemical potential is at exactly half filling – the Dirac point? According to our reasoning, there would be a Hall plateau at this level with $\sigma_{xy} = 0$. However this cannot be the case because there is a Landau level at this point, and as we stated before this rules out the plateau due to the presence of extended states.

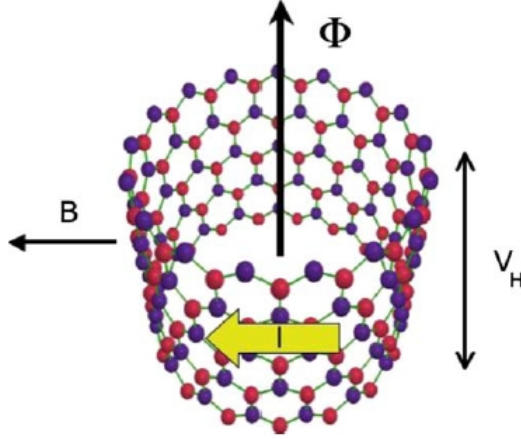


Figure 4: Laughlin’s proposed experiment to probe the quantum Hall effect in graphene. He suggested a carbon nanotube type configuration with a magnetic field passing through the surface of the tube, and a current passing circumferentially around the tube such that there is a flux ϕ down the axis of the tube, and a Hall voltage V_H is induced perpendicular to the field. Figure from reference (1)

This conundrum has been tackled by several authors, and has a rather simple explanation which is very neatly and simply explained by Castro Neto et al in reference (1): “because of the presence of the zero mode that is shared by the two Dirac points, there are exactly $2(2N + 1)$ occupied states that are transferred from one edge to another. Hence, the change in energy is $\delta E = \pm 2(2N + 1)eV_H$ for a change of flux of hc/e . Therefore, the Hall conductivity is

$$\sigma_{xy} = \frac{1}{V_H} = \frac{c\delta E}{V_H\delta\phi} = \pm 2(2N + 1)\frac{e^2}{h} \quad (10)$$

Without any Hall plateua at $N = 0$ ”!

This phenomenal and yet elegantly simple result has been realised experimentally, as shown in figure 5.

Universal Conductivity

The universal conductivity of graphene is an elegant and remarkably simple result, which shows the peculiarity of the Dirac bandstructure. We shall calculate the

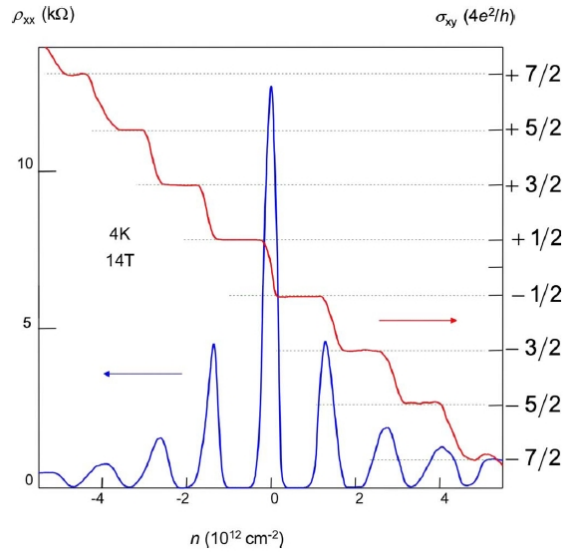


Figure 5: The measurement of the anomalous integer Quantum Hall Effect for graphene. As reasoned by several authors, there is no Hall plateau at $N = 0$. The peak of the blue line at $n = 0$ shows that there is a Landau level when the chemical potential at the neutrality point which draws states equally from the conduction and valence bands. Figure from reference (1)

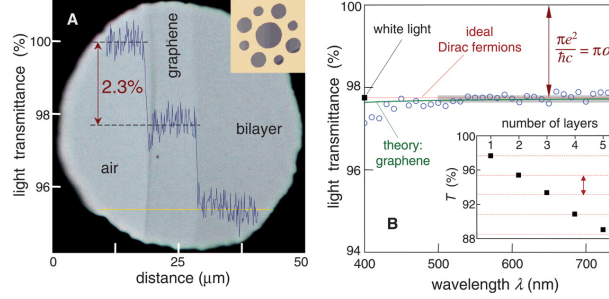


Figure 6: The measurement of the universal conductivity of graphene performed by Nair et al and published in Science magazine ???. Amazingly, the universal conductivity is directly proportional to the fine structure constant, and provides an alternative (albeit less accurate) method for determining it.

universal conductivity of graphene using the time dependent Schrodinger equation in chapter 4, but here shall reproduce the most common derivation which uses linear response theory, namely the Kubo Formula for optical conductivity. This formula will be used extensively in chapters 3 and 5, and so will be properly introduced later. For now however, we need the wavefunctions, corresponding energy levels, and the Kubo Formula. The energy levels have already been presented. The wavefunctions within the Dirac regime are

$$\langle \mathbf{k}, s | = \frac{1}{\sqrt{2}} (1 \quad s(k_x + ik_y)/k) = \frac{1}{\sqrt{2}} (1 \quad se^{i \tan^{-1}(ky/kx)}) \quad (11)$$

And the Kubo formula is

$$\sigma_{\nu, \kappa}(\omega) = \frac{1}{\omega} \int_0^\infty dt e^{i\omega t} \langle [J_\nu(t), J_\kappa(0)] \rangle \quad (12)$$

Where $\hat{v}_\mu = \partial \hat{H} / \partial k_\mu$ is the velocity operator with $\mu = x, y$. Due to the linear dispersion, the velocity operator takes on off diagonal constant values. This leads to the particularly simple result (including only interband transitions)

$$\langle \mathbf{k}, s | \hat{v} | \mathbf{k}, -s \rangle = \frac{k_x}{k^2} \quad (13)$$

We also mention in passing the breakdown of the universal conductivity with increasing energies. As mentioned earlier, the massless Dirac bandstructure quoted for single layer graphene holds up to $|\epsilon| \approx 1\text{eV}$. Moving outside of

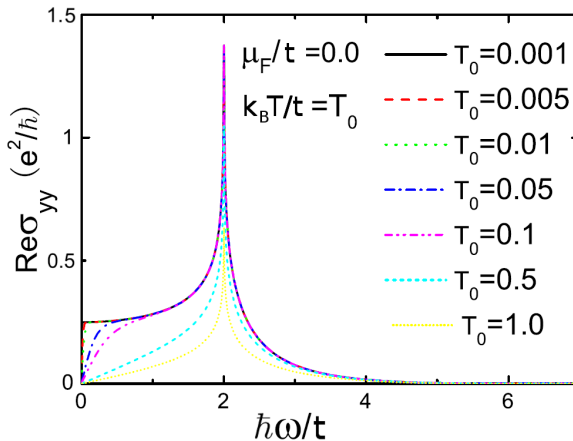


Figure 7: The optical conductivity of graphene outside the Dirac regime contains significant structure which is lost when confined to the linear approximation to the Hamiltonian. The peak corresponds to a van-Hove singularity in the density of states. The full energetic range is $0 < \hbar\omega < 9\text{eV}$. The Dirac formalism is roughly applicable up to $\approx 1\text{eV}$.

this ‘Dirac regime’, one can compute the optical conductivity after expanding the Hamiltonian to second order in momentum (21), or perform no expansions at all and proceed numerically with the full dispersion relation (20). We choose to quote the latter because this work was done within the same group as the other works in this thesis, because it was published first of the two, and finally because it is the most robust tight binding calculation performed to date (at the expense, of course, of obtaining closed form analytic results). In figure 7 we present the optical conductivity of single layer graphene over the full relevant energy range. It can be seen from this figure at what energies the Dirac approximation is appropriate in calculating the universal conductivity. For energies outside this range however, we can see that there is a peak, corresponding to a van-Hove singularity in the density of states of graphene which in turn corresponds to a saddle point in the bandstructure, followed by a gradually diminishing response for higher energies.

The unusual properties mentioned here are just a few examples of the many interesting properties of graphene based materials. The literature on graphene, despite its relatively young age, is enormous, and it is almost impossible for one

to keep abreast of the rapid progress that this field is currently undergoing. This makes graphene an exciting field to be involved in. As experimental techniques develop, one would expect that even more unexpected properties will arise with time.

Current Status and Motivation

A final word before delving into the results of this thesis. Graphene research can be, in my opinion, summarised by two major motivations: “The universe in a Helium droplet”, and “Moore’s Law”.

The former is a broad approach to condensed matter that summarises one of the most interesting aspects of modern condensed matter theory, and indeed, all of physics (and is also the title of a book by Volovik ??). As mentioned above, graphene may serve to investigate certain aspects of relativistic QED. This is not the only area where graphene research may further fundamental physics. There is a lot of interest in graphene as a quantum Hall system. The observation of fractional statistics and non-abelian quasi-particles has so far remained elusive. Quantum Hall systems are the most likely candidate systems where these are expected to be observed. Graphene may play a major role in this in the future. The quantum spin Hall effect was initially proposed for a graphene system (26), though unfortunately the intrinsic spin splitting of graphene may be too small for this proposal to be realised for graphene. Nevertheless, this has opened the door to a new class of topological insulators which are expected to be realised in other systems that can be tuned to have the same Dirac dispersions but with much larger spin-splitting. Graphene provides a solid-state laboratory with relativistic massless particles, and oddly behaved massive chiral Fermions with which we can tinker. Within the exciting field of emergent phenomena and the topological states of matter, graphene promises to provide some interesting predictions for fundamental physics.

The question of fundamental physics arising from emergent phenomena is the motivation behind the results of chapter 2 of this thesis. We calculated the collective excitation spectrum of non-Dirac armchair graphene nanoribbons and found that these materials produced plasmons with a non-propagating roton

minimum as their lowest energy excitation. This unusual result may uncover some interesting outstanding questions concerning rotons, 1D vortices, and bulk-edge coupling: questions of considerable import in the fields of Quantum Hall systems and topological states of matter. Interestingly, the only other material to display such a collective mode in the absence of an external magnetic field is the apparently ‘universe containing’ Helium droplet alluded to earlier!

The latter major motivation for graphene research is much more down to earth and practical: Moore’s Law. Everybody knows what Moore’s Law is, and more importantly, it is becoming increasingly obvious that Moore’s Law is decelerating. Graphene’s amazing electronic and transport properties which include dissipationless transport, the strong suppression of weak localization, and width and chirality dependent band gaps and band-structures, make it a prime candidate for implementation in the next generation of electronic devices, and provide some positive contribution to extending Moore’s Law into the next few years. The outstanding questions in this area are being answered at a very rapid rate. The questions are obvious: What properties of graphene will be most useful for device application? Will disorder destroy these promising effects?

These sorts of questions form the basis for chapters 3-5 of this thesis. Chapters 3 and 4 are concerned with the optical properties of graphene based systems with different geometries. The optical response of graphene is remarkably high for a single atomic layer ($\approx 3\%$ absorption). Furthermore, the characteristic energy scales of the coupling constants often fall within the terahertz–far-infrared regimes, which are of considerable import at present. This makes the investigation of the optical properties in different geometries an obvious path to take, and some interesting results are found. Chapter 5 addresses this question of disorder, by introducing phonons into the problem. For device application, room temperature physics is of paramount importance, and so the first sensible addition to the clean system is electron-phonon interactions.

So we can see that the work contained in this thesis arises from two broad approaches to graphene research. We don’t know what the former approach will yield in the years to come, with the outstanding questions being more speculative than anything. Future progress with regard to the latter however, is quite ob-

vious: the inclusion of many types of disorder, scattering, heat, non-equilibrium approaches, exchange and correlation etc.

In any case, it is now time to explore the electronic properties of graphene more closely, in order to lay the framework for the main results of the thesis contained in chapters 2-5.

Chapter 1

Electronic Properties of Graphene

In this thesis, we will investigate five graphene based systems:

1. Single Layer Graphene
2. Bilayer Graphene
3. Graphene Nanoribbons
4. Bilayer Graphene Nanoribbons
5. Stretched Graphene

For each system, we will discuss the peculiar geometry of each system and calculate their electronic dispersion relations and wavefunctions using the tight binding approximation. This is the subject of the present chapter.

The Hamiltonian for all systems considered is calculated using the tight binding approximation which is written in second quantised notation and momentum (\mathbf{k}) space by

$$H = \sum_{i,j,\mathbf{k}} t_{ij} e^{i\mathbf{k} \cdot \hat{\delta}_{ij}} a_i^\dagger(\mathbf{k}) a_j(\mathbf{k}) \quad (1.1)$$

Where i and j denote the i^{th} and j^{th} atoms in the unit cell, t_{ij} is the overlap integral of the wavefunctions of the i^{th} and j^{th} atoms in the unit cell, and $\hat{\delta}_{ij}$

is the vector between those atoms. This is the most general form of a tight-binding Hamiltonian, where all the physics of the system is captured by the phase factors and overlap integrals. The overlap integrals can be calculated by density functional theory, and can be confirmed experimentally by numerous methods. The exact value of the coupling constants in graphene is by now means a closed topic. Even the most important quantity – the first nearest neighbour overlap integral – is not firmly agreed upon.

Nevertheless, only rough values are required for this thesis. Indeed, all overlap integrals shall be normalised by the first nearest neighbour overlap integral, and so only the approximate ratio of different constants will be required. All values used shall be consistent with the majority of the literature, which shall also be the justification for their use.

Usually only the vastly dominant first nearest neighbours are included in the calculations, unless the second nearest neighbours are particularly relevant. The value of the first nearest neighbour coupling is given by $t \approx 3eV$. The second nearest neighbour overlap integral is given by $t' \approx 0.01eV \approx t/30$. The interlayer coupling constants for layered systems will be introduced below.

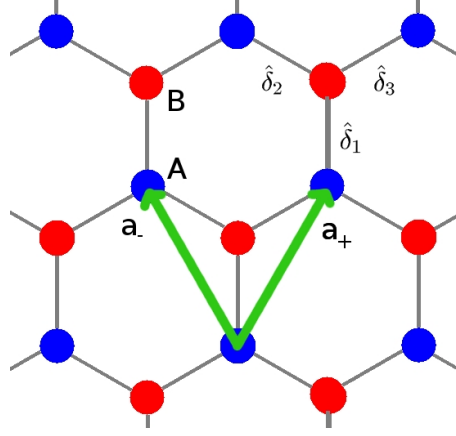


Figure 1.1: Single layer graphene contains two atoms per unit cell, generally denoted by A and B. The first nearest neighbour vectors are shown ($\hat{\delta}_i$), as well as the lattice vectors (\mathbf{a}_{\pm}). The electronic structure is investigated via the tight binding approximation.

1.1 Single Layer Graphene (SLG)

Single layer graphene is the basic building block of all the subsystems encountered in this thesis. Graphene is a two dimensional honeycomb lattice of carbon atoms. A slab of single layer graphene is shown in figure 1.1. As can be seen in the figure, there are two atoms in the unit cell denoted A and B. There are also three nearest neighbour vectors which are

$$\begin{aligned}\hat{\delta}_1 &= (0, b) \\ \hat{\delta}_2 &= \left(\frac{\sqrt{3}b}{2}, -\frac{b}{2} \right) \\ \hat{\delta}_3 &= \left(-\frac{\sqrt{3}b}{2}, -\frac{b}{2} \right)\end{aligned}\tag{1.2}$$

Where $b = 1.42\text{\AA}$ is the first nearest neighbour separation. This will be treated as the intrinsic length scale throughout the thesis, and so all lengths will be normalised by it. And the two lattice vectors are given by $\hat{\delta}_1 - \hat{\delta}_2$ and $\hat{\delta}_1 - \hat{\delta}_3$,

giving

$$\begin{aligned}\mathbf{a}_1 &= \left(-\frac{\sqrt{3}b}{2}, \frac{3b}{2} \right) \\ \mathbf{a}_2 &= \left(\frac{\sqrt{3}b}{2}, \frac{3b}{2} \right).\end{aligned}\tag{1.3}$$

Using Bloch's theorem and the tight binding approximation one can construct the 2D electronic dispersion for single layer graphene.

1.1.1 Full Energy Description

The original formulation of the electronic properties of SLG was calculated by P.R. Wallace in 1947 (6). Whilst he didn't have graphene in mind as a material in its own right, Wallace used the single layer formalism to determine the electronic properties of bulk 3D graphite. For SLG with non-zero nearest neighbour hopping only, the matrix elements are given by

$$\begin{aligned}_A \langle \mathbf{k} | H | \mathbf{k} \rangle_B &= \frac{-t}{N} \sum_{\mathbf{R}, \mathbf{R}', \mathbf{R}''} \left(e^{-i\mathbf{k} \cdot (\mathbf{R}' - \mathbf{R}'')} (\langle \mathbf{R}' | \mathbf{R} \rangle \langle \mathbf{R} + \hat{\delta}_1 | \mathbf{R}'' \rangle \right. \\ &\quad \left. + \langle \mathbf{R}' | \mathbf{R} \rangle \langle \mathbf{R} + \hat{\delta}_1 - \mathbf{a}_1 | \mathbf{R}'' \rangle + \langle \mathbf{R}' | \mathbf{R} \rangle \langle \mathbf{R} + \hat{\delta}_1 - \mathbf{a}_2 | \mathbf{R}'' \rangle) \right) \\ &= \frac{-t}{N} \sum_{\mathbf{R}, \mathbf{R}', \mathbf{R}''} \left(e^{-i\mathbf{k} \cdot (\mathbf{R}' - \mathbf{R}'')} (\delta_{\mathbf{R}', \mathbf{R}} \delta_{\mathbf{R} + \hat{\delta}_1, \mathbf{R}''} + \delta_{\mathbf{R}', \mathbf{R}} \delta_{\mathbf{R} + \hat{\delta}_1 - \mathbf{a}_1, \mathbf{R}''} \right. \\ &\quad \left. + \delta_{\mathbf{R}', \mathbf{R}} \delta_{\mathbf{R} + \hat{\delta}_1 - \mathbf{a}_2, \mathbf{R}''}) \right) \\ &= \frac{-t}{N} \sum_{\mathbf{R}} \left(e^{-i\mathbf{k} \cdot (-\hat{\delta}_1)} + e^{-i\mathbf{k} \cdot (-\hat{\delta}_1 - \mathbf{a}_1)} + e^{-i\mathbf{k} \cdot (-\hat{\delta}_1 - \mathbf{a}_2)} \right) \\ &= -te^{i\mathbf{k} \cdot \hat{\delta}_1} \left(1 + e^{i\mathbf{k} \cdot \mathbf{a}_+} + e^{i\mathbf{k} \cdot \mathbf{a}_-} \right)\end{aligned}\tag{1.4}$$

And

$$_B \langle \mathbf{k} | H | \mathbf{k} \rangle_A = {}_A \langle \mathbf{k} | H | \mathbf{k} \rangle_B^* \tag{1.5}$$

The overlap of the atomic orbitals of neighbouring sites in graphene will be the unit of energy by which all other energy values in this thesis will be normalised. The value of t in graphene is agreed to be $t \approx 3.0\text{eV}$. The next nearest neighbours can easily be incorporated into the formalism in a similar manner, giving a Hamiltonian matrix of

$$H = \begin{pmatrix} t'H_{11}(\mathbf{k}) & tH_{12}^*(\mathbf{k}) \\ tH_{12}(\mathbf{k}) & t'H_{11}(\mathbf{k}) \end{pmatrix} \quad (1.6)$$

Where

$$H_{12}(\mathbf{k}) = -e^{i\mathbf{k}\cdot\hat{\delta}_1} \left(1 + e^{i\mathbf{k}\cdot\mathbf{a}_+} + e^{i\mathbf{k}\cdot\mathbf{a}_-} \right) \quad (1.7)$$

And

$$H_{11}(\mathbf{k}) = \sqrt{3 - |H_{12}(\mathbf{k})|^2} \quad (1.8)$$

With $t' \approx t/30$. The energy eigenvalues for this system are readily solved as

$$E_s(\mathbf{k}) = t'H_{11}(\mathbf{k}) + st|H_{12}(\mathbf{k})| \quad (1.9)$$

Where $s = \pm 1$. We will define the special case where next nearest neighbour coupling is neglected (i.e. $t' = 0$) as

$$\epsilon_s(\mathbf{k}) = st|H_{12}(\mathbf{k})|^2 = st\sqrt{1 + 4\cos(k_x\sqrt{3}b/2)\cos(k_y/2) + 4\cos^2(k_y/2)} \quad (1.10)$$

The wavefunctions are then easily obtained (and are identical for zero and non-zero t'), and are given by

$$\psi(\mathbf{k}) = \frac{1}{\sqrt{2}} \begin{pmatrix} stH_{12}^*(\mathbf{k})/\epsilon_s(\mathbf{k}) \\ 1 \end{pmatrix} \quad (1.11)$$

Which, by de-Moivres theorem, can be expressed as

$$\psi(\mathbf{k}) = \frac{1}{\sqrt{2}} \begin{pmatrix} ste^{i\phi(\mathbf{k})} \\ 1 \end{pmatrix} \quad (1.12)$$

Where $\phi(\mathbf{k}) = \tan^{-1}(\Im H_{12}(\mathbf{k})/\Re H_{12}(\mathbf{k}))$.

1.1.2 Low Energy Approximation

The energy dispersion curve is given by

$$\epsilon_s(\mathbf{k}) = st|H_{12}(\mathbf{k})|^2 = st\sqrt{1 + 4\cos(k_x\sqrt{3}b/2)\cos(k_y/2) + 4\cos^2(k_y/2)} \quad (1.13)$$

Whose zeroes can be solved by

$$\epsilon_s(\mathbf{k})^2 = t^2(1 + 4\cos(k_x\sqrt{3}b/2)\cos(k_y/2) + 4\cos^2(k_y/2)) = 0 \quad (1.14)$$

There are two inequivalent points that give zero energy, which are usually called the K-points or charge neutrality points. They are $\mathbf{K}, \mathbf{K}' = (\pm \frac{4\pi}{3\sqrt{3}}, 0)$. Expanding around one of these points, we obtain a greatly simplified Hamiltonian matrix. To do this, we will proceed as follows: near the K-point, the momentum is given by $\mathbf{k} = (K_x + \Delta_x, \Delta_y)$ (since $K_y = 0$). The Hamiltonian near the K-points then, is given by (in terms of the nearest neighbour vectors $\hat{\delta}_i$):

$$\begin{aligned} -H_{12}(\mathbf{k}) &= e^{-i\Delta_y} + 2\cos\left(\frac{\sqrt{3}}{2}(K_x + \Delta_x)\right)e^{i\Delta_y/2} \\ &\approx 1 - i\Delta_y + 2\cos\left(\frac{2\pi}{3} + \frac{\sqrt{3}}{2}\Delta_x\right)\left(1 + i\frac{\Delta_y}{2}\right) \\ &= 1 - i\Delta_y + 2\left(1 + i\frac{\Delta_y}{2}\right)\left(-\frac{1}{2}\cos\left(\frac{\sqrt{3}}{2}\Delta_x\right) - \frac{\sqrt{3}}{2}\sin\left(\frac{\sqrt{3}}{2}\Delta_x\right)\right) \\ &= 1 - i\Delta_y + \left(1 + i\frac{\Delta_y}{2}\right)\left(-1 - \frac{3}{2}\Delta_x\right) \\ &= 1 - i\Delta_y - 1 - \frac{3}{2}\Delta_x - i\frac{1}{2}\Delta_y \\ &= \frac{3}{2}(\Delta_x - i\Delta_y) \end{aligned} \quad (1.15)$$

If we define the group velocity to be $v_F = \frac{3t}{2}$, then we have

$$H_K = v_F \begin{pmatrix} 0 & k_x - ik_y \\ k_x + ik_y & 0 \end{pmatrix} \quad (1.16)$$

For \mathbf{k} sufficiently small and near the K-points. This, in turn, leads to a very simple conical energy dispersion

$$\epsilon_K(\mathbf{k}) = v_F |\mathbf{k}| \quad (1.17)$$

The velocity v_F is $v_F \approx 10^6 m s^{-1}$. The wavefunctions are still given by the full energy form described in equation 1.12, but with

$$\phi(\mathbf{k}) = \tan^{-1}(k_y/k_x). \quad (1.18)$$

The two K points are equivalent unless there is coupling between them in which case a phase factor must be introduced. However this will not be relevant for any of our subsequent work.

1.2 Bilayer Graphene (BLG)

Bilayer graphene is constructed by stacking two single layers on top of one another such that half the B atoms are directly above an A atom as shown in figure 1.2. This so-called ‘Bernal’ type stacking is the most common configuration for multilayer graphene. There are three main types of interlayer coupling in BLG. The direct vertical A-B coupling, given by $\gamma_1 \approx t/10 \approx 0.3eV$. Because the coupling in this case is vertical, there is no induced phase factor in the $k_x - k_y$ wavefunction. This term causes the two single layer subbands to split into two each, giving two valence bands and two conduction bands. The second dominant coupling term, $\gamma_2 \approx 0.12eV$, couples $A - B$ sites between layers which are not directly above and below each other, leading to a phase factor which is associated with this term. This term is often called the ‘trigonal’ term. It causes the single valley K-points of SLG to split into three very small valley K-points, thus causing a ‘trigonal warping’ of the band structure. The third term, $\gamma_3 \approx 0.1eV$, couples $A - A$ and $B - B$ sites between layers, and also induces a phase factor since the sites are offset in the $x - y$ plane. This term causes a breaking of the $x - y$ isotropy of the system, as will be seen in the dispersion curves below.

The Hamiltonian then, including next nearest neighbours (NNN), and the three interlayer coupling terms, is given by

$$H_{\text{BLG}} = \begin{pmatrix} t'H_{11} & tH_{12}^* & \gamma_3 H_{12} & \gamma_1 \\ tH_{12} & t'H_{11} & \gamma_2 H_{12}^* & \gamma_3 H_{12} \\ \gamma_3 H_{12}^* & \gamma_2 H_{12} & t'H_{11} & tH_{12}^* \\ \gamma_1 & \gamma_3 H_{12}^* & tH_{12} & t'H_{11} \end{pmatrix}, \quad (1.19)$$

The eigenvalues and eigenvectors in the absence of γ_3 are readily solved. With γ_3 included however, the form of the solution is unwieldy. The eigenvalues in the simpler case are given by the (relatively) concise form

$$\epsilon_{\lambda,\kappa} = t'(\epsilon_{\text{SL}}^2 - 3) + \lambda \sqrt{\epsilon_{\text{SL}}^2 + \frac{\gamma_{12}^+}{2}} + \mu \sqrt{\Gamma} \quad (1.20)$$

Where

$$\Gamma = \epsilon_{\text{SL}}^2 \gamma_{12}^+ + \frac{(\gamma_{12}^-)^2}{4} + 2\gamma_1 \gamma_2 \epsilon_{\text{SL}}^2 \text{Re}(H_{12}) \quad (1.21)$$

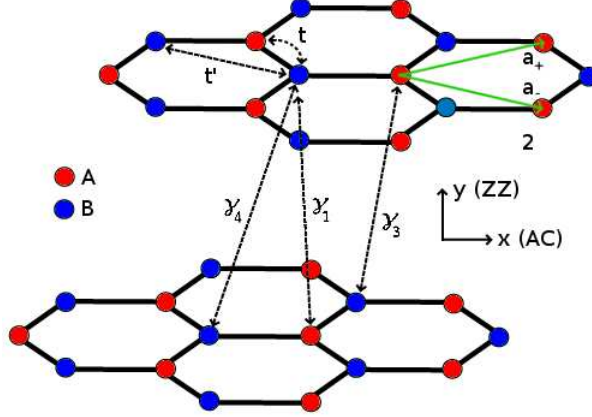


Figure 1.2: The three interlayer terms included in the BLG Hamiltonian, as well as the next nearest neighbour coupling term. γ_2 and γ_3 differ in that they connect, respectively, different and equivalent points in the SLG Brillouin Zone. Whilst γ_1 and γ_2 both represent coupling between different sites in the Brillouin zone, γ_1 is a directly vertical transition, and so the overlap of the wavefunctions is much larger ($\approx 3\times$ larger)

And $\gamma_{12}^\pm = \gamma_2^2 \epsilon_{SL}^2 \pm \gamma_1^2$, where $\lambda, \mu = \pm 1$, ϵ_{SL} are the regular eigenvalues for the SLG system, and all coupling terms have been normalised by t . From this result we see that there are two conduction bands and two valence bands which are confined above and below the line $\epsilon_{\lambda, \mu} - t'(\epsilon_{SL}^2 - 3)$. respectively.

The low energy part of the electronic dispersion curves are seen in figures 1.3 and 1.4. The NNN coupling has plunged the extrema below the Fermi energy. The effect of the dominant interlayer term γ_1 has caused a new pair of bands to emerge which, in this part of the spectrum, are separated from their pairs by an amount γ_1 . The effect of γ_2 and γ_3 is much more subtle. The trigonal warping can be seen by the K-point pair in figure 1.4, and the γ_3 induced loss of isotropy between the two valleys can also be seen. Notice however, that the energy range of these effects is $\approx \gamma_2/1000$, which is extremely small.

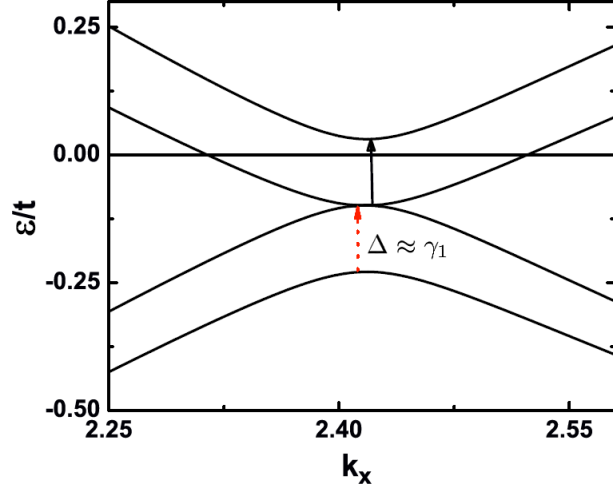


Figure 1.3: The k_x dependence of the bandstructure near the K/K' points with all coupling terms included. The two arrows show the approximately constant (at low energies) gap between similar bands.

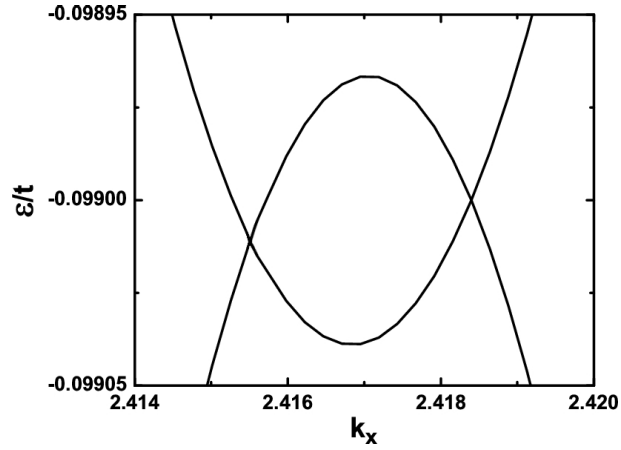


Figure 1.4: The k_x dependence of the two inner bands near the K/K' points zoomed right in to see the effects of γ_2 and γ_3 . The NNN interaction has shifted these features well below the Fermi level. γ_2 causes the second dirac point to emerge, and γ_3 causes one of the two Dirac points to occur at a lower energy.

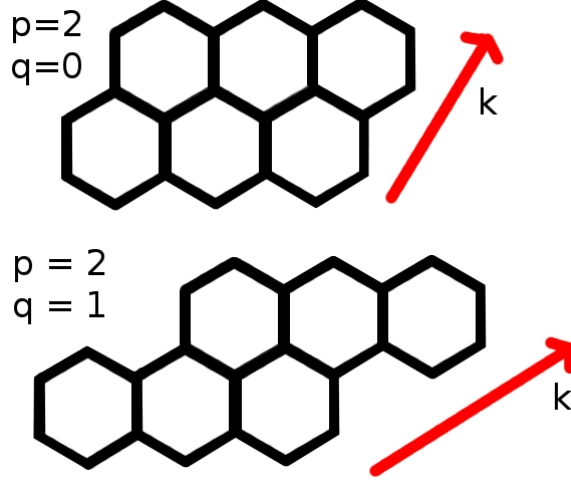


Figure 1.5: The two most typical GNRs are $q = 0$, corresponding to zig-zag ribbons, and $q = 1$, corresponding to armchair ribbons. The elegance of Ezawa's construction is the simplicity of constructing infinite ribbons by placing consecutive stacks of hexagon layers on top of each other, offset by q hexagons. The zig-zag and armchair edges can be readily seen. These are what determine the unique electronic properties of each class of ribbon. The index p essentially determines the width, and does not alter the electronic properties *as much* as q .

1.3 Graphene Nanoribbons (GNRs)

By cutting strips of single layer graphene, one can construct one dimensional graphene nanoribbons (GNRs). The electronic properties of GNRs are both width dependent and chirality dependent.

The construction of a GNR that we will use follows that introduced by Ezawa (27), and can be seen in figure 1.5. A GNR can be described by two indices $\langle p, q \rangle$, where q determines the chirality, and $p + q$ is the number of hexagons placed side-by-side in the construction (see the figure). When constructed in this way, $q = 0$ defines a Zig-Zag (ZZ) edged GNR, and $q = 1$ defines an Armchair (AC) edged GNR. The chiral angle (θ_q) is defined as the angle between a zig-zag edge, and the axis direction of the ribbon. From this definition, $\theta_{ZZ} = 0$, and $\theta_{AC} = \pi/6$, and in general $\theta_q = \tan^{-1} \sqrt{3}/(2q + 1)$.

The Hamiltonian for a GNR is given by

$$H_{GNR} = \begin{pmatrix} 0 & H_{AB} \\ H_{BA} & 0 \end{pmatrix} \quad (1.22)$$

Where the elements of H_{AB} are of the form $te^{ikb\cos(\theta_q+\phi_i)}$, and $H_{BA} = H_{AB}^*$. Here ϕ_i is the chiral angle of the unit vector that joins A and B such that

$$\begin{aligned} \phi_1 &= \pi/6 \\ \phi_2 &= 5\pi/6 \\ \phi_3 &= 3\pi/2. \end{aligned} \quad (1.23)$$

As an example, the hamiltonian matrix for a $\langle 2, 1 \rangle$ AC-GNR is

$$H_{\langle 2,1 \rangle} = \begin{pmatrix} 0 & H_{AB}^{(2,1)} \\ H_{BA}^{(2,1)} & 0 \end{pmatrix} \quad (1.24)$$

Where

$$H_{AB}^{(2,1)} = \begin{pmatrix} e^{ikb\sqrt{3}/2} & e^{ikb} & 0 & 0 & 0 \\ e^{-ikb\sqrt{3}/2} & e^{ikb\sqrt{3}/2} & e^{ikb} & 0 & 0 \\ 0 & e^{-ikb\sqrt{3}/2} & e^{ikb\sqrt{3}/2} & 0 & e^{ikb} \\ 0 & 0 & e^{-ikb\sqrt{3}/2} & e^{ikb} & e^{ikb\sqrt{3}/2} \\ 0 & 0 & 0 & e^{ikb\sqrt{3}/2} & e^{-ikb\sqrt{3}/2} \end{pmatrix} \quad (1.25)$$

And $H_{BA}^{(2,1)} = H_{AB}^{(2,1)*}$. The electronic dispersion curves for this GNR are shown in figure 1.6(b). Note that the linear Dirac-like bandstructure has re-emerged for this ribbon. One third of AC-GNRs have Dirac subbands, with the condition being $p + 1 \in 3N$ where N denotes the integers.

A typical ZZ-GNR bandstructure is shown in figure 1.6(a). The low energy bandstructure is no longer linear in this case, and all zig-zag ribbons have a zero energy gap at the Fermi energy. This zero gap condition is met over an extended region, which implies a very high density of states at the Fermi level. By selecting the appropriate width and chirality, a ribbon can be chosen with the desired electronic properties. One last example is shown in figure 1.6(c), which is the bandstructure of the $\langle 3, 3 \rangle$ chiral ribbon. Note that this too has a low energy

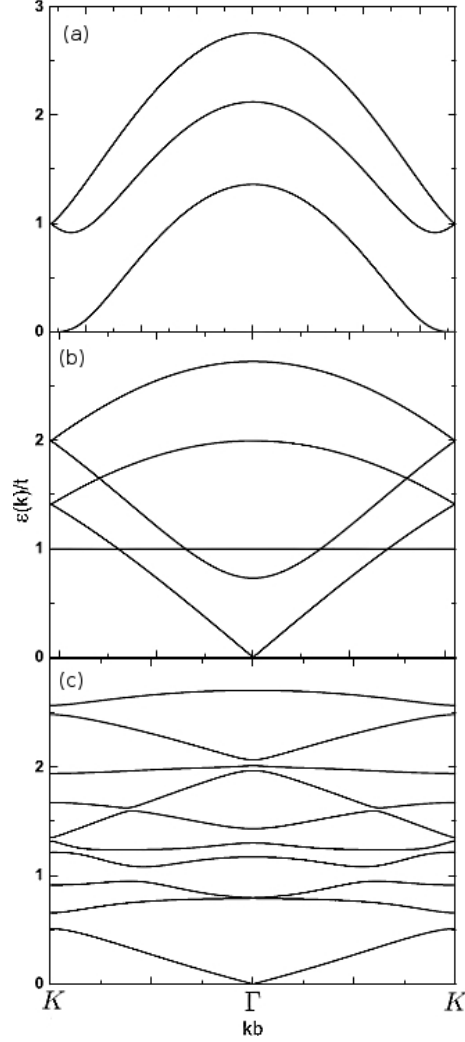


Figure 1.6: (a) A typical zig-zag nanoribbon bandstructure ($p = 2$). Note that at the brillouin zone edges the energy gap becomes zero. This is the case for all ZZ-GNRs. The linear Dirac dispersion is, however, not present, in these structures. (b) A typical armchair nanoribbon bandstructure ($p = 2$). The low energy linear Dirac dispersion occurs in armchair ribbons where $p + 1 \subset N$. For all other AC-GNRs, there is a small band gap. (c) A $\langle 3, 3 \rangle$ chiral GNR. A small number of GNRs with $q > 1$ have a linear Dirac-like dispersion with no energy gap, but in general this will not be the case, and the bandgaps and curvature of the bands will vary dramatically from ribbon to ribbon.

Dirac subband structure. This is not the norm, and there are only a handful of cases where this is true for $q > 1$.

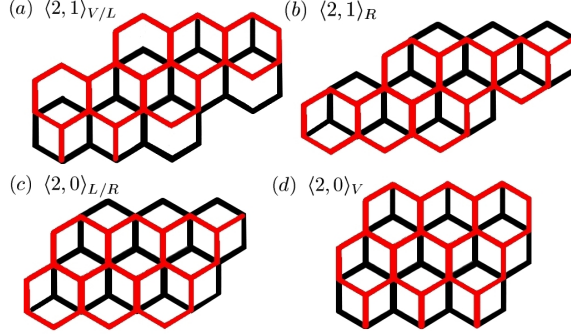


Figure 1.7: A selection of armchair and zig-zag lgnrs with the two distinct possible stacking orientations. These cause different edge sites to couple between layers in slightly different ways, leading to subtle changes in the electronic bandstructure.

1.4 Bilayer Graphene Nanoribbons (BLGNRs)

When constructing bilayer graphene using the normal ‘bernal’ type stacking, the second layer is shifted along one of the three C-C lattice vectors relative to the first. The choice as to which lattice vector the shift is to be made along, in 2D bilayer graphene, is arbitrary, since a simple rotation of the entire system by an amount $2\pi/3$ or $4\pi/3$ will obtain the alternative orientations.

When constructing bilayer graphene nanoribbons however, the choice of lattice vector along which to shift the second layer alters the electronic properties of the ribbon in various ways. Due to the C_3 symmetry of single layer graphene’s hexagonal lattice, there are three equivalent ways to cut out any particular chirality ribbon. For example, cutting parallel to any of the three lattice vectors will produce an armchair ribbon, and cutting perpendicular to any lattice vector will produce a zig-zag ribbon.

With the second layer of bilayer graphene being shifted along one of the three lattice vectors however, this creates, in general, three inequivalent ribbon cuts. The C_3 symmetry in this case, has been lost.

In the case of ZZ- and AC-BLGNRs however, due to their particular symmetry, there are only two inequivalent ribbons. Consider a second layer shift along $\hat{\delta}_1$ for example as in figure 1.7. When constructing an armchair bilayer ribbon out of this system, if the cut is parallel to $\hat{\delta}_2$, then flipping the system over (or

viewing it from behind) will transform the ribbon to one cut parallel to $\hat{\delta}_3$. This is due to the equivalence of the two layers, meaning which one is the top layer and which one is the lower layer, in this case, is arbitrary. Similarly, consider a zig-zag ribbon cut out of the same system. If the cut is made perpendicular to $\hat{\delta}_2$, and then the system is flipped (or viewed from behind), it will appear to have been cut perpendicular to $\hat{\delta}_3$.

The high symmetry of these particular cases aside however, there are, in general, three inequivalent ribbons, of equal chirality, which can be cut out of bilayer graphene.

Including only the directly vertical interlayer coupling terms, one can determine the tight binding matrix elements from the Hamiltonian

$$H = \sum_{i,j,l} t_{ij} c_{i,l}^\dagger c_{j,l} + \sum_{i,j} \gamma_{ij} c_{i,l_1}^\dagger c_{j,l_2} \quad (1.26)$$

Where i and j denote the lattice sites on layer l_1 or l_2 , $t_{i,j} = t = 3.0eV$ is the regular intralayer nearest neighbour overlap matrix if i and j are nearest neighbours, and zero otherwise, and $\gamma_{ij} = \gamma = 0.13eV$ is the regular dominant interlayer term for bilayer graphene if i on l_1 is directly above j on l_2 , and zero otherwise.

Returning to the case of the $\langle 2, 1 \rangle$ ribbon, the Hamiltonian matrix is

$$H_{(2,1)}^{BLG NR} = \begin{pmatrix} H_{(2,1)}^{GNR} & H_{inter}^S \\ H_{inter}^S & H_{(2,1)}^{GNR} \end{pmatrix} \quad (1.27)$$

Where S denotes the shift type : (V)ertical, (R)ight, or (L)eft. The vertical and left shift interlayer coupling matrices are equivalent in the armchair case, and are given by

$$H_{inter}^{V/L} = \begin{pmatrix} 0 & h_{V/L} \\ h_{V/L}^T & 0 \end{pmatrix} \quad (1.28)$$

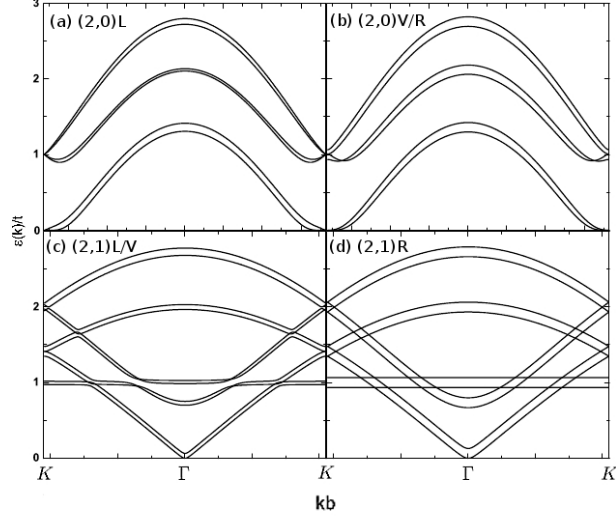


Figure 1.8: The bandstructures for the high symmetry bilayer ribbons ($q = 0, 1$), with $p = 2$. In general, when going from a single to a bilayer ribbon, each single layer subband becomes a subband pair which are separated from each other by some amount determined by the interlayer edge state coupling. Note in particular the key differences depending on stacking orientation are at the K and Γ points.

Where

$$h_R = \begin{pmatrix} \gamma & 0 & 0 & 0 & 0 \\ 0 & \gamma & 0 & 0 & 0 \\ 0 & 0 & \gamma & 0 & 0 \\ 0 & 0 & 0 & 0 & \gamma \\ 0 & 0 & 0 & \gamma & 0 \end{pmatrix} \quad (1.29)$$

Is the right shift interlayer coupling matrix, and the vertical/left shift interlayer coupling matrix is given by

$$h_{V/L} = \begin{pmatrix} 0 & \gamma & 0 & 0 & 0 \\ 0 & 0 & \gamma & 0 & 0 \\ 0 & 0 & 0 & \gamma & 0 \\ 0 & 0 & 0 & 0 & 0 \\ 0 & 0 & 0 & 0 & \gamma \end{pmatrix} \quad (1.30)$$

The two inequivalent shifts of the second graphene layer in armchair nanoribbons are parallel to the axis direction, and at an angle of $\pi/3$ to the axis direction. The former leads to complete coupling of potentially vertical sites. This unique

situation in armchair ribbons causes the bandstructure to two simple sets of curves with the simple form

$$\epsilon_i^{\text{BLG NR}} = \pm i\gamma + \epsilon^{\text{SLG NR}} \quad (1.31)$$

Where $i = [0, 1]$. This means that the bilayer armchair GNR with a parallel shift of the second layer has a set of curves equal to the single layer armchair ribbon, and a set of curves equal to the single layer ribbon but γ larger in magnitude.

The second type of bilayer armchair ribbon has some uncoupled sites in the unit cell which effects the bandgaps, making them, in general $< \gamma$, and not constant. Of particular interest are the low energy parts which are no longer two linear bands but instead curved as in 2D bilayer graphene, and at the usually degenerate points at $|\epsilon| = t$, the points are no longer degenerate but a finite gap has emerged.

ZZ-BLG NRs are constructed the same way, except that the right and left shifts are equivalent in this case. The two inequivalent shifts of the second graphene layer in zig-zag nanoribbons are perpendicular to the axis direction, and at an angle of $\pi/6$ to the axis direction. The former leads to an entire overhanging edge on each layer which is not coupled to the other. This in turn leads to a larger deviation from the single layer electronic dispersion. The latter causes less sites to be uncoupled between layers, and so a less drastic shift form for the regular zig-zag ribbon dispersion.

These single to bilayer and stacking dependent properties of the electronic dispersions of armchair and zig-zag bilayer nanoribbons can be seen in figure 1.8. When extending the system to three or more layers, the electronic properties evolve in the same way, and there are many distinct stacking orientations, as the different permutations are not, in general, equivalent.

However, we will not be particularly interested in these various stacking orientations in general. The results obtained for the vertical shift contains all the significant physics for this thesis, and from now on, it will be assumed that all BLG NRs are vertically shifted ones.

1.5 Stretched Single Layer Graphene

Stretched single layer graphene is exactly what it sounds like! We assume that in stretching graphene, the bond lengths remain constant, but the bond angles bend. This is equivalent to assuming that the electronic configuration will maintain a constant energy with respect to the first nearest neighbours, and ignores all other effects (ie the change in configuration with respect to second nearest neighbours). For small angles this is a reasonable approximation. Therefore, we construct stretched graphene as follows:

Assume the centre point of the three lattice vectors is fixed. If we apply a (pseudo) force F in some direction ϕ s.t. $0 < \phi < \pi/2$, then the three bonds will rotate about the fixed point accordingly. We define the three unit vectors as

$$\begin{aligned}\hat{\delta}_1 &= (\sin \theta_1, -\cos \theta_1) \\ \hat{\delta}_2 &= (-\cos(\pi/6 - \theta_2), \sin(\pi/6 - \theta_2)) \\ \hat{\delta}_3 &= (\cos(\pi/6 + \theta_3), \sin(\pi/6 + \theta_3))\end{aligned}\tag{1.32}$$

The latter two can be expanded to give

$$\hat{\delta}_{2,3} = (\mp\sqrt{3}/2 \cos \theta_{2,3} - 1/2 \sin \theta_{2,3}, 1/2 \cos \theta_{2,3} \mp \sqrt{3}/2 \sin \theta_{2,3})\tag{1.33}$$

For most of the working these will be denoted by $\delta_i = (A_i, B_i)$. The three rotation angles θ_i are related by the magnitude of the pseudo-force F , and its direction ϕ . Since the centre point is fixed, the pseudo force will apply a torque to the bonds such that $\tau_i = \hat{\delta}_i \times \mathbf{F}$. But because we are stretching the material, the force is applied in both directions, and so the torque will only be applied to the projection of the unit vector onto the force vector $\hat{n}_i = \mathbf{F}/|\mathbf{F}| \cdot \hat{\delta}_i$. The latter provides the fraction of the torque that is applicable. The final result will give the angles θ_i in parametric form with ϕ and F being the variables. The force then, is given by $\mathbf{F} = F(\cos \phi, \sin \phi)$. So:

$$\hat{n}_i = A_i \cos \phi + B_i \sin \phi\tag{1.34}$$

And

$$\tau_i = F(A_i \sin \phi - B_i \cos \phi) \quad (1.35)$$

And so we have

$$\begin{aligned} \theta_i &= F(A_i \cos \phi + B_i \sin \phi)(A_i \sin \phi - B_i \cos \phi) \\ &= F\left(\frac{A_i^2 - B_i^2}{2} \sin 2\phi - A_i B_i \cos 2\phi\right) \end{aligned} \quad (1.36)$$

Of course these are for the unstretched unit vectors ($\theta_i = 0$), which are

$$\begin{aligned} \hat{\delta}_1^0 &= (0, -1) \\ \hat{\delta}_2^0 &= (-\sqrt{3}/2, 1/2) \\ \hat{\delta}_3^0 &= (\sqrt{3}/2, 1/2) \end{aligned} \quad (1.37)$$

Which give (letting $F/2 \rightarrow F$):

$$\begin{aligned} \theta_1 &= F \sin 2\phi \\ \theta_2 &= F/2(\sin 2\phi + \sqrt{3} \cos 2\phi) \\ \theta_3 &= F/2(\sin 2\phi - \sqrt{3} \cos 2\phi) \end{aligned} \quad (1.38)$$

When stretching along the zig-zag or armchair direction we get the same amount of rotation on different bonds, $\phi = 0$ is the ZZ direction, and we have $\theta_2 = F/2(\sqrt{3})$, and so $F = 1$ corresponds to a rotation of $\sqrt{3}/2$ radians (in this high symmetry case). The resultant construction is shown in figure 1.9

The Hamiltonian matrix element then, is

$$h_{AB} = -t \sum_i e^{i(k_x A_i + k_y B_i)} \quad (1.39)$$

Where $A_1 = \sin \theta_1$, $B_1 = -\cos \theta_1$, and $A_{2,3} = \mp\sqrt{3}/2 \cos \theta_{2,3} - \sin \theta_{2,3}/2$, $B_{2,3} = \mp\sqrt{3} \sin \theta_{2,3}/2 + \cos \theta_{2,3}/2$. Now F is necessarily small, and so we can expand

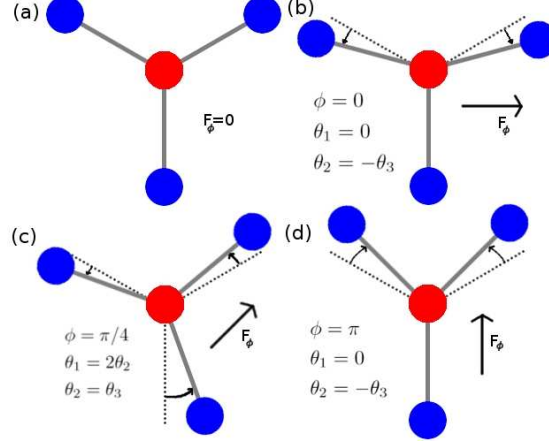


Figure 1.9: The effect of stretching on the three nearest neighbour bond directions when F is applied along various high symmetry directions. The dotted lines in b,c and d are the regular unstretched orientations. The magnitude of F has been chosen to be very large ($F \approx 15$) to emphasise the effect of stretching, however our numerical results will only go as high as $F = 2.5$.

about this first:

$$\begin{aligned}
 A_1 &\approx \theta_1 \\
 B_1 &\approx -1 \\
 A_{2,3} &\approx \mp \sqrt{3}/2 - \theta_{2,3}/2 \\
 B_{2,3} &\approx \mp \sqrt{3}\theta_{2,3}/2 + 1/2
 \end{aligned} \tag{1.40}$$

Therefore, for small F we have

$$\begin{aligned}
 H_{AB} = -t &\left[e^{-ik_y} (1 + iFk_x \sin 2\phi) + 2e^{ik_y/2} (\cos(\sqrt{3}k_x/2) \right. \\
 &\quad - iF/4 \cos(\sqrt{3}k_x/2) (k_x \sin 2\phi + 3k_y \cos 2\phi) \\
 &\quad \left. - F/4 \sin(\sqrt{3}k_x/2) (\sqrt{3}k_y \sin 2\phi + k_x \cos 2\phi) \right)
 \end{aligned} \tag{1.41}$$

This leads to a full energy, small angle dispersion of

$$\begin{aligned} \epsilon_s = st & \left[1 + 4 \left(\cos^2(\sqrt{3}k_x/2) + \cos 3k_y/2 \cos \sqrt{3}k_x/2 \right) \right. \\ & + F \left(\sin \sqrt{3}k_x(2 \cos \sqrt{3}k_x/2 - \cos 3k_y/2)(\sqrt{3}k_y \sin 2\phi + k_x \cos 2\phi) \right. \\ & \left. \left. + \cos \sqrt{3}k_x/2((k_x \sin 2\phi + 3k_y \cos 2\phi) - 4k_x \sin 3k_y/2 \sin 2\phi) \right) \right]^{\frac{1}{2}} \end{aligned} \quad (1.42)$$

Which reduces to the usual result if $F = 0$. As usual for an off-diagonal 2×2 Hamiltonian, the eigenvectors are given by

$$\psi_s(\mathbf{k}) = \frac{1}{\sqrt{2}} \begin{pmatrix} sh_{AB}/|\epsilon| \\ 1 \end{pmatrix} \quad (1.43)$$

The effect of stretching is two-fold. Firstly, stretching breaks the x-y isotropy, leading to a chiral dependence for the low energy velocity, as well as a chiral dependence of the ‘universal’ conductivity. Secondly, stretching breaks the C3 symmetry of graphene, which in turn leads to a non-zero Hall optical conductivity. These will all be discussed further in chapter 3.

1.6 Conclusion

We can see from these results that the electronic properties of graphene based materials vary significantly depending on dimensionality, layering, chirality, and stretching.

We see that single layer graphene is a zero gap semiconductor. It stands in stark contrast to normal metals which exhibit diffusive electron transport and temperature dependent resistivity. The prediction and observation of a minimum dc conductivity and a universal ac conductivity stand as testament to these unique properties. In fact, graphene seems to be increasingly referred to as a superfluid rather than any kind of ‘normal’ electronic system. This seems sensible, as localization is suppressed, and so graphene is not highly correlated. It behaves more like a dilute gas in this respect. The Klein effect makes the transport of Dirac Fermions extremely robust to disorder, aiding the dissipationless transport expected of superfluids. Band structure effects play the key role in all of these phenomena. Graphene is truly a unique material with such varied properties that categorisation into any conventional nomenclature is fruitless.

The derivation of the low energy Dirac Hamiltonian for single layer graphene has been nothing short of a phenomenon in condensed matter physics in the last few years. The Fermi energy in intrinsic graphene happens to lie precisely on the bands-touching points. This is a very interesting feature of graphene as it means that at the Fermi energy there is a vanishing density of states, and no bandgap. It is worth mentioning that the low energy bilayer Hamiltonian, whose form has not been considered as it is not relevant to this thesis, can essentially be described by the Dirac Hamiltonian with a mass term (3).

The chirality of graphene nanoribbons in particular promises some very exciting potential building blocks for electronic device implementation due to their chirality dependent band gaps. In particular, one can imagine that two ribbons, one armchair with zero-bandgap, and one chiral with a small finite band gap, can be joined together by ‘simply’ cutting along one direction, then cutting along the other. And so semiconductor-metal junctions can possibly be formed by simply cutting graphene along different directions. The holy grail in this context would be electronic device production on the smallest scale ever achieved, by simply

‘stamping’ out patterned graphene into networks of various chirality graphene nanoribbons.

The main characteristic energies of layered graphene materials in particular lie within the terahertz to far infrared regime. The second nearest neighbour intralayer coupling, as well as all three major interlayer couplings are all within this region of the spectrum. Because of this, it is not unreasonable to expect that graphene will be quite active within this region. This is part of the motivation, and cause for much of the success, for the results in chapter 3.

Before delving into the optical properties of these systems however, we will take a short detour via the dielectric and collective excitation properties of one of these materials - armchair graphene nanoribbons. Although not entirely unrelated to the optical properties of graphene, these results stand alone as a potentially exciting new field of research for graphene, putting armchair graphene nanoribbons in a class of only a couple of materials (together with 3He and 4He) that exhibit a roton-like mode in their collective excitation spectra under no external magnetic field.

Chapter 2

Dielectric Properties of Graphene Systems

The dielectric properties of single layer graphene, bilayer graphene, Dirac graphene nanoribbons, and zig-zag armchair nanoribbons have been calculated in detail elsewhere (28; 29). Here, we are interested primarily in non-Dirac armchair nanoribbons, although we will present results for Dirac ones as well, for comparison. The results we obtain here for these finite-gap armchair ribbons were neglected in the previous two reports as they were based on expansions of the Dirac Hamiltonian which can't reproduce the fuller energy range results we are here concerned with. However, before probing these systems, we must introduce the dielectric function and collective excitations.

2.1 Dielectric Function

Consider the diagram shown in figure 2.1. The interaction in question (in this case the electron-electron interaction) is represented by a wavy line. In the most bare interaction form, the second quantised interaction Hamiltonian in momentum space for the Coulomb interaction is given by the familiar form

$$H_I = \sum_{s_1, s_2, s_3, s_4, \mathbf{k}_1, \mathbf{k}_2, \mathbf{k}_3, \mathbf{k}_4} \langle \mathbf{k}_1, s_1 | \langle \mathbf{k}_2, s_2 | v_{\mathbf{q}} | \mathbf{k}_3, s_3 \rangle | \mathbf{k}_4, s_4 \rangle c_{\mathbf{k}_1, s_1}^\dagger c_{\mathbf{k}_2, s_2}^\dagger c_{\mathbf{k}_3, s_3} c_{\mathbf{k}_4, s_4} \quad (2.1)$$

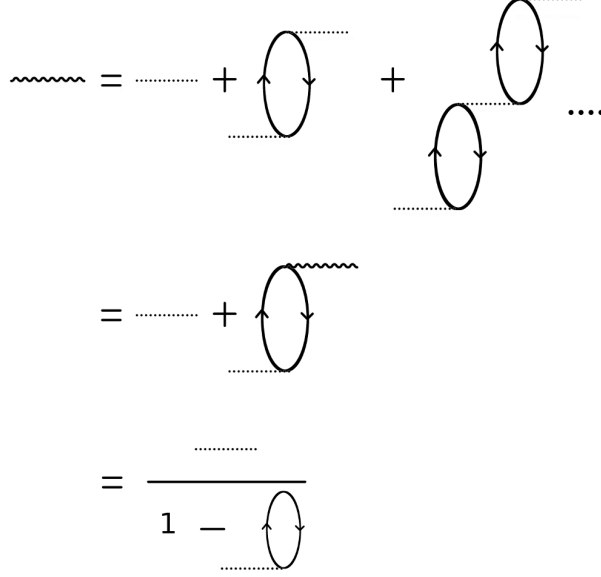


Figure 2.1: A hand waving approach to the screened interaction of an electronic system. The infinite sum of intermediate interactions leads to a denominator which is the RPA dielectric function of the system.

Which, neglecting exchange, becomes

$$H_I = \sum_{s,s',\mathbf{k},\mathbf{q}} F_{s,s'}(\mathbf{k}, \mathbf{q}) v_{\mathbf{q}} c_{\mathbf{k}+\mathbf{q},s_1}^\dagger c_{\mathbf{k}'-\mathbf{q},s_2}^\dagger c_{\mathbf{k}',s_3} c_{\mathbf{k},s_4} \quad (2.2)$$

Where $F_{s,s'}(\mathbf{k}, \mathbf{q}) = \langle \mathbf{k} + \mathbf{q}, s | \mathbf{k}, s \rangle \langle \mathbf{k}' - \mathbf{q}, s' | \mathbf{k}', s' \rangle$.

Treating electron-electron interactions by this simple model neglects intermediate scatterers. For instance, two electrons may scatter via a third electron, (ie. electron 1 scatters with electron 2, which in turn scatters electron 3). Neglecting intermediate interactions removes, potentially, a significant number of events. There are many other intermediate interactions, including vertex corrections, exchange, phonon-modulated interactions etc. We will restrict our attention to the first case. This is shown diagrammatically in figure 2.1. The bubble represents a density fluctuation due to the intermediate scattering event. In this way, we can build up a screened interaction which includes an infinite number of intermediate scattering events. This infinite sum can be conveniently expressed in terms of a single loop and a bare interaction as shown by the ‘algebra’ in figure 2.1. A more formal derivation has been given many times (30).

Algebraically, the single loop represents the polarizability of a system, and is given by the Green's functions

$$G_{\mathbf{k}+\mathbf{q},\lambda_1}(\xi_l + \alpha_m)G_{\mathbf{k},\lambda_2}(\xi_l) \quad (2.3)$$

Whose l summation can be evaluated by the integral equation and residue theorem using the standard approach, such that

$$\begin{aligned} & \int dz \left(\frac{1}{z + \alpha_m - \epsilon_{\mathbf{k}+\mathbf{q},\lambda_1}} \right) \left(\frac{1}{z - \epsilon_{\mathbf{k},\lambda_2}} \right) \\ &= n_F(\epsilon_{\mathbf{k}+\mathbf{q},\lambda_1}) \left(\frac{1}{\epsilon_{\mathbf{k}+\mathbf{q},\lambda_1} - \epsilon_{\mathbf{k},\lambda_2} - \alpha_m} \right) + n_F(\epsilon_{\mathbf{k},\lambda_2}) \left(\frac{1}{\epsilon_{\mathbf{k},\lambda_2} - \epsilon_{\mathbf{k}+\mathbf{q},\lambda_1} + \alpha_m} \right) \end{aligned} \quad (2.4)$$

The two terms have the same denominator, and so the final form is given upon analytic continuation ($\alpha_l \rightarrow \alpha + i\eta$) by

$$\Pi(\mathbf{q}, \alpha) = \int d\mathbf{k} \frac{n_F(\epsilon_{\mathbf{k}+\mathbf{q},\lambda_1}) - n_F(\epsilon_{\mathbf{k},\lambda_2})}{\epsilon_{\mathbf{k}+\mathbf{q},\lambda_1} - \epsilon_{\mathbf{k},\lambda_2} - \alpha + i\eta} \quad (2.5)$$

And so we have the dynamic dielectric function

$$\epsilon(\mathbf{q}, \omega) = 1 - v_{\mathbf{q}}\Pi(\mathbf{q}, \omega) \quad (2.6)$$

The most important use we will have for this equation is to find its zeros. These describe the collective excitation spectra of a system under some given perturbation.

In this thesis we are only concerned with the dielectric properties and collective excitation spectra of one type of graphene system: armchair graphene nanoribbons. As already mentioned, at the time the research was undertaken, the dielectric properties of 2D graphene had already been calculated (28), as well as GNRs (28; 29). The latter explains that in the case of zig-zag GNRs, there is no collective excitation spectra due to surface states. In the case of armchair GNRs however, both works adopt approximations that miss some of the important physics of the problem, and so they miss an important result: the existence of a roton-like mode in the collective excitation spectra of a subclass of non-Dirac armchair graphene nanoribbons (31).

2.2 Collective Excitation Spectra of Armchair Graphene Nanoribbons

Landau was the first to predict minima and maxima in the collective excitation spectrum of liquid ^4He . He did this by an incredible intuitive extrapolation from the known specific heat of the fluid (32). Feynman extended this work into quantum theory, producing a qualitatively accurate picture of the physics behind what he coined the ‘roton’. This, he developed into the theory of superfluidity (33; 34). Since this seminal work, ^4He has been studied extensively, and superfluidity has become a prominent entity in Bose-Einstein condensate research.

The existence of a magneto-roton mode in a two dimensional electron gas (2DEG) under a magnetic field was later found by Girvin and coworkers (35; 36). Since then, several materials with magneto-roton modes have been found, including graphene (37).

These systems have provided a rich playing field for the investigation of elementary excitation interactions (32; 38; 39; 40), and have played an important role in the development of contemporary quantum theory, and in particular, the quantum Hall effect. The question of what a roton *actually is* however, remains under dispute.

In this chapter we reveal that a new roton-like mode is expected to exist in a number of graphene nanoribbons. Aside from liquid Helium, this is the only material we are aware of which displays a roton-like mode in the absence of an external magnetic field. Interestingly, it is found that only non-Dirac armchair ribbons exhibit this peculiar new mode. The collective excitation spectrum of Dirac armchair ribbons is, as expected, similar to that found in a metal.

As stated earlier, we define the dielectric function as

$$\epsilon_{\text{RPA}}(q, \omega) = 1 - v_q \Pi(q, \omega) \quad (2.7)$$

Where $v_q = 2e^2 K_0(q|x - x_0|)$ is the Fourier transform of the Coulomb potential at x due to a charge at x_0 , where $K_0(x)$ is the modified Bessel function of the second kind. $\Pi(q, \omega)$ is the polarizability, which is a measure of the density fluctuation

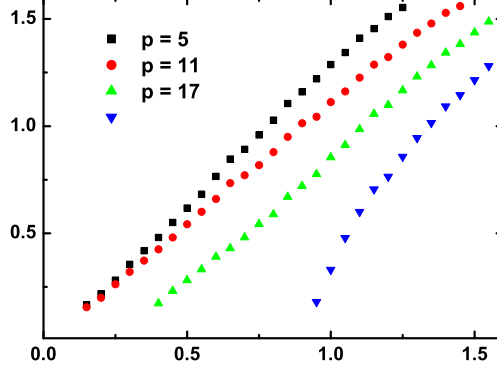


Figure 2.2: The collective excitation spectrum for Dirac armchair ($q = 1$) ribbons. The linear behaviour akin to collective excitation in metals is present for low widths, and low momentum transfers, as expected. At higher transfers and widths, the non-metallic subbands are no longer suppressed and cause the spectra to become curved.

due to an excitation of energy ω , and momentum transfer q , and is given by

$$\Pi(q, \omega) = \sum_{i,j} \int dk g_s |F_{i,j}(k, q)|^2 \frac{n_F(\epsilon_{k+q,i}) - n_F(\epsilon_{k,j})}{\epsilon_{k+q,i} - \epsilon_{k,j} - \omega} \quad (2.8)$$

Where g_s is the spin degeneracy, $F_{i,j}(k, q) = \langle k+q, i | k, j \rangle$ is the transition matrix element between subbands i and j with wavevectors $k+q$ and k respectively, $\epsilon_{x,n}$ is the energy at wavevector x of the n^{th} subband, and $n_F(x)$ denotes the familiar Fermi-Dirac distribution function. The collective excitation spectrum is found by the zeroes of the dielectric function (both real and imaginary parts), and can be viewed by $S = \Im \frac{1}{\epsilon_{\text{RPA}}}$.

The collective excitation spectra are plotted in Figures 2.2 and 2.3 for Dirac and non-Dirac armchair nanoribbons respectively. The armchair ($q = 1$) ribbons with Dirac energy dispersions are those for which $p+q \in 3N$, that is $p = 2, 5, 8 \dots$. The collective excitation spectrum in the case of Dirac and non-Dirac ribbons varies greatly due to the difference between zero and finite bandgap materials.

Figure 2.2 shows the collective excitation spectrum for Dirac armchair ribbons ($p + q \in 3N$). The excitation dispersion is found to be linear in general for

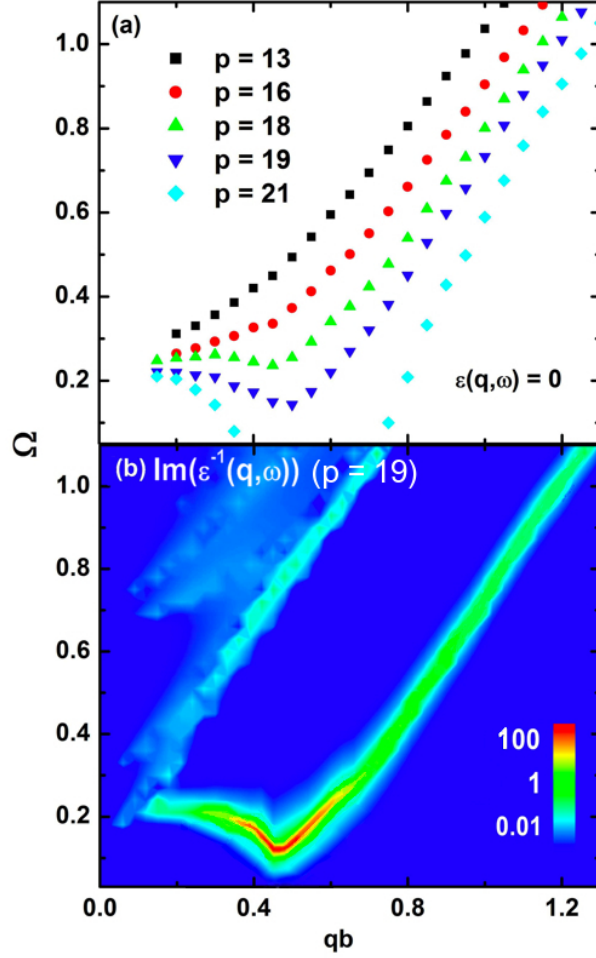


Figure 2.3: Top: The collective excitation spectrum for non-Dirac armchair ($q = 1$) ribbons. The roton mode emerges here for $p = 18$, and for $p \geq 21$ there is a region where no excitations occur. Bottom: The frequency and wavevector dependent intensity distribution for a non-Dirac armchair (19,1) ribbon.

small momentum transfers and small widths. This is due to the lowest energy metallic Dirac subband, and is in good agreement with the usual collective excitation spectra of metals. For higher momentum transfers and greater widths however, the non-metallic, higher energy subbands become significant, and cause the curvature of the excitation spectrum. Also interesting is that with increasing width, the low energy excitations begin to occur at greater momentum transfers. This leads to a momentum gap in the excitation dispersion. The widths where this begins to occur correlates well with the widths where the emergence of the roton modes for non-Dirac ribbons is observed, as discussed below.

In figure 2.3(a) we present the collective excitation spectra for non-Dirac armchair ribbons. For very small widths, the excitation spectrum is monotonic increasing. As the width increases however, a part of the spectrum begins to plummet downwards. The roton mode emerges here for $p = 18, 19$. There is a distinct minimum in the excitation spectrum at $qb = 0.45, 0.5$ with an energy gap of $\Delta = \hbar\omega/t = 0.24, 0.14$. By further increasing the width, it is found that the minimum disappears such that a region develops where there is no excitation spectrum, and beyond that, the spectrum follows the regular $\log(q)$ -type relationship.

The gradient of the excitation spectrum determines the group velocity of the collective excitations. At the minimum of the curve then, the roton mode R will have finite energy and momentum, but zero velocity. The modes to the left of the roton minimum (denoted by R_-) are also rather peculiar, having a negative group velocity. Since there are no excitations allowed at lower energies than the roton mode, there is no ‘phonon-like’ mode from the equivalent discussion of superfluid helium, and the excitation population would be dominated by the zero velocity roton modes, and R_- and R_+ states.

For $p \geq 21$ non-Dirac armchair nanoribbons, we observe still more peculiar collective excitation spectra. These ribbons do not exhibit a roton-like minimum in their spectra, but they do have extremely low energy R_- modes with very high group velocities. These modes are expected to be quite significant in the determination of the electronic and transport properties of this subclass of armchair graphene nanoribbons. Beyond these R_- modes there is a region with no excitations until the re-emergence of an R_+ mode at higher momentum transfers, which

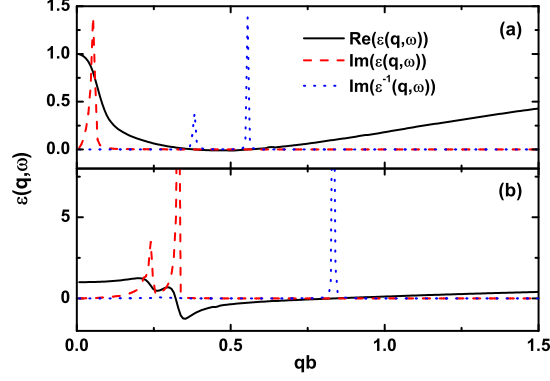


Figure 2.4: The dielectric function of the armchair ribbon exhibiting a roton mode is shown here for two values of $\hbar\omega/t$. (a) is that for $\hbar\omega/t = 0.35$ which is within the roton section of the spectrum. The two excitation peaks are clearly visible. For higher energies, the imaginary part is no longer negligible, and suppresses the excitations. This is seen in (b) where $\hbar\omega/t = 1$. Note that the collective excitation peaks have been normalized by the maximum magnitude of the real and imaginary parts of ϵ .

also have an extremely high group velocity for low energy excitations. These R_{\pm} modes are similar to their phonon-like counterparts in liquid ^4He , having an approximately linear dispersion for small energies. However unlike in ^4He , there are both forward propagating and backward propagating modes observed here.

Further to the existence of the roton mode, is the intensity carried by the mode $\text{Im}[1/\epsilon(\omega, q)]$. In figure 2.3(b), we have shown that over the whole ω - q space, almost all intensities are located on the collective modes. Furthermore, the intensity at the roton minimum is the strongest, indicating that the modes are strongly coupled with the incident light.

Figure 2.4 shows the dielectric function for the $p = 19$ armchair ribbon for two different values of $\hbar\omega/t$. The zeroes can be clearly observed, and $\Im(1/\epsilon(q, \omega))$ shows the corresponding excitation strength. The unusual aspect of the graphene ribbons is easily seen from this figure. For particular energies, the imaginary part of the dielectric function is negligible not only for one zero of the real part of the dielectric function (as is usually the case, and can be seen in Fig. 2.3(b),

but for both zeros. It is this fact that causes the double excitation peak for $\hbar\omega/t = 0.18$ shown in Fig. 2.3(a). As the energy is increased, the imaginary part of the dielectric function returns to its usual behaviour, and only one excitation is observed.

There is direct correlation between the inverse dielectric function and the static structure factor $S(q)$ (30). This correlation has been used by both Bijl-Feynman and Girvin *et al* to develop their theories of roton modes in ^4He and 2DEGs. A direct consequence of the roton minimum is a peak in the static structure factor. Since $S(q)$ is the space Fourier transform of the pair correlation function $G(r, 0)$, the maximum of $S(q)$ which occurs at q_{roton} indicates that in these non-Dirac ribbons, the strongest pair correlation occurs at a finite separation of $y_0 = 1/q_{\text{roton}}$.

In conclusion a roton-like minimum in the collective excitation spectrum of certain non-Dirac armchair graphene nanoribbons is predicted. These peculiar quasi-particles are expected to shed further light on the nature of rotons in materials, and should lead to some very interesting properties of these particular ribbons. Graphene nanoribbons can be added to an extremely small subclass of materials that exhibit roton-like collective excitation spectra.

Chapter 3

Optical Conductivity of Graphene

The Kubo formula for optical conductivity is given by the current-current correlation function in an electromagnetic field (30):

$$\sigma_{\nu,\kappa}(\omega) = \frac{1}{\omega} \int_0^\infty dt e^{i\omega t} \langle [J_\nu(t), J_\kappa(0)] \rangle \quad (3.1)$$

Where the time dependence of an operator is given by $O(t) = e^{-iHt} O(0) e^{iHt}$. This form of the Kubo formula allows us to calculate the longitudinal conductivities σ_{xx} and σ_{yy} and the transverse conductivity $\sigma_{xy} = \sigma_{yx}$. The current operator matrix elements are given by

$$J_\nu^{i,j} = ev_\nu^{i,j} = e \frac{\partial H^{i,j}}{\partial k_\nu} \quad (3.2)$$

The commutator can then be expressed as

$$\langle [J_\nu(t), J_\kappa(0)] \rangle = e^{i\omega t} \sum_{\lambda_1, \lambda_2} \langle \mathbf{k}', \lambda_1 | \frac{\partial \mathbf{k}_\nu}{\partial \hat{H}} | \mathbf{k}, \lambda_1 \rangle \langle \mathbf{k}, \lambda_2 | \frac{\partial \mathbf{k}_\mu}{\partial \hat{H}} | \mathbf{k}, \lambda_2 \rangle c_{\mathbf{k}', \lambda_2}^\dagger c_{\mathbf{k}, \lambda_2} c_{\mathbf{k}, \lambda_1}^\dagger c_{\mathbf{k}', \lambda_1} \quad (3.3)$$

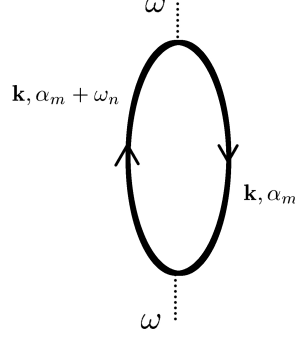


Figure 3.1: The single loop diagram describing the linear optical conductivity in the absence of interactions.

Where $H = \sum_{\mathbf{k}, \lambda_1} \hat{H} c_{\mathbf{k}, \lambda_1}^\dagger c_{\mathbf{k}, s}$. The creation/annihilation operators form just one connected diagram, a single loop as shown in 3.1 with Green's functions

$$G_{\mathbf{k}, \lambda_1}(\xi_l + \omega_n) G_{\mathbf{k}, \lambda_2}(\xi_l) = \sum_{l, n} \left(\frac{1}{\xi_l + \omega_n - \epsilon_{\mathbf{k}, \lambda_2}} \right) \left(\frac{1}{\xi_l - \epsilon_{\mathbf{k}, \lambda_1}} \right) \quad (3.4)$$

Which, converting the l summation to an integral over the complex plain has residues

$$\sum_l \left(n_F(\epsilon_{\mathbf{k}, \lambda_1}) \frac{1}{\epsilon_{\mathbf{k}, \lambda_2} - \epsilon_{\mathbf{k}, \lambda_1} - \omega_n} + n_F(\epsilon_{\mathbf{k}, \lambda_2}) \frac{1}{\epsilon_{\mathbf{k}, \lambda_1} - \epsilon_{\mathbf{k}, \lambda_2} + \omega_n} \right) \quad (3.5)$$

Which, on analytic continuation gives

$$\frac{n_F(\epsilon_{\mathbf{k}, \lambda_2}) - n_F(\epsilon_{\mathbf{k}, \lambda_1})}{\epsilon_{\mathbf{k}, \lambda_2} - \epsilon_{\mathbf{k}, \lambda_1} - \omega + i\eta} \quad (3.6)$$

And so the optical conductivity with no intermediate interactions is given by

$$\frac{(F_{12}(\mathbf{q}) F_{21}^*(\mathbf{q})) n_F(\epsilon_{\mathbf{k}, \lambda_2}) - n_F(\epsilon_{\mathbf{k}, \lambda_1})}{\epsilon_{\mathbf{k}, \lambda_2} - \epsilon_{\mathbf{k}, \lambda_1} - \omega + i\eta} \quad (3.7)$$

Where $F_{12}(\mathbf{q}) = \langle \mathbf{k}', \lambda_1 | \frac{\partial \mathbf{k}_\nu}{\partial H} | \mathbf{k}, \lambda_2 \rangle$ is the current transition matrix element. Intra-subband transitions are forbidden in this case since there is no momentum shift. So only inter-subband transitions will be considered.

3.1 Single Layer Graphene

Proceeding then, with single layer graphene with the full energy formalism, the current operators are readily solved for inter-subband transitions, giving

$$\begin{aligned} J_x &= \frac{-2ev_F a}{\sqrt{3}} \sum_{\mathbf{k}} \left(\frac{\cos k_y - \cos \sqrt{3}k_x/2 \cos k_y/2}{\sqrt{3 + \alpha(\mathbf{k})}} \right) c_{\mathbf{k},s}^\dagger c_{\mathbf{k},-s} \\ J_y &= \frac{-2ev_F}{\sqrt{3}} \sum_{\mathbf{k}} \frac{\sin \sqrt{3}/2 k_x \sin k_y/2}{\sqrt{3 + \alpha(\mathbf{k})}} c_{\mathbf{k},s}^\dagger c_{\mathbf{k},-s} \end{aligned} \quad (3.8)$$

Proceeding with the solution obtained above for the Green's functions then, we obtain

$$\begin{aligned} \sigma_{xx} &= \frac{e^2 v_F^2 a}{\pi^2 \omega} \int d\mathbf{k} \frac{(\cos k_y - \cos \sqrt{3}k_x/2 \cos k_y/2)^2}{3 + \alpha(\mathbf{k})} \\ &\quad \times \left(\frac{n_F(\epsilon_{\mathbf{k},\lambda_1}) - n_F(\epsilon_{\mathbf{k},\lambda_{-1}})}{\omega + 2t\sqrt{3 + \alpha(\mathbf{k})}} \right) \\ \sigma_{yy} &= \frac{e^2 v_F^2}{3\pi^2 \omega} \int d\mathbf{k} \frac{(\sin \sqrt{3}/2 k_x \sin k_y/2)^2}{3 + \alpha(\mathbf{k})} \\ &\quad \times \left(\frac{n_F(\epsilon_{\mathbf{k},\lambda_1}) - n_F(\epsilon_{\mathbf{k},\lambda_{-1}})}{\omega + 2t\sqrt{3 + \alpha(\mathbf{k})}} \right) \end{aligned} \quad (3.9)$$

This is readily solved numerically for any given temperature or chemical potential. These results have been presented elsewhere (20), but with a slightly different form for J_y . Equation 3.9 is given shown here for comparison with the results of subsequent chapters. Within the Dirac regime the results are even easier to obtain as the current operators are constants. This leads to a constant, isotropic ‘universal’ conductivity $\sigma_0 = e^2/4\hbar$. This is the value by which all other optical conductance results will be normalised.

3.2 Bilayer Graphene

The ‘universal conductance’ reported in the last section is both a dc and an ac phenomenon (although it must be pointed out that the static and dynamic cases differ by a factor of π). As discussed earlier, it is a direct result of the linear energy dispersion of graphene. Linear subbands imply both a constant density of states as well as consistent transition matrix elements, which means that for as long as the linear (Dirac) approximation is valid, the conductance is a constant. In the ac case, the value of the universal conductance of single layer graphene is $\sigma_1 = e^2/4\hbar$. In the layered case, a standard benchmark is simply $\sigma_n = n\sigma_1$. For a system of layers which are completely uncoupled, this will clearly be true. However, this is not generally accurate, as the interlayer coupling leads to a subband curvature caused which in turn leads to a non-constant conductivity. This raises an important question: in what energy range is $\sigma_n = n\sigma_1$ applicable?

Another question is: how many intersite coupling terms (interlayer and intralayer) need to be included to replicate experimental results. In this chapter we include three interlayer coupling terms (more than anyone else in the field) as well as the next nearest neighbour interlayer coupling (which is almost universally neglected).

The infrared conductance of BLG has been measured by several groups (18; 41). These results rely upon the effects of an induced gate voltage on the band-structure, and all assume a discrepancy in onsite energy between the two layers. In ref. 17, Mak et al present the ‘expected’ IR conductance without the latter assumption, and find that it differs markedly from their experimental results. This demonstrates the need to assume an energetic discrepancy between the two layers in BLG. Our theoretical results, however, show a strong correlation to the results in ref.16 and 17, demonstrating that while an energetic discrepancy may exist, it is not necessary in describing the IR response observed experimentally.

In this section it is shown that the interplay of the coupling terms included leads to a significant deviation in the behaviour of the conductance at low frequencies, which can, in turn, be tuned by electronic doping. For this reason we will consider two important samples: Intrinsic (ie. undoped and unbiased) bilayer graphene, as well as a sample which is doped so as to drag the chemical

potential to the bands crossing point (see fig.2). In the important ultraviolet frequency band, this interplay leads to significant conductance anisotropy, i.e., the absorption along the zig-zag direction is around 50% stronger than that along the armchair direction.

The eigenvalues in BLG were calculated in chapter 1 and are

$$\epsilon_{s,s'} = t'(\epsilon_{\text{SLG}}^2 - 3) + s\sqrt{\epsilon_{\text{SL}}^2 + \frac{\gamma_{12}^+}{2} + s'\sqrt{\Gamma}} \quad (3.10)$$

Where

$$\Gamma = \epsilon_{\text{SL}}^2 \gamma_{12}^+ + \frac{(\gamma_{12}^-)^2}{4} + 2\gamma_1 \gamma_3 \epsilon_{\text{SL}}^2 \text{Re}(H) \quad (3.11)$$

And $\gamma_{12}^\pm = \gamma_3^2 \epsilon_{\text{SL}}^2 \pm \gamma_1^2$, with $s, s' = \pm 1$, and ϵ_{SL} are the regular eigenvalues for the SLG system given as

$$\epsilon_{\text{SLG}} = t \left(1 + 4 \cos(ak_x/2) \cos(ak_y/2\sqrt{3}) + 4 \cos^2(ak_x/3) \right)^{\frac{1}{2}}, \quad (3.12)$$

From this result we see that there are two conduction bands and two valence bands which are confined above and below the line $\epsilon_{s,s'} - t'(\epsilon_{\text{SLG}}^2 - 3) \approx 3t'$ near the K points. This simple result will form the basis for much of the discussion to follow.

In Fig.3.3. we examine the optical conductance of intrinsic bilayer graphene. Near the higher energy valley points, the optical conductance exhibits two extrema, similar to the single peak found in single layer graphene (20; 21). These peaks correspond to the two dominant vertical transitions between the two symmetric pairs of saddle points. The Joint Density of States in these valleys reaches a cusp-like maximum which leads to the extrema in the conductance. These two energy peaks are separated by an amount $\hbar\omega = 2\gamma_1$, as expected from the bandstructure calculations. Finally note that the conductance along the zig-zag direction is generally larger than that along the armchair direction, especially at larger energies.

Fig.3.4. shows the low energy optical conductivity of the intrinsic sample from the grey shaded region of Fig.3.3., as well as a sample doped to shift the

Fermi level to the bands crossing point. The longitudinal conductance varies greatly when including a non-zero NNN interaction in the model, and the effect is equivalent to doping when NNN interactions are included. The effect of the dominant interlayer term γ_1 (ie. setting $\gamma_3 = \gamma_4 = t' = 0$) at low energies has been reported recently (42). This result has been retrieved in our NNN inclusive result by doping the sample so as to force the Fermi energy to coincide with the bands-crossing points. In the intrinsic case however, the previously reported result is entirely suppressed, and replaced by an approximately $2\times$ larger, rounded peak, followed by a significant trough. This correlates well with the behaviour observed in IR experiments (18; 41), although without the added effects of an induced gate voltage. In the doped sample, electron transitions from either valence band into either conduction band are allowed, which is equivalent to intrinsic bilayer graphene calculations with NNN coupling neglected, as shown in Fig.2. The intrinsic bilayer sample with NNN interactions included in the model, however, suppresses transitions from the upper valence band to the lower conduction band, since they are both filled, and yet a new set of transitions become allowed between the two conduction bands. These similar bands are separated by an approximately constant factor of γ_1 , which leads to the large peak centred at $\hbar\omega \approx \gamma_1$ in the intrinsic bilayer sample. The feature is in striking contrast with that of SLG. For SLG, the effect of the NNN coupling is to suppress the universal conductance at low frequencies (21). As is clearly seen in Fig.3.4, for BLG the interplay of the interlayer coupling and the NNN coupling can suppress the conductance at low frequencies. However, it also induces a strong absorption peak in the far infrared before the onset of the universal conductance.

For this reason, the low energy approximations of the behaviour of bilayer graphene are generally more relevant to carefully doped samples, with the intrinsic bilayer properties being drastically affected by the next nearest neighbor hopping and additional interlayer terms. Whilst the existing low energy formalisms are capable of accurately reproducing the low energy bandstructures with these terms, in intrinsic bilayer graphene those bands will be completely filled, and predicted effects will be suppressed. In order to empty one of the two inner bands, the system must be doped (or biased) in some way, and to a very specific level. Furthermore, when using existing theories to explain experimental

results, it needs to be noted that an energetic discrepancy between layers, as well as the inclusion of a gate voltage, both cause some similar effects to the inclusion of the NNN interaction. All of these will therefore need to be accounted for when explaining any experimental result.

Furthermore, the conductance anisotropy observed in Figures 3.3 and 3.4, which is prominent even in the IR region when γ_4 and t' are both included, makes the polarization of the photon beam in experiments a relevant parameter. This orientation dependence of the optical conductance makes determination of the orientation of a BLG flake possible, and also makes BLG a potential partial polarizer. The doping dependence of the low energy conductance anisotropy makes this feature quite versatile. We note, however, that this anisotropy is stronger when the chemical potential lies above the Fermi level than when it is below it. This partly explains the effect noticed by Li et al (18) which is that the bias of the gate voltage breaks electron-hole symmetry.

Finally, as we have already mentioned, the value of the ‘universal’ conductivity is a topic of great interest at the moment. According to these results, which have been calculated from the most robust interlayer and intralayer model adopted to date, the value of the universal conductivity for bilayer graphene is $\sigma_2 = 2\sigma_1$ where $\sigma_1 = e^2/4\hbar$ is the universal optical conductivity of single layer graphene defined earlier. The range over which this value is applicable is greatly affected by the inclusion of the NNN interaction in numerical calculations, and is strongly dependent on the electronic doping of a real sample. In particular, the NNN interaction causes the very low energy optical response to become negligible, and around the observed peak, the optical conductance is $\sigma_{\text{peak}} \approx 5.5\sigma_1$.

From our results, it is clear that the universal conductivity is an approximation that applies only within certain energy ranges and is strongly dependent on sample doping. For intrinsic BLG, the energy ranges where $\sigma_2 \approx 2\sigma_1$ is $\hbar\omega > 0.4t$. However, this quickly becomes inaccurate with increasing energy, especially for σ_{xx} . For a doped sample however, the approximation can be much more appropriate. In this case the applicable energy ranges are $\hbar\omega < 0.13t$, and $\hbar\omega > 0.25t$.

Before concluding, we mention in passing that the exact location of the Fermi energy is not widely agreed upon as its determination involves many factors. Within our model a Fermi level could be determined by half-filling the π orbitals

via the DOS. This is by no means an accurate method, and a precise determination of the Fermi level requires a more fundamental approach. Therefore it is outside the scope of the present work to attempt to determine the Fermi energy, but instead we choose the natural $\epsilon = 0$ point that arises from the tight-binding formalism adopted. However, the exact location of the Fermi energy is largely irrelevant. The breaking of electron hole symmetry induced by NNN interactions assures that the Fermi energy will not coincide with the bands-crossing points by at least an amount of the order of t' . For Fermi energies above or below the neighborhood of these points, the low energy peak conductance reported here varies in magnitude from $\approx 5.5 \rightarrow 6.1$, and the variation of the peak position is indetectable within acceptable numerical accuracy. The former can be clearly seen in the inset to Fig.5. Doped samples where the Fermi energy does not coincide with the bands-crossing points have very similar optical responses to intrinsic BLG.

In conclusion, we have studied the longitudinal optical conductivity of BLG with the inclusion of all relevant interlayer coupling terms and next nearest neighbor intralayer interactions. The optical conductivity exhibits double peak resonance separated by an amount $2\gamma_1$ and is centered around $\hbar\omega = 2t$. At low energies, the NNN interaction leads to entirely new behaviour of the optical conductivity. The results obtained without NNN coupling, however, can be retrieved by appropriate electronic doping. The interplay of the NNN- γ_4 couplings were found to lead to significant low energy conductance anisotropy which is strongly doping dependent. Finally, the value of the universal conductivity with the most robust formalism used to date has also been determined, and is given by $\sigma_2 = 2\sigma_1$. The applicability of this approximation, however, is restricted to certain energy ranges and is strongly doping dependent. These results will be crucial to the experimental testing of accepted theories on bilayer graphene, and will be useful for potential low energy electronic and photonic applications of bilayer graphene.

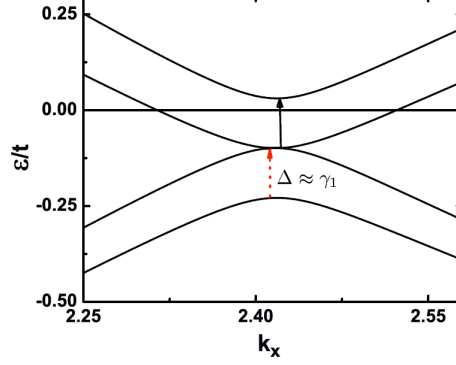


Figure 3.2: The k_x dependence of the bandstructure near the K/K' points. The effect of the NNN coupling is to shift the Fermi level (here $\epsilon_F = 0$) off the bands-crossing points. The other noticeable effect here is that of the dominant interlayer coupling γ_1 which causes the gap of $\Delta \approx \gamma_1$ between similar bands. The red dashed arrow represents a transition which is permitted in an intrinsic bilayer calculation if NNN coupling is neglected in the model, but becomes forbidden when it is included. The black solid arrow is the opposite: a previously forbidden transition becomes allowed when NNNs are included in the model. The effect of doping is to raise or lower the Fermi level, making the inclusion of NNNs partly equivalent to doping.

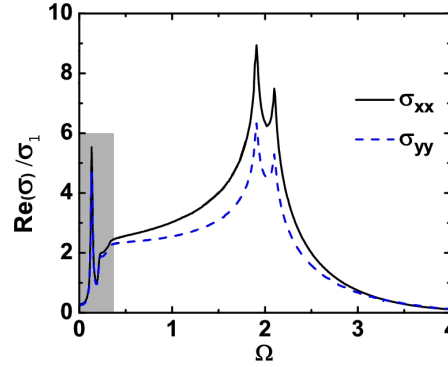


Figure 3.3: The optical conductance (in units of $\sigma_1 = e^2/\hbar$) vs the normalized frequency $\Omega = \hbar\omega/t$ for bilayer graphene. Generally, σ_{xx} (the zig-zag direction) has a larger optical response than σ_{yy} (the armchair direction). When NNN and γ_4 are neglected, and at low energies, $\sigma_{xx} = \sigma_{yy}$. This is no longer the case here, with NNNs and γ_4 included. The grey shaded area indicates the low energy region plotted in Fig.3.4.

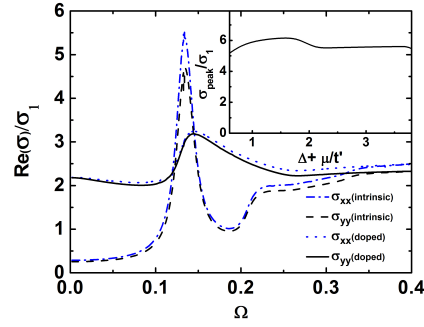


Figure 3.4: The low energy optical conductance at two different doping levels. The blue dash-dot and black dashed lines are the optical conductance of intrinsic BLG along the x and y directions respectively. The black solid and blue dotted lines represent the optical conductance of a sample which is doped such that the chemical potential is shifted to the bands crossing point. The NNN- γ_4 coupling causes a new peak to emerge, and suppresses the previously reported one. This new peak is much larger and shifted to a lower photon energy. In a suitably doped sample, however, the $t' = 0$ (no NNN) peak has been retrieved by an effective shifting of the Fermi level. The inset shows the sensitivity of the intrinsic zig-zag peak to the Fermi energy. Δ is the bands crossing point. If the Fermi energy lies at least $0.6t'$ from the bands-crossing points (in either direction), the peak conductance lies within 15% of our result.

3.3 Graphene Nanoribbons

As in the case of bilayer graphene, the nanoribbon optical conductances are calculated numerically from scratch. This is due to the complexity of the problem. In general, the nanoribbon eigenvalues and eigenvectors have not been calculated exactly.

Nevertheless, the optical conductance is readily obtained numerically for any arbitrary width or chirality of ribbon.

These have been calculated at length by others (43; 44), and so were not applicable to this thesis. However, they will be presented in part in the next section in order to introduce the significant enhancement obtained in bilayer ribbons. Also, we have reported that in the presence of a magnetic field, the optical properties of GNRs can be tuned to respond strongly in the THz-FIR regime (44). This is primarily the work of a collaborator and so it is not appropriate to present it here.

3.4 Layered Graphene Nanoribbons

The optical responses presented so far for 2D graphene systems has been relatively weak. The ‘universal’ conductance for single layer graphene $\sigma_0 = e^2/4\hbar$ corresponds to an absorption of $\approx 3\%$. The enhancement obtained when extending to two layers was, in general, $2\sigma_0$, and in parts of the spectrum was as much as $6\sigma_0$ depending on doping levels. Although not explicitly presented here, the optical conductance of graphene nanoribbons is not a continuum, but a set of resonant peaks due to van-Hove singularities in the density of states. The optical response of all ribbons remains very weak, with these peaks having approximately equivalent strength to the universal conductivity of graphene sheets(43). Despite the presense of van-Hove singularities, the reason for the still poor optical response is due to the relatively small interband transition amplitudes between valence and conduction subbands. Because of this, potential application of graphene structures in optoelectronics and photonics is severely limited.

However we demonstrate in this chapter, that there exists a sub-class of bilayer graphene nanoribbons (BLGNRs) which have an unusually strong optical conductance in the terahertz (THz) to far infrared (FIR) regime. The height of the conductance peak is about two orders of magnitude greater than the universal conductance of graphene sheets. We found that this sub-class of BLGNRs can be either armchair or chiral, but their energy dispersion near the Γ point must be that of a one-dimensional massless Dirac Fermion. This sub-class of graphene structures are the first systems to show such a strong optical response in the absence of any external field in the important frequency band of THz and FIR.

Moreover, it was recently reported that nanoribbons with widths less than 10nm have been successfully created in the lab (45). These ribbons were identified as single layer, bilayer, and trilayer ribbons. This remarkable experimental feat demonstrates that, although not yet recognized, the class of strutures reported can already be produced.

The construction of layered GNRs and their corresponding energy dispersions was described in chapter 1.

We will use the model system of $p = 2$ ribbons, the system with the smallest Hamiltonian matrix, to show the existence of a strong optical conductance peak

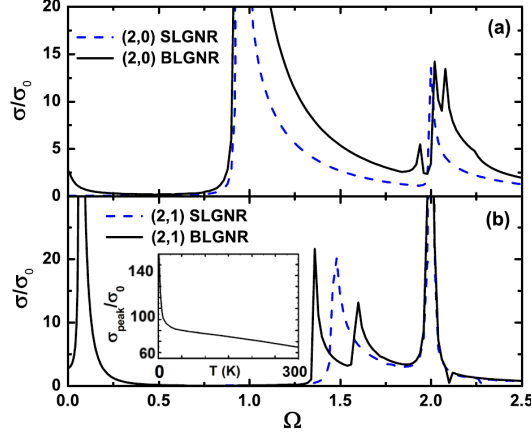


Figure 3.5: The optical conductivity for the ZZ-BLGNR (a) and the AC-BLGNR (b). The low energy activity in the bilayer ribbons is particularly significant, especially in the Dirac AC-BLGNR where the optical conductivity is approximately $150\sigma_0$. The temperature dependence of the large peak observed in all armchair bilayer ribbons is shown in the inset. The peak is robust all the way up to room temperature, decreasing rapidly to $\approx 80\sigma_0$ at $10K$ then decreasing very slowly with increasing energy.

at low frequencies. Our full numerical result has been obtained for the entire sub-class of ribbons.

We find here that the oscillator strength of the interband transition is strongly dependent on the properties of the energy dispersion at the zero-gap point. It will be shown that for ZZ-BLGNRs, where the zero gap position is at the K point and the two low energy dispersions are close to parabolic, the oscillator strength at low energy is very small. On the other hand, for AC-BLGNR, the zero gap position is at the Γ point. Furthermore, the two low energy dispersions are very close to linear (or a one-dimensional massless Dirac Fermion). Near the band minimum however, the bands are curved, displaying a rounded minimum as opposed to a sharp one. This has two effects, firstly it greatly increases the DOS at the band minimum, and secondly, the curvature allows transitions between non-symmetric bands (as was the case for 2D bilayer graphene in the preceding section).

The optical conductivity is calculated using the Kubo formula as usual, and

the results are normalized by the single layer universal conductivity given by $\sigma_0 = e^2/4\hbar$. We determine the dependence of the optical conductance on the ribbon widths and chiralities. In figure 3.5(a) we show that the optical conductivity for the ZZ-BLGNR exhibits a spike centered on zero energy. This spike occurs here because both low energy subbands approach zero energy at the Dirac-like points. In the SLGNR case, the velocity operator approaches a constant, which makes inter-symmetric-subband transitions forbidden. This is no longer the case in bilayer ribbons, and there is also now the possibility of low energy inter-non-symmetric-subband transitions.

Over the full energy spectrum, we see that some of the resonant peaks in the single layer optical conductivity spectrum have split into three peaks. This will not generally be the case. Most peaks will split into two as will be seen in the armchair case. However, near $\Omega = 1$, the subbands create a linear Dirac-like band structure with features similar to the Dirac point in the proceeding armchair case, as well as those observed in 2D bilayer graphene. This means that there are three possible energy transitions with high density of states. The central, primary peak corresponds to the original SLGNR peak, and the two secondary peaks, one below, and one above the original by an amount $\Omega = \gamma$, correspond to the new curved subbands which don't quite touch the degenerate point from the single layer case.

The optical conductance of armchair BLGNRs is shown in figure 3.5(b). In the AC case it peaks sharply at $\gamma/2$ and trails off because of the linearity of the band structure. In the armchair case, a peak is still observed as $\Omega \rightarrow 0$, but the peak at $\gamma/2$ is about 2 orders of magnitude stronger. This peak corresponds to vertical transitions between non-symmetric subbands which are far more probable than those between symmetric ones (see fig. 3.7 and subsequent discussion). This single low energy peak is larger than every other peak across the spectrum, and, as can be seen from the inset to figure 3.6(b), is robust across a wide range of relevant temperatures. Of course, the correction due to electron-phonon interactions must be considered with increasing temperature. However, the correction at low energies has been found experimentally and deemed negligible, and even for energies $> 1\text{eV}$, to be only a few percent (17). As the width of the ribbons increases, the strength of this peak remains approximately constant. This is an

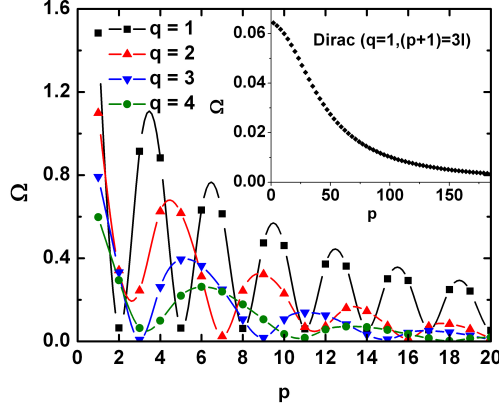


Figure 3.6: The width dependence of the energy of the low-energy peak for BLGNRs with $q = [1, 4]$. The strongest peaks occur in the lowest energy gaps in the Dirac armchair ribbons. The inset shows the width dependence of the band gap for Dirac BLGNRs with strong low energy optical response. This gap eventually disappears, but in the 2D limit with no edges, it re-emerges at γ .

effect which is peculiar to one dimensional ribbons, which reflects the consistency of the Dirac bandstructure with increasing width. In the case of an infinitely wide ribbon, the strong optical response is lost completely, settling at $\approx 4\sigma_0$ at $\Omega = \gamma$. This universally enhanced response for arbitrarily wide ribbons is a remarkable result which will certainly be instrumental in abolishing current limitations in implementing graphene based systems into optoelectronic and photonic devices.

At higher energies, the single peaks observed in AC-SLGNRs generally have split into two, and are separated by an amount $\approx 2\gamma$. This corresponds to two sets of symmetric transitions, the non-symmetric transitions being largely suppressed.

For $q > 1$ BLGNRs, the band gap between the two lowest energy symmetric bands varies from zero to 1eV . Similarly the non-Dirac AC-BLGNRs (ie $(p + q)/3 \notin I$), have varying band-gaps for the lowest energy subbands.

For a given type of BLGNR, the conductance peak position can be tuned with the ribbon width. Figure 3.6 shows the width dependence of the peak position in the THz/FIR regime. The peak position oscillates with the ribbon width. The amplitude of the oscillation is of the same order of magnitude as the average peak position, indicating a large range for tuning the resonance peak. The period of

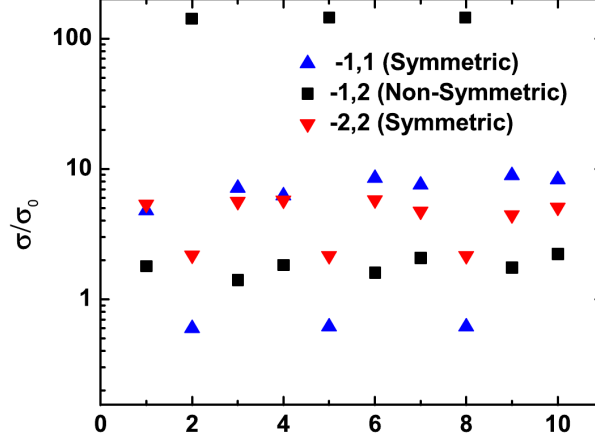


Figure 3.7: The p dependence of the low energy peaks for a $(p,1)$ BLG NR. In Dirac ribbons the symmetric transitions are suppressed and the non-symmetric ones dominate. For non-Dirac ribbons the opposite is the case. Notice that the strength of the peak in the Dirac cases is constant (within the specified computational accuracy of the calculation).

the oscillation increases with the chirality (q). The inset of figure 3.6 shows the width dependence of the energy gap for Dirac BLG NRs. This gap decreases as width increases making the location of the optical peak strongly width dependent. The strength of the peak, however, remains constant as discussed earlier. This makes Dirac bilayer graphene nanoribbons remarkably versatile in choosing the desired optical response energy without compromising on response strength. The bilayer ribbons that have recently been fabricated (45) correspond to $p < 100$ in our results. Furthermore, energy gaps in the THz regime correspond to bilayer ribbons with $p \geq 100$. This demonstrates that the structures in question already exist, and the gateway to graphene based THz devices is extremely close.

Figure 3.7 shows the width dependence of the magnitude of the low energy peak for the $(p,1)$ BLG NR. For $(p+1)/3 \in I$, the non-symmetric matrix element dominates, causing the single low energy peak. The low-frequency peak conductance for this class of BLG NRs is unusually strong having a value of approximately $150\sigma_0$, much stronger than the universal conductance of graphene sheets.(17) When the Dirac condition is not met however (ie $(p+1)/3 \notin I$), the

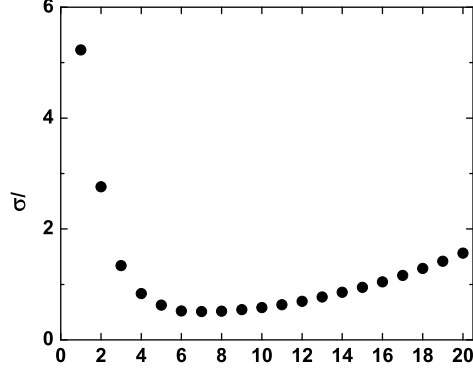


Figure 3.8: The width dependence of the magnitude of the low energy peak for the ZZ-BLGNRs decreases quickly with increasing width, and then increases steadily for $p > 6$.

symmetric matrix elements dominate, and the non-symmetric matrix elements are greatly suppressed, leading to a much weaker response to the low energy spectrum.

The width dependence of the strength of the low energy peak for ZZ-BLGNRs is given in Figure 3.8. For very narrow ribbons with $p < 6$ the peak quickly decreases in magnitude at a decreasing rate. For $p > 6$ however, the peak magnitude increases steadily, reflecting the low energy subband shape. As the width increases, the low energy subbands remain lower, which increases the DOS, allowing more transitions between subbands. For very narrow width ZZ-BLGNRs however, the curvature in the subbands is so high that the velocity operator allows strong coupling between the subbands, which makes the low energy magnitude very strong.

In summary, we have shown that the interplay of ribbon's chirality and the inter-ribbon coupling can lead to significant enhancement in optical response. We have identified a sub-class of BLGNRs where the inter-layer coupling causes a finite band gap in the energy minimum and induces strong inter-subband transitions. The distinct feature of this sub-class of BLGNRs is that they have a one dimensional massless Dirac Fermion dispersion near the Γ point. The peak conductance of this class of BLGNRs has a very large constant value of around

$150\sigma_0$, making them a class of materials for unique applications in optoelectronics. The simple picture behind this phenomenon is that the density of states for the 1D massless Dirac Fermions remains finite at zero energy, whereas that for the 2D massless Dirac Fermions in a graphene sheet vanishes. The remarkable role of the edge states is to cause the transition energy to decrease with increasing width, but not the magnitude of response. In the 2D limit however, with edge states removed, the strong optical response suddenly disappears completely.

These results open a gateway to the creation of graphene-based low energy photon devices. The ribbon width and chirality selection for various applications is crucial, as the optical responses of various ribbons change dramatically when these properties are varied.

3.5 Stretched Graphene

In this section we calculate both the longitudinal and Hall optical conductivity of single layer graphene which has been stretched along some direction. We find that stretching a single layer graphene sheet breaks the x-y isotropy, causing the conical Dirac bandstructure at the K points to have elliptical rather than circular cross sections. This leads to a discrepancy between the Fermi velocities along the armchair and zig-zag directions, which in turn alters the relative universal conductivities along each direction.

To model stretched graphene, we assume that the bonds will rotate relative to each other, but that the bond length remains constant. This approximation is equivalent to the first nearest neighbour approximation where next nearest neighbours are neglected. The first nearest neighbours are kept in their energetically minimum configuration, but next nearest neighbours are not. For large stretching magnitudes, the next nearest neighbour distance will approach the first, and this approximation will break down. However, graphene is a very stiff material, and breaks long before this condition is met. Therefore we restrict our attention to very small bond bending angles, with no bond rotation exceeding a couple of degrees. We model the system as described in chapter 1, where we obtain

$$\begin{aligned}\theta_1 &= F \sin 2\phi \\ \theta_2 &= F/2(\sin 2\phi + \sqrt{3} \cos 2\phi) \\ \theta_3 &= F/2(\sin 2\phi - \sqrt{3} \cos 2\phi)\end{aligned}\tag{3.13}$$

Where F is the magnitude of the stretching force, and ϕ is the chiral angle along which the force is applied.

The current operators are obtained, as usual, from $J_\nu = \langle \Psi | v_\nu | \Psi \rangle$, where

$\nu = x, y$, where $\hat{v}_\nu = \partial H / \partial k_\nu$. We obtain

$$\begin{aligned}
 J_x = \frac{2}{|\epsilon|} & \left[2F \cos 3k_y/2 \left(\sqrt{3}/8 \sin \sqrt{3}k_x/2 (k_x \sin 2\phi + 3k_y \cos 2\phi) - 1/4 \cos \sqrt{3}k_x/2 \sin 2\phi \right. \right. \\
 & \left. \left. + \sqrt{3}k_x/2 \sin \sqrt{3}k_x/2 \sin 2\phi \right) \right. \\
 & + 2 \sin 3k_y/2 \left(-\sqrt{3}/2 \sin \sqrt{3}k_x/2 - F(\sqrt{3}/8 \cos \sqrt{3}k_x/2 (\sqrt{3}k_y \sin 2\phi + k_x \cos 2\phi) \right. \\
 & \left. \left. + 1/4 \sin \sqrt{3}k_x/2 \cos 2\phi + \cos \sqrt{3}k_x/2 \sin 2\phi \right) \right. \\
 & \left. + F \left(\sqrt{3}/2 \sin \sqrt{3}k_x (k_x \sin 2\phi + 3k_y \cos 2\phi) - 1/4 \cos \sqrt{3}k_x/2 \sin 2\phi \right) \right] \quad (3.14)
 \end{aligned}$$

And

$$\begin{aligned}
 J_y = \frac{-2}{|\epsilon|} & \left[1 + \cos 3k_y/2 \left(\cos \sqrt{3}k_x/2 - F/4 \sin \sqrt{3}k_x/2 (\sqrt{3}k_y \sin 2\phi \right. \right. \\
 & \left. \left. + k_x \cos 2\phi) + 3F/2 \cos \sqrt{3}k_x/2 \cos 2\phi \right) \right. \\
 & + F \sin 3k_y/2 \left(k_x \sin 2\phi \cos \sqrt{3}k_x/2 + 1/4 \cos \sqrt{3}k_x/2 (\sqrt{3}k_y \sin 2\phi + k_x \cos 2\phi) \right. \\
 & \left. \left. + 3/2 \cos \sqrt{3}k_x/2 \cos 2\phi \right) \right. \\
 & - 2 \cos \sqrt{3}k_x/2 \left(\cos \sqrt{3}k_x/2 - F/2 \sin \sqrt{3}k_x/2 (\sqrt{3}k_y \sin 2\phi + k_x \cos 2\phi) \right. \\
 & \left. \left. + 3F/2 \cos \sqrt{3}k_x/2 \cos 2\phi \right) \right] \quad (3.15)
 \end{aligned}$$

Which allows us to calculate the optical conductivity numerically. The optical conductivity is given by Kubo's formula (30)

$$\sigma_{\mu,\nu}(\omega) = \frac{1}{\omega} \int_0^\infty dt e^{i\omega t} \langle [J_\mu(t), J_\nu(0)] \rangle. \quad (3.16)$$

The components of the current operator can be calculated from $J_{\nu,\mu}(t) = e^{iHt} J_{\nu,\mu}(0) e^{-iHt}$, where $J_{\nu,\mu}(0) = \Psi^\dagger(\mathbf{r}) \hat{v}_{\nu,\mu} \Psi(\mathbf{r}')$, in which $\nu, \mu = x, y$. The lon-

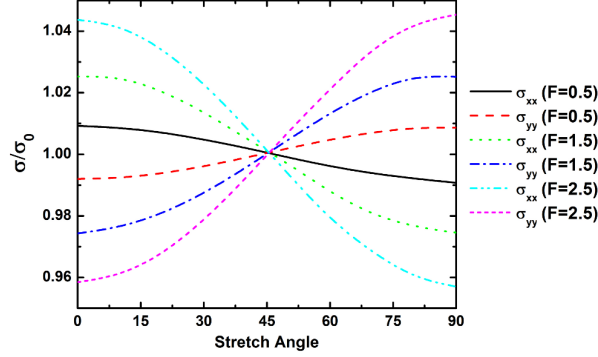


Figure 3.9: The stretching induced anisotropy in the longitudinal conductivity for three small pseudo force values. These correspond to bond stretching angles of $\approx 0.4, 1.2, 2$ degrees for $F = 0.5, 1.5, 2.5$ respectively. Despite the relatively small stretching angle, the induced anisotropy is as much as 10%. The angular dependence of this quantity is quite well behaved. When stretching along the zig-zag direction, the zig-zag longitudinal conductivity is increased, and similarly for stretching along the armchair direction. For stretching of $\pi/4$, the system remains isotropic.

gitudinal ($\sigma_{\nu\nu}$, $\nu = x, y$) and Hall (σ_{xy}) optical conductivities are calculated numerically.

In Fig.3.9 we show the longitudinal conductivity along the x (zig-zag) and y (armchair) directions for various pseudo-force values. These values are for the ‘universal’ conductivity, where we have chosen $\hbar\omega = 0.05eV$. These values are approximately universal up to $\hbar\omega = 1eV$. Beyond this regime the effect of stretching is negligible, and the optical conductivity agrees with other calculations for intrinsic graphene (20; 21). Within the Dirac regime however, we can see that a significant anisotropy develops, which is greatest when the sample is stretched along either the armchair or zig-zag directions. When stretched along the zig-zag direction ($\phi = 0$), the optical conductivity along the zig-zag direction becomes higher, and the conductivity along the armchair direction becomes smaller. This discrepancy is as much as $\approx 10\%$ for $F = 2.5$, which corresponds to bond bending angles of $\theta_2 = -\theta_1 \approx 2.16^\circ$. This is a large degree of anisotropy for such a small angle. As the stretching angle changes, we see that at 45° of rotation, the regular isotropic universal conductivity is regained. This is not wholly unexpected, but

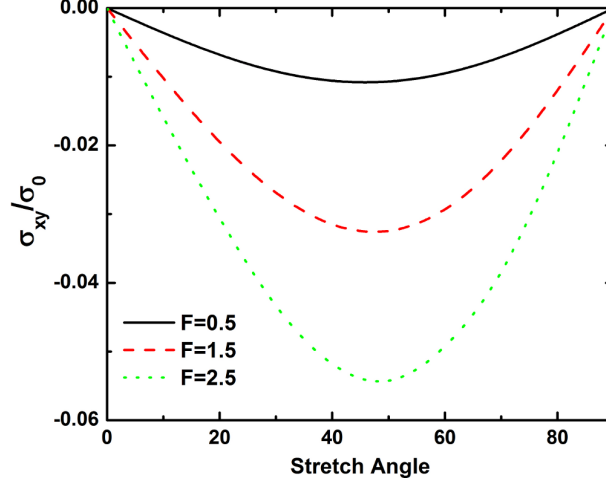


Figure 3.10: The transverse optical conductivity as a function of stretching angle. Interestingly, even though the C3 symmetry is broken for stretching along the high symmetry directions, the transverse conductivity remains zero. For chiral stretching this is not the case. Maximum stretching is reached for the longitudinally isotropic value of $\phi = \pi/4$.

is interesting considering the distortions that graphene obtains on this angle of stretching (see Fig.1(c)). As we continue to rotate the angle of stretching, we see that at $\phi = 90^\circ$, the reverse situation is obtained as that seen for $\phi = 0$.

The Hall conductivity for single layer graphene is zero due to the C3 symmetry of the system. In Fig.3.10 we report the variation of the Hall conductivity within the Dirac regime as a function of ϕ . We can see that for chiral angles, the Hall conductivity is non-zero, reaching a maximum of $\approx \sigma_0/20$ at $\phi = 45^\circ$ and $F = 2.5$. Despite the broken C3 symmetry, when stretching along the zig-zag or armchair directions, the Hall conductivity still gives zero. The magnitude of the Hall conductivity increases linearly with F for small magnitudes of F .

Finally, in Fig.3.11 we show the Hall conductivity at $\phi = 45^\circ$ over the entire energy spectrum. For transitions between the two high density of states saddle points at $\Omega = 2$, both the longitudinal and Hall conductivity reach a maximum. The Hall conductivity has changed sign near this point and remains positive for the rest of the energy spectrum. For bond bending of $\approx 2^\circ$, the Hall conductivity reaches a maximum value of $\sigma_{xy}^{\text{peak}} \approx 0.85\sigma_0$. The longitudinal conductivity at this same point is almost identical to the unstretched value, which has been reported

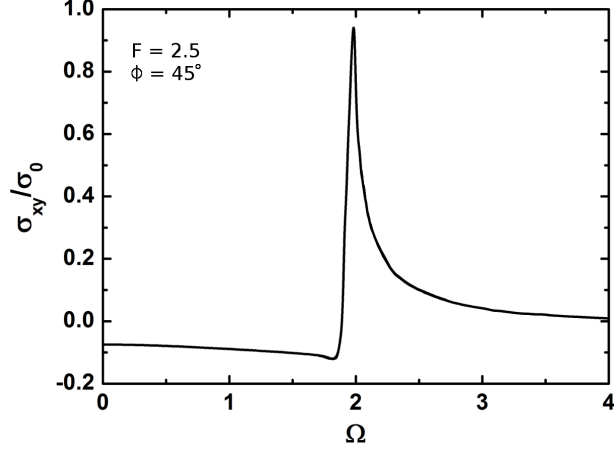


Figure 3.11: The transverse (Hall) conductivity for $\phi = 45^\circ$ and $F = 2.5$. The transverse conductivity reaches a maximum of $\approx 0.85\sigma_0$ at the high density of states saddle point $\Omega = 2$.

elsewhere and reaches a maximum of $\sigma_{xx(yy)}^{\text{peak}} \approx 6 - 8\sigma_0$. Although approximately an order of magnitude smaller, the transverse conductivity is not insignificant.

In conclusion, we have calculated the optical conductivity of stretched graphene. We have observed suprisingly large anisotropy in the universal longitudinal conductivity of stretched graphene for small stretching amounts ($\approx 10\%$ anisotropy for bond bending of $\approx 2.16^\circ$). We also have observed that when stretched along chiral directions, the Hall conductivity is non-zero, and reaches a maximum value when stretching at an angle of 45° from either the zig-zag or armchair direction. Along these two high symmetry directions however, the Hall conductivity was still zero as intrinsic graphene. We have also calculated the Hall conductivity across the entire energy spectrum and found that near the high density of states saddle points, the Hall conductivity changes sign and exhibits a strong peak (which is a maximum when $\phi = 45^\circ$), for relatively small stretching magnitudes.

3.6 Conclusions

The optical properties of graphene based materials have, in this chapter, been shown to be quite diverse, robust, and highly tunable. The universal conductivity of graphene is a remarkable result in its own right, but for practical purposes is impractically small.

Here we have shown that this response can be increased by an order of magnitude at characteristic frequencies in bilayer graphene which happen to fall within the THz-FIR regime. When cutting graphene into ribbons, the optical response is not significantly enhanced. However we have also shown in this chapter that in the case of bilayer ribbons this is no longer true. We have demonstrated that a two order of magnitude increase in the optical conductivity of bilayer graphene nanoribbons can be achieved. These results eliminate the conditions that formerly made graphene unsuitable for photonic device applications, and in particular will be useful for potential THz-FIR emitters and detectors.

Furthermore, we have demonstrated that mechanical stretching can break the C_3 symmetry of single layer graphene, which in turn leads to a significant anisotropy in the longitudinal optical conductivity of this material at modest stretching angles, as well as quite a strong Hall conductivity to emerge. These results will be useful, particularly the strong Hall response, for potential future applications.

Having exhausted the linear response theory in the absence of interactions, we now proceed to calculate, in the next chapter, the optical conductivity of graphene nanoribbons within a magnetic field, then in chapter 5, the nonlinear optical conductivity of single layer Dirac graphene, and, in chapter 6, the linear response theory in the presence of electron-LO phonon interactions.

Chapter 4

Nonlinear Optical Conductivity of Graphene

In the last chapter we discussed the optical conductance of a variety of graphene based systems. So far we have only calculated the linear approximation to the optical conductivity of these systems. Before the advent of strong light sources such as the laser, this was a reasonable approximation. This is no longer universally the case. In this chapter we will demonstrate that strong nonlinear effects can exist in intrinsic ($\mu = 0$) graphene in the terahertz to infrared frequency regime under a moderate electric field intensity. Within the classical picture, it has been shown elsewhere that frequency up-conversion can be achieved within the Dirac description(22), although the field response has been restricted to the linear E term. Here we shall adopt an approach that treats the coupling of the Dirac electron to the time-dependent electric field quantum mechanically to calculate the nonlinear terms, both in high order electrical field and in multiple frequencies. We determine the required field strength to induce non-negligible nonlinear effects, and investigate the temperature dependence of these terms as well.

4.1 Formalism

Let's consider intrinsic graphene under an applied field, $E(t) = Ee^{i\omega t}$ whose direction is along the x-axis. The tight binding Hamiltonian in the low energy

regime is given by,

$$H = v_F \begin{pmatrix} 0 & p_- + eA_- \\ p_+ + eA_+ & 0 \end{pmatrix} \quad (4.1)$$

Where $v_F \approx c/300$, $p_{\pm} = p_x \pm ip_y$, and $A_{\pm} = A = \frac{E}{i\omega} e^{i\omega t}$. We can use this form of the electric field rather than the real part because the imaginary component adds a correction to the wavefunction which is two orders smaller than the real part (ie two expansion terms along), and so is deemed irrelevant. This form is much more readily used, and so is chosen to be a more suitable choice. The time-dependent two-component wavefunctions can be expanded in the basis set

$$\psi(\mathbf{p}, t) = \sum_{n=0}^{\infty} \phi(\mathbf{p}, n) e^{in\omega t} e^{-i\epsilon t}, \quad (4.2)$$

where $\epsilon = |\mathbf{p}|$, and $\phi(\mathbf{p}, n)$ is a spinor given by

$$\phi(\mathbf{p}, n) = \begin{pmatrix} \alpha_n(\mathbf{p}) \\ \beta_n(\mathbf{p}) \end{pmatrix}. \quad (4.3)$$

By substituting eq.(2) into the Schrödinger equation $i\hbar\partial\psi/\partial t = H\psi$, we obtain

$$\begin{aligned} & -\hbar \sum_{n=0}^{\infty} \phi(\mathbf{p}, n) (n\omega - \epsilon) e^{i(n\omega - \epsilon)t} \\ & = \begin{pmatrix} 0 & p_- + \frac{eE}{i\omega} e^{i\omega t} \\ p_+ + \frac{eE}{i\omega} e^{i\omega t} & 0 \end{pmatrix} \sum_{n=0}^{\infty} \phi(\mathbf{p}, n) e^{i(n\omega - \epsilon)t}. \end{aligned} \quad (4.4)$$

The above equation contains information of all multiple photon process in intrinsic graphene. Due to the orthonormal relation of $e^{in\omega t}$, we can write the coupled recursion relations for the spinor components,

$$\begin{aligned} (\epsilon - n\omega)\alpha_n(\mathbf{p}) &= p_+\beta_n(\mathbf{p}) + \frac{E}{2i\omega}\beta_{n-1}(\mathbf{p}) \\ (\epsilon - n\omega)\beta_n(\mathbf{p}) &= p_-\alpha_n(\mathbf{p}) + \frac{E}{2i\omega}\alpha_{n-1}(\mathbf{p}) \end{aligned} \quad (4.5)$$

The recursion relation couples the n photon processes to the $n - 1$ photon processes. From the solutions to equation (5) we can calculate the n th order total current which is given by

$$\mathbf{J}_n^\nu = \frac{1}{4\pi^2} \int d\mathbf{p} \mathbf{j}_n^\nu N(\epsilon). \quad (4.6)$$

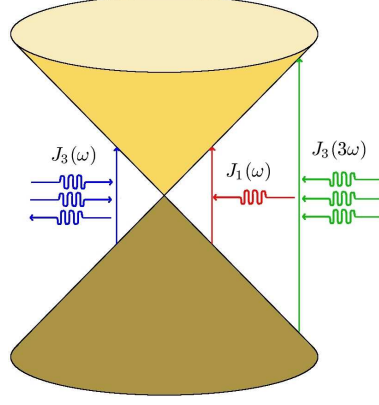


Figure 4.1: A schematic illustration of linear and nonlinear optical processes in intrinsic graphene. The universal conductance described by \mathbf{J}_1 . The two third order terms $\mathbf{J}_3(\omega)$ and $\mathbf{J}_3(3\omega)$ are shown in blue and green colour. The latter is a frequency tripling term which is the dominant nonlinear current.

Here $N(\epsilon) = n_F(-\epsilon) - n_F(\epsilon) = \tanh(\epsilon/2k_B T)$, and $\mathbf{j}_n^\nu = \psi^\dagger \hat{v}_\nu \psi$, where $\hat{v}_\nu = \frac{\partial H}{\partial p_\nu}$ is the current operator with $\nu = x, y$. The choice of ν is arbitrary due to the simplicity of the Hamiltonian. The n th order current becomes

$$\mathbf{J}_n = \frac{1}{2\pi^2} \int N(\epsilon) p dp d\theta \text{Re} \left(\sum_{i=0}^n \alpha_i^* \beta_{n-i} + \beta_i^* \alpha_{n-i} \right) \quad (4.7)$$

In the absence of the electric field, only $n = 0$ terms are nonzero and the solution of eq.(5) is the usual wavefunctions for the massless Dirac Fermion, $\alpha_0(\mathbf{p}) = 1/\sqrt{2}$, $\beta_0(\mathbf{p}) = p_-/\sqrt{2}p$.

All that remains then, is to calculate α_i and β_i to our desired order. We are interested in the third order current, so we need to calculate all terms up to $i = 3$.

4.2 Results

We explicitly write out the recursion relations stated earlier:

$$\begin{aligned} \alpha_n &= \frac{1}{p - n\omega} \left(p_+ \beta_n + A \beta_{n-1} \right) \\ \beta_n &= \frac{1}{p - n\omega} \left(p_- \alpha_n + A \alpha_{n-1} \right) \end{aligned} \quad (4.8)$$

We can form a useful relation for α_n which will help us apply the recursion relations above:

$$\begin{aligned}
 \alpha_n &= \frac{1}{p - n\omega} \left(p_+ \beta_n + A \beta_{n-1} \right) \\
 &= \frac{1}{p - n\omega} \left(\frac{p_+}{p - n\omega} (p_- \alpha_n + A \alpha_{n-1}) + A \beta_{n-1} \right) \\
 &= \frac{1/(p - n\omega)}{1 - p^2/(p - n\omega)^2} \left(\frac{A p_+}{p - n\omega} \alpha_{n-1} + A \beta_{n-1} \right) \\
 &= \frac{A}{n\omega(n\omega - 2p)} \left(p_+ \alpha_{n-1} + (p - n\omega) \beta_{n-1} \right)
 \end{aligned} \tag{4.9}$$

Now, noting that $\alpha_0 = \frac{1}{\sqrt{2}}$, and $\beta_0 = \frac{p_-}{\sqrt{2}p}$, we can calculate subsequent values:

$$\begin{aligned}
 \alpha_1 &= \frac{A}{\omega(\omega - 2p)} \left(p_+ \alpha_0 + (p - \omega) \beta_0 \right) \\
 &= \frac{A}{\omega(\omega - 2p)} \left(\frac{p_+}{\sqrt{2}} + (p - \omega) \frac{p_-}{\sqrt{2}p} \right) \\
 &= \frac{A}{\sqrt{2}\omega p(\omega - 2p)} \left(p_+ p + (p - \omega) p_- \right) \\
 &= \frac{A}{\sqrt{2}\omega p(\omega - 2p)} \left((p_- + p_+) p - \omega p_- \right)
 \end{aligned} \tag{4.10}$$

Solving for β_1 then, we have

$$\begin{aligned}
 \beta_1 &= \frac{1}{p - \omega} \left(p_- \alpha_1 + A \alpha_0 \right) \\
 &= \frac{1}{p - \omega} \left(p_- \left(\frac{A}{\sqrt{2}\omega p(\omega - 2p)} \left((p_- + p_+) p - \omega p_- \right) \right) + A \alpha_0 \right) \\
 &= \frac{A}{\sqrt{2}(p - \omega)\omega p(\omega - 2p)} \left(p_- \left((p_- + p_+) p - \omega p_- \right) + \omega p(\omega - 2p) \right) \\
 &= \frac{A}{\sqrt{2}(p - \omega)\omega p(\omega - 2p)} \left(p_-^2 p + p^3 - \omega p_-^2 + \omega^2 p - 2\omega p^2 \right) \\
 &= \frac{A}{\sqrt{2}(p - \omega)\omega p(\omega - 2p)} \left(p(p^2 - 2\omega p + \omega^2) + p_-^2(p - \omega) \right) \\
 &= \frac{A}{\sqrt{2}\omega p(\omega - 2p)} (p^2 - \omega p + p_-^2)
 \end{aligned} \tag{4.11}$$

So we have

$$\begin{aligned}\alpha_1 &= C_1((p_- + p_+)p - \omega p_-) \\ \beta_1 &= C_1(p^2 - \omega p + p_-^2)\end{aligned}\tag{4.12}$$

Where $C_1 = \frac{A}{\sqrt{2\omega p(\omega - 2p)}}$. Now for the second order terms:

$$\begin{aligned}\alpha_2 &= \frac{A}{2\omega(2\omega - 2p)} \left(p_+ \alpha_1 + (p - 2\omega) \beta_1 \right) \\ &= \frac{AC_1}{4\omega(\omega - p)} \left(p_+((p_- + p_+)p - \omega p_-) + (p - 2\omega)(p^2 - \omega p + p_-^2) \right) \\ &= \frac{AC_1}{4\omega(\omega - p)} \left(2p^3 + pp_+^2 - 4\omega p^2 + 2\omega^2 p + p_-^2 p - 2\omega p_-^2 \right) \\ &= \frac{AC_1}{4\omega(\omega - p)} \left(2(p - \omega)(p^2 - p\omega + p_-^2) + p(p_+^2 - p_-^2) \right) \\ &= \frac{A}{4\omega(\omega - p)} \left(2(p - \omega) \beta_1 + p(p_+^2 - p_-^2) C_1 \right)\end{aligned}\tag{4.13}$$

So

$$\begin{aligned}\beta_2 &= \frac{p_- \alpha_2 + 4A\alpha_1\omega(\omega - p)}{4\omega(\omega - p)(p - 2\omega)} \\ &= \frac{AC_1(2p_-(p^3 - 4p^2\omega + 5p\omega^2 - 2\omega^3) + p_+(p^3 - 4\omega p^2 + 4\omega^2 p) + p_-^3(p - 2\omega))}{4\omega(\omega - p)(p - 2\omega)} \\ &= \frac{AC_1(2p_-(p^3 - 4p^2\omega + 5p\omega^2 - 2\omega^3) + p_+p(p - 2\omega)^2 + p_-^3(p - 2\omega))}{4\omega(\omega - p)(p - 2\omega)}\end{aligned}\tag{4.14}$$

It seems a fair choice to think that the 3rd order polynomial will divide by $p - 2\omega$, which it turns out it does. So we have

$$\begin{aligned}\beta_2 &= \frac{AC_1(2p_-(p - 2\omega)(p - \omega)^2 + p_+p(p - 2\omega)^2 + p_-^3(p - 2\omega))}{4\omega(\omega - p)(p - 2\omega)} \\ &= \frac{AC_1(2p_-(p - \omega)^2 + p_+p(p - 2\omega) + p_-^3)}{4\omega(\omega - p)}\end{aligned}\tag{4.15}$$

And finally, for the third order terms:

$$\begin{aligned}\alpha_3 &= \frac{A}{3\omega(3\omega - 2p)} \left(p_+ \alpha_2 + (p - 3\omega) \beta_2 \right) \\ &= \frac{A^2 C_1 (p_+ (3p^3 - 9p^2\omega + 8p\omega^2) + p_- (3p^3 - 12p^2\omega + 14p\omega^2 - 6\omega^3) + p_-^3 (p - 3\omega) + p_+^3 p)}{12\omega^2(3\omega - 2p)(\omega - p)}\end{aligned}\quad (4.16)$$

And finally

$$\begin{aligned}\beta_3 &= \frac{1}{p - 3\omega} (p_- \alpha_3 + A \alpha_2) \\ &= \frac{A^2 C_1 (p_-^2 (3p^2 - 9\omega p + 8\omega^2) + p_+^2 p (p - 3\omega) + p_-^4 + p (3p^3 - 12p^2\omega + 14p\omega^2 - 6\omega^3))}{12\omega^2(3\omega - 2p)(\omega - p)}\end{aligned}\quad (4.17)$$

To calculate the current, consider the following terms:

$$\begin{aligned}\phi_i^* \hat{v} \phi_j + \phi_j^* \hat{v} \phi_i &= \alpha_i^* \beta_j + \beta_i^* \alpha_j + \alpha_j^* \beta_i + \beta_j^* \alpha_i \\ &= 2\text{Re}(\alpha_i^* \beta_j + \beta_i^* \alpha_j)\end{aligned}\quad (4.18)$$

To calculate the third order term then, we have

$$\begin{aligned}\mathbf{j}_3 &= \phi_0^* \hat{v} \phi_3 + \phi_0^* \hat{v} \phi_3 + \phi_1^* \hat{v} \phi_2 + \phi_2^* \hat{v} \phi_1 + \phi_3^* \hat{v} \phi_0 \\ &= 2\text{Re}(\alpha_0^* \beta_3 + \beta_0^* \alpha_3 + \alpha_1^* \beta_2 + \beta_1^* \alpha_2)\end{aligned}\quad (4.19)$$

And the current is given by

$$\begin{aligned}\mathbf{J}_3 &= \frac{1}{4\pi^2} \int d\mathbf{p} \mathbf{j}_3 \\ &= \frac{1}{2\pi^2} \int p dp d\theta \text{Re}(\alpha_0^* \beta_3 + \beta_0^* \alpha_3 + \alpha_1^* \beta_2 + \beta_1^* \alpha_2)\end{aligned}\quad (4.20)$$

First, we note that the integral over all p_{\pm}^{2n} terms give zero. The first and second terms only have a single contribution then which is immediately seen to be the term in β_3 which has no p_{\pm} prefactors, and the α_3 term with the p_- prefactor

which combines with β_0^* 's p_+ to give p^2 . All other terms cancel over angular integration. So we have

$$\int p dp d\theta \operatorname{Re}(\alpha_0^* \beta_3) = \int p dp \frac{A^3 p (3p^3 - 12p^2 \omega + 14p\omega^2 - 6\omega^3)}{12\omega^3 p (\omega - 2p)(\omega - p)(3\omega - 2p)} \quad (4.21)$$

Now for the third term:

$$\begin{aligned} \int p dp d\theta \operatorname{Re}(\alpha_1^* \beta_2) &= \int p dp \frac{2\pi C_1^* (p_+ (p - \omega) + p_- p) A C_1 (2p_- (p - \omega)^2 + p_+ p (p - 2\omega) + p_-^3)}{4\omega(\omega - p)} \\ &= \int p dp \frac{2\pi |A|^2 A (2p^2 (p - \omega)^3 + p^4 (p - 2\omega))}{8\omega^3 p^2 |\omega - 2p|^2 (\omega - p)} \\ &= \int p dp \frac{\pi |A|^2 A (2(p - \omega)^3 + p^2 (p - 2\omega))}{4\omega^3 |\omega - 2p|^2 (\omega - p)} \end{aligned} \quad (4.22)$$

And finally, the complement to this term:

$$\begin{aligned} \int p dp d\theta \operatorname{Re}(\beta_1^* \alpha_2) &= \int p dp \frac{2\pi C_1^* (p^2 - \omega p + p_+^2) A C_1 (2(p - \omega)(p^2 - \omega p + p_-^2) + p(p_+^2 - p_-^2))}{4\omega(\omega - p)} \\ &= \int p dp \frac{2\pi |A|^2 A (2(p - \omega)((p^2 - \omega p)^2 + p^4) - p^5)}{8\omega^3 p^2 |\omega - 2p|^2 (\omega - p)} \\ &= \int p dp \frac{\pi |A|^2 A (2(p - \omega)^3 - 2p^2 (p - \omega) - p^3)}{4\omega^3 |\omega - 2p|^2 (\omega - p)} \\ &= \int p dp \frac{\pi |A|^2 A (2(p - \omega)^3 - 3p^3 + 2p^2 \omega)}{4\omega^3 |\omega - 2p|^2 (\omega - p)} \end{aligned} \quad (4.23)$$

Summing these last two terms, we get

$$\int p dp d\theta \operatorname{Re}(\alpha_1^* \beta_2 + \beta_1^* \alpha_2) = \operatorname{Re} \left[\int p dp \frac{\pi |A|^2 A (4(p - \omega)^3 - 2p^3)}{4\omega^3 |\omega - 2p|^2 (\omega - p)} \right] \quad (4.24)$$

Now to sum over the meagnitude of the momentum, we take the analytic continuation of the denominators such that

$$\frac{1}{x} \rightarrow \frac{1}{x + i\eta} \rightarrow \frac{1}{x} + i\pi\delta(x) \quad (4.25)$$

Calculating our final result first, the absolute value denominator is a magnitude, so we don't analytically continue this term, leaving only the final term, giving

$$\int p dp d\theta \operatorname{Re}(\alpha_1^* \beta_2 + \beta_1^* \alpha_2) = \operatorname{Re} \left[\int p dp \frac{\pi |A|^2 A (4(p - \omega)^3 - 2p^3)}{4\omega^3 |\omega - 2p|^2} \left(\frac{1}{\omega - p} + i\pi \delta(\omega - p) \right) \right] \quad (4.26)$$

But A is imaginary, therefore we only want to take the imaginary part in order to retain only the real parts. Then we have

$$\begin{aligned} \int p dp d\theta \operatorname{Re}(\alpha_1^* \beta_2 + \beta_1^* \alpha_2) &= \left[\int p dp \frac{i\pi^2 |A|^2 A (4(p - \omega)^3 - 2p^3)}{4\omega^3 |\omega - 2p|^2} \delta(\omega - p) \right] \\ &= \frac{-2i\pi^2 |A|^2 A \omega^4}{4\omega^3 (-\omega)^2} \\ &= \frac{-i\pi^2 |A|^2 A}{2\omega} \end{aligned} \quad (4.27)$$

The first two terms aren't as simple. We wish to integrate

$$\begin{aligned} &\int dp \int d\theta \frac{A^3 p (3p^3 - 12p^2 \omega + 14p\omega^2 - 6\omega^3)}{12\omega^3 (\omega - 2p)(\omega - p)(3\omega - 2p)} \\ &= 2\pi \int dp \frac{A^3 p (3p^3 - 12p^2 \omega + 14p\omega^2 - 6\omega^3)}{12\omega^3} \\ &\times \left(\frac{1}{\omega - 2p} + i\pi \delta(\omega - 2p) \right) \left(\frac{1}{\omega - p} + i\pi \delta(\omega - p) \right) \left(\frac{1}{3\omega - 2p} + i\pi \delta(3\omega - 2p) \right) \\ &= 2\pi \int dp \frac{A^3 p (3p^3 - 12p^2 \omega + 14p\omega^2 - 6\omega^3)}{12\omega^3} \\ &\times i\pi \left(\frac{\delta(\omega - 2p)}{(\omega - p)(3\omega - 2p)} + \frac{\delta(\omega - p)}{(\omega - 2p)(3\omega - 2p)} + \frac{\delta(3\omega - 2p)}{(\omega - 2p)(\omega - p)} \right) \\ &= 2i\pi^2 \frac{(-13/16 + 2 - 45/16)\omega^2}{12\omega^3} = \frac{-2i\pi^2 7A^3}{32\omega} = \frac{2\pi^2 7|A|^3 e^{3i\omega t}}{32\omega} \end{aligned} \quad (4.28)$$

And our final result is (reintroducing $-e$ from the current formula)

$$\begin{aligned}\mathbf{J}_3 &= \frac{e|A|^3}{2\pi^2} \left[\frac{2\pi^2 7e^{3i\omega t}}{32\omega} + \frac{2\pi^2 e^{i\omega t}}{4\omega} \right] \\ &= \frac{e|A|^3}{4\omega} \left[\frac{7e^{3i\omega t}}{8} + 2e^{i\omega t} \right]\end{aligned}\tag{4.29}$$

Where σ_0 is the ‘universal conductivity’ of graphene. In real units, we simply set $|A| \rightarrow \frac{v_F e E_0}{\hbar \omega}$ (and $p \rightarrow v_F p$ but they have been eliminated with the delta functions) and we end up with

$$\mathbf{J}_3 = \frac{J_1 e^2 v_F^2 E_0^2}{\hbar^2 \omega^4} \left[\frac{7e^{3i\omega t}}{8} + e^{i\omega t} \right]\tag{4.30}$$

For a 1THz beam, for the third order term to be comparable to the first order term we have

$$\begin{aligned}\frac{\mathbf{J}_3}{\mathbf{J}_1} &= \frac{e^2 v_F^2 E_0^2}{\hbar^2 \omega^4} \left[\frac{7e^{3i\omega t}}{8} + e^{i\omega t} \right] \\ &\approx \frac{e^2 v_F^2 E_0^2}{\hbar^2 \omega^4} \\ &\rightarrow E_c = \frac{\hbar \omega^2}{e v_F}\end{aligned}\tag{4.31}$$

Where we have defined E_c as the critical field needed to make the nonlinear terms begin to dominate over the linear ones. Using $\hbar \approx 1E - 34Js$, $e \approx 1E - 19C$, $\omega^2 = 1E24 * 4\pi^2 s^{-2} \approx 1E25s^{-2}$, and $v_F \approx 1E6ms^{-1}$ we get

$$E_0 \approx 10000V/m\tag{4.32}$$

4.2.1 Temperature Dependence of Results

We need not redo the entire to obtain the equivalent finite temperature results. Firstly consider

$$\begin{aligned}
 n_F(\epsilon) - n_F(-\epsilon) &= \frac{1}{e^{-\epsilon/\tau} + 1} - \frac{1}{e^{\epsilon/\tau} + 1} \\
 &= \frac{1}{e^{-\epsilon/\tau} + 1} - \frac{e^{-\epsilon/\tau}}{e^{-\epsilon/\tau} + 1} \\
 &= \frac{1 - e^{-\epsilon/\tau}}{e^{-\epsilon/\tau} + 1} \\
 &= -\frac{n_F(\epsilon)}{n_B(-\epsilon)} \\
 &= n(\epsilon)
 \end{aligned} \tag{4.33}$$

Inserting the distribution function into the velocity operators, we have, from equation 17:

$$\int p dp d\theta \operatorname{Re}(\alpha_1^* \beta_2 + \beta_1^* \alpha_2) = \operatorname{Re} \left[\int p dp \frac{\pi |A|^2 A (4(p - \omega)^3 - 2p^3)}{4\omega^3 |\omega - 2p|^2 (\omega - p)} \right] \frac{1 - e^{-p/\tau}}{e^{-p/\tau} + 1} \tag{4.34}$$

Which follows the analysis quite simply, giving (equivalent to eqn. 20):

$$J_3^1 = \frac{-i\pi^2 |A|^2 A}{\omega} \left(\frac{1 - e^{-\omega/\tau}}{e^{-\omega/\tau} + 1} \right) \tag{4.35}$$

For the other terms we start from eqn. 21

$$\begin{aligned}
 & \int dp \int d\theta \frac{A^3 p(3p^3 - 12p^2\omega + 14p\omega^2 - 6\omega^3)}{12\omega^3(\omega - 2p)(\omega - p)(3\omega - 2p)} n(p) \\
 &= 2\pi \int dp \frac{A^3 p(3p^3 - 12p^2\omega + 14p\omega^2 - 6\omega^3)}{12\omega^3} n(p) \\
 &\times \left(\frac{1}{\omega - 2p} + i\pi\delta(\omega - 2p) \right) \left(\frac{1}{\omega - p} + i\pi\delta(\omega - p) \right) \left(\frac{1}{3\omega - 2p} + i\pi\delta(3\omega - 2p) \right) \\
 &= 2\pi \int dp \frac{A^3 p(3p^3 - 12p^2\omega + 14p\omega^2 - 6\omega^3)}{12\omega^3} n(p) \\
 &\times i\pi \left(\frac{\delta(\omega - 2p)}{(\omega - p)(3\omega - 2p)} + \frac{\delta(\omega - p)}{(\omega - 2p)(3\omega - 2p)} + \frac{\delta(3\omega - 2p)}{(\omega - 2p)(\omega - p)} \right) \\
 &= 2i\pi^2 \frac{(-13n(\omega/2)/16 + 2n(\omega) - 45n(3\omega/2)/16)\omega^2}{12\omega^3}
 \end{aligned} \tag{4.36}$$

And so we have

$$\begin{aligned}
 \mathbf{J}_3 &= \frac{e|A|^3}{4\omega} \left[\left(\frac{-13n(\omega/2)}{48} + \frac{n(\omega)}{3} - \frac{45n(3\omega/2)}{48} \right) e^{3i\omega t} - n(\omega)e^{i\omega t} \right] \\
 &= \frac{\mathbf{J}_1 e^2 v_F^2 E_0^3}{\hbar^2 \omega^4} \left[\left(\frac{-13n(\omega/2)}{48} + 2\frac{n(\omega)}{3} - \frac{45n(3\omega/2)}{48} \right) e^{3i\omega t} - n(\omega)e^{i\omega t} \right]
 \end{aligned} \tag{4.37}$$

And the critical field strength is given by

$$E_c = \frac{\hbar\omega^2}{ev_F N_F^i} \tag{4.38}$$

Where

$$N_F^1 = 2n(\omega) \tag{4.39}$$

And

$$N_F^3 = -\frac{13}{48}n(\omega/2) + \frac{2}{3}n(\omega) - \frac{45}{48}n(3\omega/2) \tag{4.40}$$

Where

$$n(x) = \frac{1 - e^{-x/\tau}}{1 + e^{-x/\tau}} \tag{4.41}$$

If E_c^0 is the field strength required at zero temperature, we have

$$\frac{E_c^T}{E_c^0} = \frac{1}{N_F^i} \quad (4.42)$$

Which gives the field strength required as a ratio of the zero temperature field's strength.

We have calculated the linear current term via this method and obtained the same result as that obtained with the Kubo formula. As well as the linear term, we have calculated the third order current contribution to the ‘universal’ conductivity, as well as the frequency tripling term. It was found that the second order contribution, due to time inversion symmetry, gave a zero contribution. The third order current, then, is a superposition of a term oscillating with frequency ω , $J_3(\omega)$, and a frequency tripling term, $J_3(3\omega)$. The electronic processes represented by these two terms are shown in Fig.4.1. The linear ‘universal conductivity’ is a single photon process where an electron absorbs a photon making causing a from the valence band to the conduction band. The two third order terms are both three-photon processes. The term oscillation with frequency ω corresponds to a process where two incoming photons are absorbed, followed by the immediate emission of a third photon. The frequency tripling term corresponds to simultaneous absorption of three photons and the total transition energy is $3\hbar\omega$. The latter two terms are inversely proportional to ω^4 , and proportional to E_0^2 which is the power of the field.

By using the same method we can obtain $\alpha_n(\mathbf{p})$ and $\beta_n(\mathbf{p})$ for any n , and thus the full nonlinear current of the system at arbitrary electric field can be obtained. In general the n th order term is proportional to E_0^{n-1}/ω^{2n} . This means that at sufficiently high field strength and low frequency, the nonlinear terms are relevant.

In Fig.4.2, we plot the frequency dependent nonlinear current relative to the linear current. Both nonlinear terms decrease rapidly with the frequency, and at low frequencies, are approximately an order of magnitude lower at room temperature than at zero temperature. For weak fields and high frequencies, the linear current dominates and the two nonlinear terms are approximately equal in magnitude.

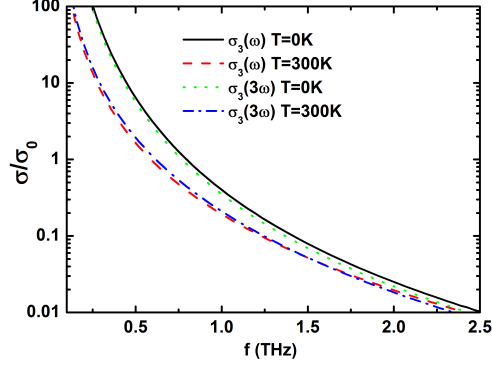


Figure 4.2: The frequency dependent nonlinear current. Both the single frequency and frequency tripling terms decrease as ω^{-4} , and also with increasing temperature. At low frequencies, low temperatures, and sufficiently high field strengths, the nonlinear terms will contribute to the optical conductance of graphene. In particular, the single frequency term will abolish the universality of the ‘universal conductance’ under the right conditions.

The point at which the nonlinear conductance dominates over the linear conductivity is given by the simple expression $\sigma_3^i/\sigma_1 > 1$ which gives a critical field strength of

$$E_C^{i\omega} = \frac{\hbar\omega^2}{ev_F\sqrt{N_i}} \quad (4.43)$$

For a beam of frequency $\omega=1\text{THz}$, at zero temperature, this gives a critical field strength of $E_C^\omega \approx 1600\text{V/cm}$ for the single frequency term, and $E_C^{3\omega} \approx 1700\text{V/cm}$ for the frequency tripling term. These field strengths can easily be achieved in a laboratory. For the same beam at room temperature, the critical field strength becomes $E_C^\omega \approx 2350\text{V/cm}$, and $E_C^{3\omega} \approx 2250\text{V/cm}$. This means there is a crossover point where the single frequency term ceases to dominate over the tripling term. At zero temperature, both critical fields increase as ω^2 . At room temperature, the two critical fields have rather different ω -dependence. Fig.4.3(a). shows the change of critical field $\Delta E_C = E_C(300\text{K}) - E_C(0\text{K})$ as a function of frequency. Both critical fields increase as temperature increases, indicating that thermal excitation can reduce the nonlinear effect. For each ΔE_C , there exists a frequency at which the thermal effect is strongest. For $\Delta E_C(\omega)$, this frequency is around

$k_B T/4$ and for $\Delta E_C(3\omega)$ it is around $3k_B T/4$.

Fig.4.3(b) shows the temperature dependence of the critical field at $\omega = 1\text{THz}$. There are two distinctive temperature regimes separated by the temperature T_1 . Below T_1 , $J_3(\omega)$ dominates the nonlinear effect while above T_1 , $J_3(3\omega)$ is more dominant. This behaviour is useful for frequency up-conversion device applications since the use of the frequency tripling term is more effective at room temperature than at low temperature.

These results demonstrate that graphene is a rather strong nonlinear material. There are two third order nonlinear terms, $J_3(\omega)$ and $J_3(3\omega)$. The first contributes to the current oscillating with ω . This adds a correction to the response function of ω , $\sigma(\omega) = \sigma_0 + E^2/\omega^4$. Therefore the universal conductance will be destroyed at a field strength of around 10^3 V/cm and frequency around 1THz. This effect is rather robust from low to room temperatures. The second nonlinear contribution is a frequency tripling term. This term is similar in strength to its complement, and at higher frequencies is higher than the single frequency term. This term's relative strength makes graphene a potential candidate as a THz emitter/detector at frequencies which are traditionally difficult to obtain by using an existing emitter at one third the frequency. For sufficiently strong fields the loss rate could be minimised even in a cascading situation.

These results are particularly significant as materials with a regular parabolic dispersion will not exhibit any kind of nonlinear response: linear response theory is exact in these cases. Nonlinearities are introduced to a parabolic system via disorder scattering. The slight distortion of the bandstructure can then cause non-zero higher order terms to arise. Graphene has no such restriction however due to its unique linear bandstructure.

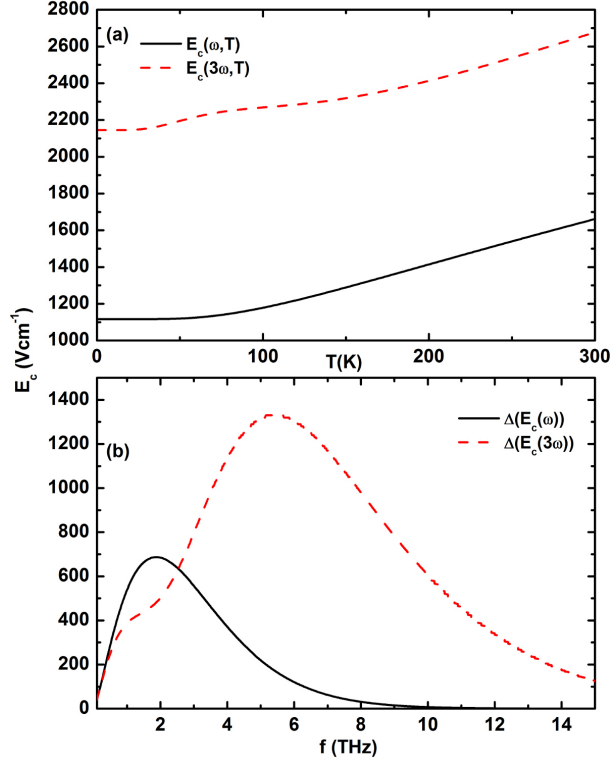


Figure 4.3: (a) The difference between the critical fields at 0K and 300K as a function of frequency (ie. $\Delta E_c = E_c(0K) - E_c(300K)$). There is a maximum discrepancy for each nonlinear contribution which indicates the frequency where thermal effects are most significant. (b) The temperature dependence of the critical field strength at fixed frequency. At low temperatures the single frequency nonlinear current dominates over the frequency tripling term. At $\approx 180K$ however, the situation is reversed such that at room temperature, the frequency tripling term is the dominant nonlinear contribution.

Chapter 5

High Frequency Conductivity of Graphene

With all the predictions of chapters three and four having emerged, the optical properties of graphene based systems appear to be more significant and more versatile than perhaps previously believed. However, a rather fundamental issue remains unsolved: What is the effect of electron-phonon coupling on these properties? Will the predicted properties remain at, say, room temperature?

With these questions in mind, we will now investigate the impact of electron-phonon coupling on the ac conductivity of graphene based systems. While these calculations are only strictly relevant for 2D single layer graphene, the results will inform our understanding of the contribution of electron-phonon interactions to the ac conductivity of graphene systems in general, and serve as a starting point for further theoretical and experimental investigation.

In this chapter we evaluate the finite temperature effect of the contribution to the optical conductivity obtained when electron-LO phonon interactions are included in the optical conductance calculation. The choice of which terms to include in the calculation will be determined diagrammatically with a simple high-frequency approximation. The electron-LO phonon interaction contribution to the universal conductivity of graphene that we obtain is relatively small, but becomes significant as temperature is sufficiently increased. Moreover, the nature of electron-LO phonon interactions in graphene is further understood by these results.

5.1 Phonon Spectrum

Before delving into the calculation of the optical conductivity of graphene with electron-phonon scattering included, we must determine the phonon spectrum of graphene. This has already been done quite competently (46). There are two methods which are primarily utilised. The first is the force constant tensor method up to fourth nearest neighbours. The second is a similar force constant tensor method up to only second nearest neighbours with a bond bending term incorporated to account for the effect of further neighbours.

We have used the former, and reproduced the phonon spectrum for the sake of future calculations. An excellent summary of the calculation is given in the book by Saito, Dresselhaus, and Dresselhaus (46), and is summarised briefly here.

The equation of motion for the i th atom in the unit cell is

$$M_i \mathbf{u}_i = \sum_j K^{ij} (\mathbf{u}_i - \mathbf{u}_j) \quad (5.1)$$

Where the summation is over all relevant neighbours j . The force constant tensor K^{ij} then, contains the strength and direction of the coupling between the neighbours i and j . Fourier transforming the displacements using the usual prescription we arrive at

$$\left(\sum_j K^{ij} - M_i \omega^2 \right) \sum_{\mathbf{k}} e^{-i\mathbf{k} \cdot \mathbf{R}_i} \mathbf{u}_{\mathbf{k}}^i = \sum_j K^{ij} \sum_{\mathbf{k}} e^{-i\mathbf{k} \cdot \mathbf{R}_j} \mathbf{u}_{\mathbf{k}}^j \quad (5.2)$$

Where ω is the eigenfrequency which we have reasonably assumed to be constant over all sites. The exponential terms can be combined on the RHS to give the position of the i th atom relative to the j th ($\Delta \mathbf{R}_{ij}$), and we obtain

$$\left(\sum_j K^{ij} - M_i \omega^2 \right) \sum_{\mathbf{k}} \mathbf{u}_{\mathbf{k}}^i = \sum_j K^{ij} \sum_{\mathbf{k}} e^{-i\mathbf{k} \cdot \Delta \mathbf{R}_{ij}} \mathbf{u}_{\mathbf{k}}^j \quad (5.3)$$

We are thus left with a dynamical matrix which is a function of the 3×3 force constant tensors. There are two atoms per unit cell in graphene, which means we have a 6×6 dynamical matrix, with quadrants

$$D = \begin{pmatrix} D_{AA} & D_{AB} \\ D_{BA} & D_{BB} \end{pmatrix}. \quad (5.4)$$

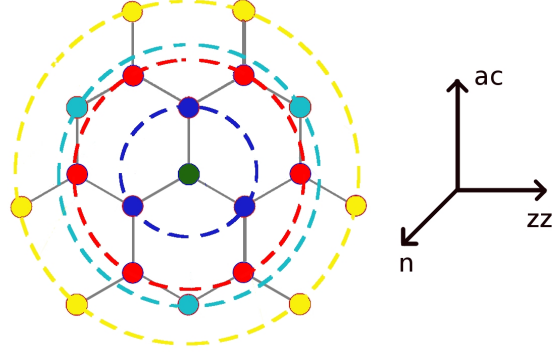


Figure 5.1: The fourth nearest neighbours for graphene. We include up to fourth nearest neighbours so that the bond-bending effect of the third and fourth neighbours will be included.

All that remains is to determine the force constant tensors for each pair, up to the desired number of nearest neighbours. In the literature cited, the three axes are denoted by radial (r), in-plane tangential (ti), and out-of-plane tangential (to). This is generally misleading for our present case because we won't be considering the case of carbon nanotubes. For this reason we shall depart from the cited text slightly and denote those three same directions by armchair (ac), zig-zag (zz), and normal (n). For coupling between an A atom and its neighbour along the ac axis, the force constant tensor is given by

$$K^{AB_1} = \begin{pmatrix} \phi_n^1 & 0 & 0 \\ 0 & \phi_{zz}^1 & 0 \\ 0 & 0 & \phi_{ac}^1 \end{pmatrix} \quad (5.5)$$

Where the superscript denotes that we are talking about first nearest neighbours. Whatever the values of ϕ^1 , the strengths will be equivalent for all equivalent neighbours, but rotated. So we obtain the other two first nearest neighbour force constant tensors by rotating the above matrix by $2\pi/3$ and $4\pi/3$ about the normal axis. We now have all the information we need except the actual values of ϕ . These are given in table 5.1.

There are three first nearest neighbours, six second nearest neighbours, three third nearest neighbours, and six fourth nearest neighbours, as shown in figure 5.1. The dispersion curves have been solved numerically and the results are shown

Table 5.1: Force constant tensor values ϕ up to fourth NN

Neighbour	Normal	Zig-Zag	Armchair
1	9.82	24.50	36.50
2	-0.40	-3.23	8.80
3	0.15	-5.25	3.00
4	-0.58	2.29	-1.92

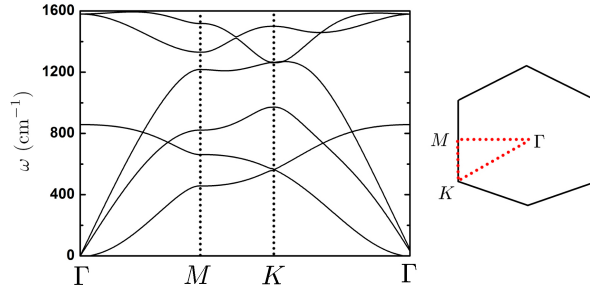


Figure 5.2: The phonon spectrum of graphene obtained using the fourth nearest neighbour force constant tensor method.

below in figure 5.2.

For results in this thesis we will only be concerned with the longitudinal optical mode at small \mathbf{q} (ie. near the Γ point), which is one of the two highest energy modes in figure 5.2, and has an energy in electron-volts of $\hbar\omega_{LO} \approx 0.2meV$.

5.2 Many Particle Formalism

Let's now consider electrons in graphene whose energy is relatively low and is given by the massless Dirac fermion dispersion. The Hamiltonian of electrons is given by

$$H = H_0 + H_I, \quad (5.6)$$

where H_0 is the Hamiltonian of noninteracting electrons and phonons,

$$H_0 = -t \sum_{\mathbf{k},s} k_s c_{\mathbf{k},s}^\dagger c_{\mathbf{k},-s} + \sum_{\mathbf{q}} \omega_{\mathbf{q}} b_{\mathbf{q}}^\dagger b_{\mathbf{q}}. \quad (5.7)$$

Here $t \approx 2.7\text{eV}$ is the first nearest neighbor hopping amplitude, $s = \pm 1$, and $k_{\pm} = k_x \pm ik_y$, and $c_{\mathbf{k}}(b_{\mathbf{k}})$ is the electron (phonon) annihilation operator whose hermitian conjugate is a creation operator, and ω_q is the LO phonon frequency. H_I is the electron-LO-phonon interaction term,

$$H_I = \sum_{\mathbf{k}, \mathbf{q}, s, s'} g_{\mathbf{k}, \mathbf{q}} M_q c_{\mathbf{k}+\mathbf{q}, s}^{\dagger} c_{\mathbf{k}, s'} (b_{\mathbf{q}} + b_{-\mathbf{q}}^{\dagger}), \quad (5.8)$$

where $g_{\mathbf{k}, \mathbf{q}}$ is the electron transition matrix element, M_q is the electron phonon coupling strength which, in the case of LO phonons, has no \mathbf{q} dependence but is given by a constant. We shall neglect the spin degree of freedom in our calculation.

The single particle eigenvalues and eigenvectors can be written as,

$$\epsilon_{\mathbf{k}, s} = s v_F |\mathbf{k}| \quad (5.9)$$

and

$$\psi_s(\mathbf{k}) = \frac{1}{\sqrt{2}} \begin{pmatrix} s e^{i\phi(\mathbf{k})} \\ 1 \end{pmatrix}, \quad (5.10)$$

where $\phi(\mathbf{k}) = \tan^{-1}(k_y/k_x)$. The corresponding Fermion field operators have the form $\Psi_s(\mathbf{r}) = \sum_{\mathbf{k}} \psi_s(\mathbf{k}) e^{i\mathbf{k} \cdot \mathbf{r}} c_{\mathbf{k}, s}$, from which the current operator is given as $j_{\nu} = e^2 \sum_{s, s', \mathbf{k}, \mathbf{k}'} \langle \mathbf{k}', s' | \partial H_0 / \partial k_{\nu} | \mathbf{k}, s \rangle$.

The Kubo formula for electrical conductivity is given by (30),

$$\sigma_{\mu, \nu}(\mathbf{q}, \omega) = \frac{1}{\omega} \int_0^{\infty} dt e^{i\omega t} \langle [j_{\mu}^{\dagger}(\mathbf{q}, t), j_{\nu}(\mathbf{q}, 0)] \rangle. \quad (5.11)$$

The time dependence of an operator is given by $O(t) = e^{iH_0 t} O e^{-iH_0 t}$. In order to represent the Kubo formula in terms of Green's functions, we need to find the ensemble average with the complete ground state. Of course this is not possible, and the usual approach is to exploit the existence of a Dyson's equation for the correlation function of equation 5.11, which is done by performing the S-matrix expansion of the perturbed state functions in terms of the known ground state functions of the non-interacting Hamiltonian H_0 . This leads to a Green's function representation of equation 5.11 of

$$\begin{aligned} M_{\mu\nu}(\mathbf{p}, u) = & \frac{1}{V} \sum_{s_1, s_2, s_3, s_4} \sum_{\mathbf{k}, \mathbf{k}'} v_{s_1, s_2}^*(\mathbf{k}') v_{s_3, s_4}(\mathbf{k}) \\ & \times \langle T(c_{\mathbf{p}+\mathbf{k}, s_1}^{\dagger} c_{\mathbf{p}, s_2} c_{\mathbf{p}+\mathbf{k}', s_3}^{\dagger} c_{\mathbf{p}, s_4} U(\beta)) \rangle_0 \end{aligned} \quad (5.12)$$

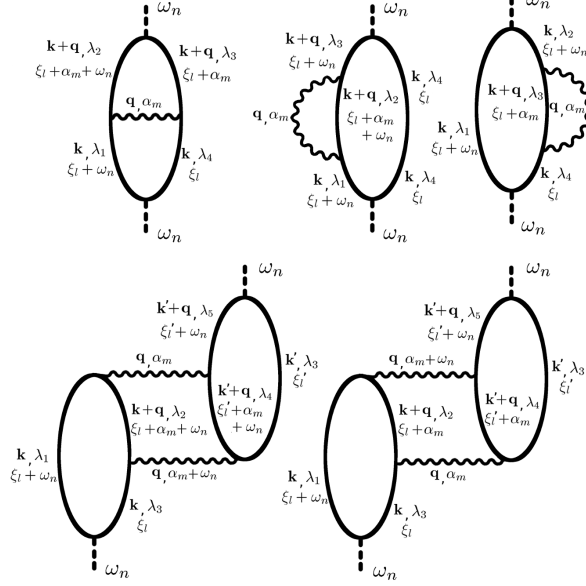


Figure 5.3: The five diagrams which contribute to the high frequency correction to the optical conductivity.

where $v_{i,j}(\mathbf{k}) = \langle \mathbf{k}, i | \partial H_0 / \partial k | \mathbf{k}, j \rangle$, and T is the time ordering operator. $U(\beta)$ carries the interaction terms and is given by

$$U(\beta) = \exp \left[- \int_0^\beta du H_I(u) \right] \quad (5.13)$$

Our system is isotropic, and so we will drop the indices μ, ν , and expect the Hall contribution to be zero. The Green's function described above will give us the phonon contribution to the longitudinal conductivity of graphene within the Dirac regime and under the high frequency approximation. Using this we can write out the Green's function $M(\mathbf{p}, u)$ to any order of interaction. We restrict our attention to terms with equal numbers of bubbles and interaction lines which is the five diagrams given in figure 5.3. The interactions are given by the RPA series (which simply retains the same approximation used to obtain the five diagrams) and is shown in figure 5.4. The effective interaction obtained via

$$D(\mathbf{q}, \alpha_m) = D^0(\mathbf{q}, \alpha_m) + \text{loop diagram}$$

Figure 5.4: The effective interaction is given by the bare phonon propagator plus an intermediate electron-phonon interaction, which causes a density fluctuation described by the electron propagator loop, followed by an effective interaction. This diagram describes the infinite sum implied by equations 5.14 & 5.16. Taking the effective interaction to be of this form is equivalent to adopting the RPA approximation.

the RPA approximation is

$$\begin{aligned} V(\mathbf{q}, \alpha_m) &= V^0(\mathbf{q}, \alpha_m) + V^0(\mathbf{q}, \alpha_m) \Pi(\mathbf{q}, \alpha_m) V(\mathbf{q}, \alpha_m) \\ &= \frac{V^0(\mathbf{q}, \alpha_m)}{1 - V^0(\mathbf{q}, \alpha_m) \Pi(\mathbf{q}, \alpha_m)}. \end{aligned} \quad (5.14)$$

Here $\Pi(\mathbf{q}, \alpha_m)$ is the electronic polarizability given by,

$$\Pi(\mathbf{q}, \alpha_m) = \sum_{\mathbf{k}, s, s'} \frac{|\langle \mathbf{k} + \mathbf{q}, s' | \mathbf{k}, s \rangle|^2 (n_F(\epsilon_{\mathbf{k}+\mathbf{q}, s'}) - n_F(\epsilon_{\mathbf{k}, s}))}{\epsilon_{\mathbf{k}+\mathbf{q}, s'} - \epsilon_{\mathbf{k}, s} - \alpha_m} \quad (5.15)$$

In eq.(5.14) $V^0 = M^2 D^0(\mathbf{q}, \alpha_m)$, where D^0 is the bare phonon propagator given by $D^0(\mathbf{q}, \alpha_m) = \frac{2\omega_{LO}}{\alpha_m^2 - \omega_{LO}^2}$ for the LO branch. The effective interaction from eq.(5.14) can then be written as,

$$V(\mathbf{q}, \alpha_m) = \frac{2\omega_{LO}}{\alpha_m^2 - \omega_{LO}^2 - 2\omega_{LO}\Pi(\mathbf{q}, \alpha_m)} \quad (5.16)$$

Using the five diagrams from figure 5.3, we obtain five separate Green's func-

tions:

$$\begin{aligned}
 & \sum_{l,m} V_{s_1,s_2,s_3,s_4}(\mathbf{q}, \alpha_m) G_{\mathbf{k},\lambda_1}(\xi_l + \omega_n) G_{\mathbf{k}+\mathbf{q},\lambda_2}(\xi_l + \alpha_m + \omega_n) \\
 & \quad \times G_{\mathbf{k}+\mathbf{q},\lambda_3}(\xi_l + \alpha_m) G_{\mathbf{k},\lambda_4}(\xi_l) F_{\lambda_1\lambda_2}(\mathbf{q}) F_{\lambda_4\lambda_3}^*(\mathbf{q}) v_{\lambda_2\lambda_3}^q v_{\lambda_4\lambda_1} \\
 & \sum_{l,m} V_{s_1,s_2,s_2,s_3}(\mathbf{q}, \alpha_m) G_{\mathbf{k},\lambda_1}(\xi_l + \omega_n) G_{\mathbf{k}+\mathbf{q},\lambda_2}(\xi_l + \alpha_m + \omega_n) \\
 & \quad \times G_{\mathbf{k},\lambda_3}(\xi_l + \omega_n) G_{\mathbf{k},\lambda_4}(\xi_l) F_{\lambda_2\lambda_1}(\mathbf{q}) F_{\lambda_2\lambda_3}^*(\mathbf{q}) v_{\lambda_3\lambda_4} v_{\lambda_4\lambda_1} \\
 & \sum_{l,m} V_{s_2,s_3,s_3,s_4}(\mathbf{q}, \alpha_m) G_{\mathbf{k},\lambda_1}(\xi_l + \omega_n) G_{\mathbf{k}+\mathbf{q},\lambda_2}(\xi_l) \\
 & \quad \times G_{\mathbf{k},\lambda_3}(\xi_l + \alpha_m) G_{\mathbf{k},\lambda_4}(\xi_l) F_{\lambda_3\lambda_2}(\mathbf{q}) F_{\lambda_3\lambda_4}^*(\mathbf{q}) v_{\lambda_1\lambda_2} v_{\lambda_4\lambda_1} \\
 & \sum_{l,l',m} V_{s_1,s_2,s_6,s_5}(\mathbf{q}, \alpha_m + \omega_n) G_{\mathbf{k},\lambda_1}(\xi_l + \omega_n) G_{\mathbf{k}+\mathbf{q},\lambda_2}(\xi_l + \alpha_m) G_{\mathbf{k},\lambda_3}(\xi_l) \\
 & \quad F_{\lambda_2\lambda_1}(\mathbf{q}) F_{\lambda_2\lambda_3}^*(\mathbf{q}) v_{\lambda_3\lambda_1} v_{\lambda_5\lambda_6} \\
 & \quad \times V_{s_2,s_3,s_6,s_5}(\mathbf{k}, \alpha_m) G_{\mathbf{k}'+\mathbf{q},\lambda_4}(\xi'_l + \alpha_m) G_{\mathbf{k}',\lambda_5}(\xi'_l + \omega_n) G_{\mathbf{k}',\lambda_6}(\xi'_l) F_{\lambda_4\lambda_6}(\mathbf{q}) F_{\lambda_4\lambda_5}^*(\mathbf{q}) \\
 & \sum_{l,l',m} V_{s_1,s_2,s_4,s_5}(\mathbf{q}, \alpha_m) G_{\mathbf{k},\lambda_1}(\xi_l + \omega_n) G_{\mathbf{k}+\mathbf{q},\lambda_2}(\xi_l + \alpha_m + \omega_n) G_{\mathbf{k},\lambda_3}(\xi_l) \\
 & \quad F_{\lambda_2\lambda_1}(\mathbf{q}) F_{\lambda_2\lambda_3}^*(\mathbf{q}) v_{\lambda_3\lambda_1} v_{\lambda_5\lambda_6} \\
 & \quad \times V_{s_2,s_3,s_6,s_5}(\mathbf{q}, \alpha_m + \omega_n) G_{\mathbf{k}'+\mathbf{q},\lambda_4}(\xi'_l + \alpha_m + \omega_n) G_{\mathbf{k}',\lambda_5}(\xi'_l + \omega_n) G_{\mathbf{k}',\lambda_6}(\xi'_l) \\
 & \quad F_{\lambda_4\lambda_6}(\mathbf{q}) F_{\lambda_4\lambda_5}^*(\mathbf{q})
 \end{aligned} \tag{5.17}$$

Here G is the electron Green's function given by $G_{\mathbf{k},\lambda_n}(\xi_l) = \frac{1}{\xi_l - \epsilon_{\mathbf{k},\lambda_n}}$.

5.3 Momentum Frequency Summation (ξ_l)

Having obtained the form of the electron Green's function, the l summation is readily performed by the residue theorem. We can do this, up to a point, for any general system, by writing down general transition matrix elements and general energy bands. The calculations are straightforward, but long and cumbersome, so we will only show the calculations for diagrams two and three from figure 5.3, purely for pedagogical purposes.

5.3.1 Diagrams two and three

Next we will consider the single loop diagrams with the interaction on the left and right hand sides together. These two terms are particularly symmetric and so it is most convenient to proceed in this way. First, the left hand side interaction diagram has the Green's function

$$\begin{aligned} & \sum_l V G_{\mathbf{k},\lambda_1}(\xi_l + \omega_n) G_{\mathbf{k}+\mathbf{q},\lambda_2}(\xi_l + \alpha_m + \omega_n) \\ & \times G_{\mathbf{k},\lambda_3}(\xi_l + \omega_n) G_{\mathbf{k},\lambda_4}(\xi_l) F_{\lambda_2\lambda_1}(\mathbf{q}) F_{\lambda_2\lambda_3}^*(\mathbf{q}) v_{\lambda_3\lambda_4} v_{\lambda_4\lambda_1} \end{aligned} \quad (5.18)$$

The Green's functions can be written in integral form as (dropping the subscripts for ω_n and α_l)

$$\int dz \left(\frac{1}{z + \omega - \epsilon_{\mathbf{k},\lambda_1}} \right) \left(\frac{1}{z + \alpha + \omega - \epsilon_{\mathbf{k}+\mathbf{q},\lambda_2}} \right) \left(\frac{1}{z + \omega - \epsilon_{\mathbf{k},\lambda_3}} \right) \left(\frac{1}{z - \epsilon_{\mathbf{k},\lambda_4}} \right) \quad (5.19)$$

Which has residues

$$\begin{aligned} & n_F(\epsilon_{\mathbf{k},\lambda_1}) \left(\frac{1}{\epsilon_{\mathbf{k},\lambda_1} - \epsilon_{\mathbf{k}+\mathbf{q},\lambda_2} + \alpha} \right) \left(\frac{1}{\epsilon_{\mathbf{k},\lambda_1} - \epsilon_{\mathbf{k},\lambda_3}} \right) \left(\frac{1}{\epsilon_{\mathbf{k},\lambda_1} - \epsilon_{\mathbf{k},\lambda_4} - \omega} \right) \\ & n_F(\epsilon_{\mathbf{k}+\mathbf{q},\lambda_2}) \left(\frac{1}{\epsilon_{\mathbf{k}+\mathbf{q},\lambda_2} - \epsilon_{\mathbf{k},\lambda_1} - \alpha} \right) \left(\frac{1}{\epsilon_{\mathbf{k}+\mathbf{q},\lambda_2} - \epsilon_{\mathbf{k},\lambda_3} - \alpha} \right) \left(\frac{1}{\epsilon_{\mathbf{k}+\mathbf{q},\lambda_2} - \epsilon_{\mathbf{k},\lambda_4} - \omega - \alpha} \right) \\ & n_F(\epsilon_{\mathbf{k},\lambda_3}) \left(\frac{1}{\epsilon_{\mathbf{k},\lambda_3} - \epsilon_{\mathbf{k},\lambda_1}} \right) \left(\frac{1}{\epsilon_{\mathbf{k},\lambda_3} - \epsilon_{\mathbf{k}+\mathbf{q},\lambda_2} + \alpha} \right) \left(\frac{1}{\epsilon_{\mathbf{k},\lambda_3} - \epsilon_{\mathbf{k},\lambda_4} - \omega} \right) \\ & n_F(\epsilon_{\mathbf{k},\lambda_4}) \left(\frac{1}{\epsilon_{\mathbf{k},\lambda_4} - \epsilon_{\mathbf{k},\lambda_1} + \omega} \right) \left(\frac{1}{\epsilon_{\mathbf{k},\lambda_4} - \epsilon_{\mathbf{k}+\mathbf{q},\lambda_2} + \alpha + \omega} \right) \left(\frac{1}{\epsilon_{\mathbf{k},\lambda_4} - \epsilon_{\mathbf{k},\lambda_3} + \omega} \right) \end{aligned} \quad (5.20)$$

And the Green's function for the right hand side interaction diagram is

$$\begin{aligned} & \sum_l V G_{\mathbf{k},\lambda_1}(\xi_l + \omega_n) G_{\mathbf{k}+\mathbf{q},\lambda_2}(\xi_l) \\ & \times G_{\mathbf{k},\lambda_3}(\xi_l + \alpha_m) G_{\mathbf{k},\lambda_4}(\xi_l) F_{\lambda_3\lambda_2}(\mathbf{q}) F_{\lambda_3\lambda_4}^*(\mathbf{q}) v_{\lambda_1\lambda_2} v_{\lambda_4\lambda_1} \end{aligned} \quad (5.21)$$

The Green's functions can be written in integral form as (again, dropping the subscripts for ω_n and α_l)

$$\int dz \left(\frac{1}{z + \omega - \epsilon_{\mathbf{k}, \lambda_1}} \right) \left(\frac{1}{z - \epsilon_{\mathbf{k}, \lambda_2}} \right) \left(\frac{1}{z + \alpha_m - \epsilon_{\mathbf{k}+\mathbf{q}, \lambda_3}} \right) \left(\frac{1}{z - \epsilon_{\mathbf{k}, \lambda_4}} \right) \quad (5.22)$$

Which has residues

$$\begin{aligned} & n_F(\epsilon_{\mathbf{k}, \lambda_1}) \left(\frac{1}{\epsilon_{\mathbf{k}, \lambda_1} - \epsilon_{\mathbf{k}, \lambda_2} - \omega} \right) \left(\frac{1}{\epsilon_{\mathbf{k}, \lambda_1} - \epsilon_{\mathbf{k}+\mathbf{q}, \lambda_3} - \omega + \alpha} \right) \left(\frac{1}{\epsilon_{\mathbf{k}, \lambda_1} - \epsilon_{\mathbf{k}, \lambda_4} - \omega} \right) \\ & n_F(\epsilon_{\mathbf{k}, \lambda_2}) \left(\frac{1}{\epsilon_{\mathbf{k}, \lambda_2} - \epsilon_{\mathbf{k}, \lambda_1} + \omega} \right) \left(\frac{1}{\epsilon_{\mathbf{k}, \lambda_2} - \epsilon_{\mathbf{k}+\mathbf{q}, \lambda_3} + \alpha} \right) \left(\frac{1}{\epsilon_{\mathbf{k}, \lambda_2} - \epsilon_{\mathbf{k}, \lambda_4}} \right) \\ & n_F(\epsilon_{\mathbf{k}+\mathbf{q}, \lambda_3}) \left(\frac{1}{\epsilon_{\mathbf{k}+\mathbf{q}, \lambda_3} - \epsilon_{\mathbf{k}, \lambda_1} - \alpha + \omega} \right) \left(\frac{1}{\epsilon_{\mathbf{k}+\mathbf{q}, \lambda_3} - \epsilon_{\mathbf{k}, \lambda_2} - \alpha} \right) \left(\frac{1}{\epsilon_{\mathbf{k}+\mathbf{q}, \lambda_3} - \epsilon_{\mathbf{k}, \lambda_4} - \alpha} \right) \\ & n_F(\epsilon_{\mathbf{k}, \lambda_4}) \left(\frac{1}{\epsilon_{\mathbf{k}, \lambda_4} - \epsilon_{\mathbf{k}, \lambda_1} + \omega} \right) \left(\frac{1}{\epsilon_{\mathbf{k}, \lambda_4} - \epsilon_{\mathbf{k}, \lambda_2}} \right) \left(\frac{1}{\epsilon_{\mathbf{k}, \lambda_4} - \epsilon_{\mathbf{k}+\mathbf{q}, \lambda_3} + \alpha} \right) \end{aligned} \quad (5.23)$$

Now, in order to match up the transition matrix element indices, for the second of these diagrams, set $2 \rightarrow 1, 3 \rightarrow 2, 4 \rightarrow 3, 1 \rightarrow 4$, so we have then,

$$\begin{aligned} & n_F(\epsilon_{\mathbf{k}, \lambda_1}) \left(\frac{1}{\epsilon_{\mathbf{k}, \lambda_1} - \epsilon_{\mathbf{k}, \lambda_4} + \omega} \right) \left(\frac{1}{\epsilon_{\mathbf{k}, \lambda_1} - \epsilon_{\mathbf{k}+\mathbf{q}, \lambda_2} + \alpha} \right) \left(\frac{1}{\epsilon_{\mathbf{k}, \lambda_1} - \epsilon_{\mathbf{k}, \lambda_3}} \right) \\ & n_F(\epsilon_{\mathbf{k}+\mathbf{q}, \lambda_2}) \left(\frac{1}{\epsilon_{\mathbf{k}+\mathbf{q}, \lambda_2} - \epsilon_{\mathbf{k}, \lambda_4} - \alpha + \omega} \right) \left(\frac{1}{\epsilon_{\mathbf{k}+\mathbf{q}, \lambda_2} - \epsilon_{\mathbf{k}, \lambda_1} - \alpha} \right) \left(\frac{1}{\epsilon_{\mathbf{k}+\mathbf{q}, \lambda_2} - \epsilon_{\mathbf{k}, \lambda_3} - \alpha} \right) \\ & n_F(\epsilon_{\mathbf{k}, \lambda_3}) \left(\frac{1}{\epsilon_{\mathbf{k}, \lambda_3} - \epsilon_{\mathbf{k}, \lambda_4} + \omega} \right) \left(\frac{1}{\epsilon_{\mathbf{k}, \lambda_3} - \epsilon_{\mathbf{k}, \lambda_1}} \right) \left(\frac{1}{\epsilon_{\mathbf{k}, \lambda_3} - \epsilon_{\mathbf{k}+\mathbf{q}, \lambda_2} + \alpha} \right) \\ & n_F(\epsilon_{\mathbf{k}, \lambda_4}) \left(\frac{1}{\epsilon_{\mathbf{k}, \lambda_4} - \epsilon_{\mathbf{k}, \lambda_1} - \omega} \right) \left(\frac{1}{\epsilon_{\mathbf{k}, \lambda_4} - \epsilon_{\mathbf{k}+\mathbf{q}, \lambda_2} - \omega + \alpha} \right) \left(\frac{1}{\epsilon_{\mathbf{k}, \lambda_4} - \epsilon_{\mathbf{k}, \lambda_3} - \omega} \right) \end{aligned} \quad (5.24)$$

Combining the two equations then, and concentrating on the $n_F(\epsilon_{\mathbf{k},\lambda_i})$ terms, we have

$$\begin{aligned}
 & n_F(\epsilon_{\mathbf{k},\lambda_1}) \left(\frac{1}{\epsilon_{\mathbf{k},\lambda_1} - \epsilon_{\mathbf{k}+\mathbf{q},\lambda_2} + \alpha} \right) \left(\frac{1}{\epsilon_{\mathbf{k},\lambda_1} - \epsilon_{\mathbf{k},\lambda_3}} \right) \left(\frac{1}{\epsilon_{\mathbf{k},\lambda_1} - \epsilon_{\mathbf{k},\lambda_4} + \omega} + \frac{1}{\epsilon_{\mathbf{k},\lambda_1} - \epsilon_{\mathbf{k},\lambda_4} - \omega} \right) \\
 & n_F(\epsilon_{\mathbf{k},\lambda_3}) \left(\frac{1}{\epsilon_{\mathbf{k},\lambda_3} - \epsilon_{\mathbf{k}+\mathbf{q},\lambda_2} + \alpha} \right) \left(\frac{1}{\epsilon_{\mathbf{k},\lambda_3} - \epsilon_{\mathbf{k},\lambda_1}} \right) \left(\frac{1}{\epsilon_{\mathbf{k},\lambda_3} - \epsilon_{\mathbf{k},\lambda_4} + \omega} + \frac{1}{\epsilon_{\mathbf{k},\lambda_3} - \epsilon_{\mathbf{k},\lambda_4} - \omega} \right) \\
 & n_F(\epsilon_{\mathbf{k},\lambda_4}) \left(\frac{1}{\epsilon_{\mathbf{k},\lambda_4} - \epsilon_{\mathbf{k},\lambda_1} \pm \omega} \right) \left(\frac{1}{\epsilon_{\mathbf{k},\lambda_4} - \epsilon_{\mathbf{k}+\mathbf{q},\lambda_2} + \alpha \pm \omega} \right) \left(\frac{1}{\epsilon_{\mathbf{k},\lambda_4} - \epsilon_{\mathbf{k},\lambda_3} \pm \omega} \right)
 \end{aligned} \tag{5.25}$$

And for the $n_F(\epsilon_{\mathbf{k}+\mathbf{q},\lambda_i})$ terms, we have

$$\begin{aligned}
 & n_F(\epsilon_{\mathbf{k}+\mathbf{q},\lambda_2}) \left(\frac{1}{\epsilon_{\mathbf{k}+\mathbf{q},\lambda_2} - \epsilon_{\mathbf{k},\lambda_1} - \alpha} \right) \left(\frac{1}{\epsilon_{\mathbf{k}+\mathbf{q},\lambda_2} - \epsilon_{\mathbf{k},\lambda_3} - \alpha} \right) \left(\frac{1}{\epsilon_{\mathbf{k}+\mathbf{q},\lambda_2} - \epsilon_{\mathbf{k},\lambda_4} - \alpha \pm \omega} \right) \\
 & = n_F(\epsilon_{\mathbf{k}+\mathbf{q},\lambda_2}) \left(\frac{1}{\epsilon_{\mathbf{k},\lambda_1} - \epsilon_{\mathbf{k},\lambda_3}} \right) \left(\frac{1}{\epsilon_{\mathbf{k}+\mathbf{q},\lambda_2} - \epsilon_{\mathbf{k},\lambda_4} - \alpha \pm \omega} \right) \\
 & \times \left(\frac{1}{\epsilon_{\mathbf{k}+\mathbf{q},\lambda_2} - \epsilon_{\mathbf{k},\lambda_1} - \alpha} - \frac{1}{\epsilon_{\mathbf{k}+\mathbf{q},\lambda_2} - \epsilon_{\mathbf{k},\lambda_3} - \alpha \pm \omega} \right) \\
 & = n_F(\epsilon_{\mathbf{k}+\mathbf{q},\lambda_2}) \left(\frac{1}{\epsilon_{\mathbf{k},\lambda_1} - \epsilon_{\mathbf{k},\lambda_3}} \right) \\
 & \times \left[\left(\frac{1}{\epsilon_{\mathbf{k},\lambda_1} - \epsilon_{\mathbf{k},\lambda_4} \pm \omega} \right) \left(\frac{1}{\epsilon_{\mathbf{k}+\mathbf{q},\lambda_2} - \epsilon_{\mathbf{k},\lambda_1} - \alpha} - \frac{1}{\epsilon_{\mathbf{k}+\mathbf{q},\lambda_2} - \epsilon_{\mathbf{k},\lambda_4} - \alpha \pm \omega} \right) \right. \\
 & \left. - \left(\frac{1}{\epsilon_{\mathbf{k},\lambda_3} - \epsilon_{\mathbf{k},\lambda_4} \pm \omega} \right) \left(\frac{1}{\epsilon_{\mathbf{k}+\mathbf{q},\lambda_2} - \epsilon_{\mathbf{k},\lambda_3} - \alpha} - \frac{1}{\epsilon_{\mathbf{k}+\mathbf{q},\lambda_2} - \epsilon_{\mathbf{k},\lambda_4} - \alpha \pm \omega} \right) \right]
 \end{aligned} \tag{5.26}$$

Now, looking at the second and fourth terms of this last expression:

$$\begin{aligned}
 & \left(\frac{1}{\epsilon_{\mathbf{k},\lambda_1} - \epsilon_{\mathbf{k},\lambda_3}} \right) \left(\frac{1}{\epsilon_{\mathbf{k}+\mathbf{q},\lambda_2} - \epsilon_{\mathbf{k},\lambda_4} - \alpha \pm \omega} \right) \\
 & \times \left(\frac{1}{\epsilon_{\mathbf{k},\lambda_3} - \epsilon_{\mathbf{k},\lambda_4} \pm \omega} - \frac{1}{\epsilon_{\mathbf{k},\lambda_1} - \epsilon_{\mathbf{k},\lambda_4} \pm \omega} \right) \\
 & = \left(\frac{1}{\epsilon_{\mathbf{k},\lambda_1} - \epsilon_{\mathbf{k},\lambda_4} \pm \omega} \right) \left(\frac{1}{\epsilon_{\mathbf{k},\lambda_3} - \epsilon_{\mathbf{k},\lambda_4} \pm \omega} \right) \left(\frac{1}{\epsilon_{\mathbf{k}+\mathbf{q},\lambda_2} - \epsilon_{\mathbf{k},\lambda_4} - \alpha \pm \omega} \right)
 \end{aligned} \tag{5.27}$$

Combining the $n_F(\epsilon_{\mathbf{k},\lambda_i})$ and $n_F(\epsilon_{\mathbf{k}+\mathbf{q},\lambda_i})$ terms, we get

$$\begin{aligned}
 F_{\lambda_2\lambda_1}(\mathbf{q})F_{\lambda_2\lambda_3}^*(\mathbf{q})v_{\lambda_3\lambda_4}v_{\lambda_4\lambda_1} & \left[\left(\frac{1}{\epsilon_{\mathbf{k},\lambda_1} - \epsilon_{\mathbf{k},\lambda_3}} \right) \left(\frac{1}{\epsilon_{\mathbf{k},\lambda_1} - \epsilon_{\mathbf{k},\lambda_4} \pm \omega} \right) Q^{21}(\mathbf{q}, \alpha_m) \right. \\
 & - \left(\frac{1}{\epsilon_{\mathbf{k},\lambda_1} - \epsilon_{\mathbf{k},\lambda_3}} \right) \left(\frac{1}{\epsilon_{\mathbf{k},\lambda_3} - \epsilon_{\mathbf{k},\lambda_4} \pm \omega} \right) Q^{23}(\mathbf{q}, \alpha_m) \\
 & \left. + \left(\frac{1}{\epsilon_{\mathbf{k},\lambda_1} - \epsilon_{\mathbf{k},\lambda_4} \pm \omega} \right) \left(\frac{1}{\epsilon_{\mathbf{k},\lambda_3} - \epsilon_{\mathbf{k},\lambda_4} \pm \omega} \right) Q^{24}(\mathbf{q}, \alpha_m \pm \omega_n) \right]
 \end{aligned} \tag{5.28}$$

All five diagrams can be calculated following the same procedure. Before writing down the final result however, we need to determine the form factors (transition matrix elements) for graphene specifically.

5.4 Form Factor Determination

Up until now, the calculation has been for any general multiband system with non-trivial transition matrix elements. We are interested in terms like that in equation 5.28 but with the specific transition matrix elements of Dirac graphene. For single layer graphene, these non-trivial form factors are given by

$$\begin{aligned}
 F_{\lambda_i\lambda_j}(\mathbf{q})F_{\lambda_k\lambda_l}^*(\mathbf{q}) &= (1 \quad \lambda_i e^{-i\phi(\mathbf{k}+\mathbf{q})}) \begin{pmatrix} 1 \\ \lambda_j e^{i\phi(\mathbf{k})} \end{pmatrix} \\
 &\times (1 \quad \lambda_k e^{i\phi(\mathbf{k}+\mathbf{q})}) \begin{pmatrix} 1 \\ \lambda_l e^{-i\phi(\mathbf{k})} \end{pmatrix} \\
 &= (1 + \lambda_i \lambda_j e^{-i\Delta})(1 + \lambda_k \lambda_l e^{i\Delta}) \\
 &= 1 + \lambda_i \lambda_j \lambda_k \lambda_l + \lambda_i \lambda_j e^{-i\Delta} + \lambda_k \lambda_l e^{i\Delta}
 \end{aligned} \tag{5.29}$$

Where $\Delta = \phi(\mathbf{k} + \mathbf{q}) - \phi(\mathbf{k})$. There are eight possible band combinations if $\lambda_i = \lambda$:

$$\begin{aligned}
 F_{\lambda\lambda}(\mathbf{q})F_{\lambda\lambda}^*(\mathbf{q}) &= \frac{1}{2}(1 + \cos \Delta) \\
 F_{\lambda\lambda}(\mathbf{q})F_{\lambda-\lambda}^*(\mathbf{q}) &= \frac{1}{2}i \sin \Delta \\
 F_{\lambda\lambda}(\mathbf{q})F_{-\lambda\lambda}^*(\mathbf{q}) &= \frac{1}{2}i \sin \Delta \\
 F_{\lambda-\lambda}(\mathbf{q})F_{\lambda\lambda}^*(\mathbf{q}) &= -\frac{1}{2}i \sin \Delta \\
 F_{\lambda\lambda}(\mathbf{q})F_{-\lambda-\lambda}^*(\mathbf{q}) &= \frac{1}{2}(1 + \cos \Delta) \\
 F_{\lambda-\lambda}(\mathbf{q})F_{\lambda-\lambda}^*(\mathbf{q}) &= \frac{1}{2}(1 - \cos \Delta) \\
 F_{\lambda-\lambda}(\mathbf{q})F_{-\lambda\lambda}^*(\mathbf{q}) &= \frac{1}{2}(1 - \cos \Delta) \\
 F_{\lambda-\lambda}(\mathbf{q})F_{-\lambda-\lambda}^*(\mathbf{q}) &= -\frac{1}{2}i \sin \Delta
 \end{aligned} \tag{5.30}$$

Which in general can be described by

$$F_{ij}(\mathbf{q})F_{kl}^*(\mathbf{q}) = \frac{1}{2}Z_{ijkl}(1 + ije^{i\Delta}) \tag{5.31}$$

Where $Z_{ijk\dots} = \Re(\Im)$ if $ijk\dots = 1(-1)$. Also, note that $Q^{-i-j}(\mathbf{q}, x) = Q^{ij}(\mathbf{q}, -x)$, and $Q^{i-j}(\mathbf{q}, x) = Q^{-ij}(\mathbf{q}, -x)$. The other term to consider is the current matrix elements of the velocity operator

$$\begin{aligned}
 v_{\lambda_i\lambda_j} &= \langle \mathbf{k}, i | \frac{\partial H}{\partial \mathbf{k}} | \mathbf{k}, j \rangle \\
 &= \frac{v}{2} \begin{pmatrix} 1 & \lambda_i e^{-i\phi(\mathbf{k})} \\ 1 & 0 \end{pmatrix} \begin{pmatrix} 0 & 1 \\ 1 & 0 \end{pmatrix} \begin{pmatrix} 1 \\ \lambda_j e^{i\phi(\mathbf{k})} \end{pmatrix} \\
 &= \frac{1}{2}(\lambda_i e^{-i\phi(\mathbf{k})} + \lambda_j e^{i\phi(\mathbf{k})}) \\
 &= \cos \phi(\mathbf{k}) \quad (\lambda_i = \lambda_j = 1) \\
 &= -\cos \phi(\mathbf{k}) \quad (\lambda_i = \lambda_j = -1) \\
 &= -i \sin \phi(\mathbf{k}) \quad (\lambda_i = -\lambda_j = 1) \\
 &= i \sin \phi(\mathbf{k}) \quad (\lambda_i = -\lambda_j = -1)
 \end{aligned} \tag{5.32}$$

This can also be described quite generally by

$$v_{ij} = Z_{ij} j e^{i\Delta} \quad (5.33)$$

Proceeding with these factors then, we now need only calculate the momentum transfer summation.

5.5 Momentum Transfer Summations (α_m)

Before calculating the interaction summation, it is worth establishing some rules for the boson and fermion distribution functions, as well as summations over density fluctuations:

Firstly

$$\begin{aligned} n_F(x) &= \frac{1}{e^{\beta x} + 1} = \frac{e^{-\beta x} + 1 - 1}{1 + e^{-\beta x}} = 1 - n_F(-x) \\ n_B(x) &= \frac{1}{e^{\beta x} - 1} = \frac{e^{-\beta x} - 1 + 1}{1 - e^{-\beta x}} = -1 - n_B(-x) \end{aligned} \quad (5.34)$$

Also, for systems with symmetric subbands, the density fluctuation is given by

$$\begin{aligned} Q^{s,s'}(x) &= \sum_{s,s'} \frac{n_F(s'\epsilon_{\mathbf{k}+\mathbf{q}}) - n_F(s\epsilon_{\mathbf{k}})}{s'\epsilon_{\mathbf{k}+\mathbf{q}} - s\epsilon_{\mathbf{k}} - x} \\ &= \sum_{s,s'} \frac{1 - n_F(-s'\epsilon_{\mathbf{k}+\mathbf{q}}) - (1 - n_F(-s\epsilon_{\mathbf{k}}))}{s'\epsilon_{\mathbf{k}+\mathbf{q}} - s\epsilon_{\mathbf{k}} + x} \\ &= \sum_{s,s'} \frac{-(n_F(-s'\epsilon_{\mathbf{k}+\mathbf{q}}) - n_F(-s\epsilon_{\mathbf{k}}))}{-(-s'\epsilon_{\mathbf{k}+\mathbf{q}} - (-s)\epsilon_{\mathbf{k}} + x)} \\ &= Q^{-s,-s'}(-x) \end{aligned} \quad (5.35)$$

Since $s, s' = \pm 1$. On integration, the indices s, s' become irrelevant here and so $\int Q(x) = \int Q(-x)$. However, if we impose this condition, then we must switch all $s, s' \rightarrow -s, -s'$ in the form factors. The only ones that make a difference are in the filling factors such that the following transformations must be adopted:

$$\begin{aligned} n_B(\epsilon_{\mathbf{k}+\mathbf{q}} - \epsilon_{\mathbf{k}}) &= N_q \rightarrow -1 - N_q \\ n_F(\epsilon_{\mathbf{k}+\mathbf{q}} - \epsilon_{\mathbf{k}}) &= n_q \rightarrow 1 - N_q \end{aligned} \quad (5.36)$$

Finally, we will define some shorthand notation

$$\begin{aligned} Q(\mathbf{q}, \omega_{LO}) &= Q_0 \\ Q(\mathbf{q}, \omega_n \pm \omega_{LO}) &= Q_{\pm} \end{aligned} \quad (5.37)$$

To proceed with the momentum transfer (m) summation, we cannot use the residue method because the interactions are dressed (they have continuous poles rather than simple singular poles). We use the method adopted by Perel and Eliashberg (47), which essentially leads to the relation

$$\begin{aligned} \frac{1}{\beta} \sum_m \phi(\alpha_m) \psi(\alpha_m + \omega_n) &= \frac{P}{2\pi i} \int dx H(x) \\ &\times \left((\phi^+(x) - \phi^-(x)) \psi^+(x + \omega_n) + \phi^+(x + \omega_n) (\psi^+(x) - \psi^-(x)) \right) \end{aligned} \quad (5.38)$$

Where $\phi(x)^{\pm} = \phi(x \pm i\eta)$, with $\eta \rightarrow 0$, can be any combination of products of $Q(x)$ and $V(x)$ terms, and $H(x)$ is the Bose-Einstein distribution function.

$$\begin{aligned} f(\omega_n) &= \sum_m \phi(\alpha_m) \psi(\alpha_m + \omega_n) \\ &= \int dx \coth(x/2) (\phi^+(x) - \phi^-(x)) \psi^+(x + \omega_n) + \phi^+(x + \omega_n) (\psi^+(x) - \psi^-(x)) \end{aligned} \quad (5.39)$$

Where $\phi^{\pm} = \phi(x \pm i\eta)$ with $\eta \rightarrow 0$. The final step will be the sum over n , which will simply be the analytic continuation of ω_n . With all these rules in place, we can write down the Green's function for the five diagrams shown in figure 5.3 with effective interactions as given by equation 5.16. The result is given in the next section.

5.6 Results and Discussions

We now have the final result for the electron-phonon scattering effect on the optical conductivity of Dirac graphene. The contribution is given by

$$\sigma(\omega) = \sigma_0(\omega) \left[1 + \frac{I(\omega)}{\omega} \right] \quad (5.40)$$

Where

$$I(\omega) = \int \frac{d\mathbf{q}}{(2\pi)^2} \frac{iP}{2\pi} \int dx n_B\left(\frac{\beta x}{\hbar}\right) F(x, \mathbf{q}) \quad (5.41)$$

In which

$$\begin{aligned} F(x, \mathbf{q}) = & 16 \sum_{s,s'} \left[\frac{1}{4\pi^2} \int d\mathbf{k} \left[-(1 + ss' \cos \Delta) \right. \right. \\ & \times \left(\frac{\cos \phi_{\mathbf{k}+\mathbf{q}} \cos \phi_{\mathbf{k}}}{\omega^2} + \frac{(4s' \epsilon_{\mathbf{k}} \epsilon_{\mathbf{k}+\mathbf{q}} - \omega^2) \sin \phi_{\mathbf{k}+\mathbf{q}} \sin \phi_{\mathbf{k}}}{(4\epsilon_{\mathbf{k}}^2 + \omega^2)(4\epsilon_{\mathbf{k}+\mathbf{q}}^2 + \omega^2)} \right) \\ & + \sin \Delta \left(\frac{\cos \phi_{\mathbf{k}+\mathbf{q}} \sin \phi_{\mathbf{k}}}{(4\epsilon_{\mathbf{k}}^2 + \omega^2)} - \frac{\sin \phi_{\mathbf{k}+\mathbf{q}} \cos \phi_{\mathbf{k}}}{(4\epsilon_{\mathbf{k}+\mathbf{q}}^2 + \omega^2)} \right) \\ & + \frac{1}{4} \left[\frac{(1 + ss' \cos \Delta)^2 \cos \phi_{\mathbf{k}}^2}{\omega^2} + \frac{\sin^2 \Delta \sin \phi_{\mathbf{k}}^2}{4\epsilon_{\mathbf{k}}^2 + \omega^2} \right] \\ & \times V(\mathbf{q}, a + \omega)^+ Q^{s's}(\mathbf{q}, a + \omega)^+ \left. \right] \left(V(\mathbf{q}, a)^+ Q^{s's}(\mathbf{q}, a)^+ - V(\mathbf{q}, a)^- Q^{s's}(\mathbf{q}, a)^- \right) \\ & + \frac{1}{4\pi^2} \int d\mathbf{k} \left((1 + ss' \cos \Delta) \right. \\ & \times \left(ss' \frac{\cos \phi_{\mathbf{k}+\mathbf{q}} \cos \phi_{\mathbf{k}}}{\omega^2} - ss' \frac{(4s' \epsilon_{\mathbf{k}} \epsilon_{\mathbf{k}+\mathbf{q}} + \omega^2) \sin \phi_{\mathbf{k}+\mathbf{q}} \sin \phi_{\mathbf{k}}}{(4\epsilon_{\mathbf{k}}^2 + \omega^2)(4\epsilon_{\mathbf{k}+\mathbf{q}}^2 + \omega^2)} - \frac{\cos \phi_{\mathbf{k}}^2}{\omega^2} \right) \\ & + (1 - ss' \cos \Delta) \sin \phi_{\mathbf{k}}^2 \frac{(4\epsilon_{\mathbf{k}}^2 - \omega^2)}{(4\epsilon_{\mathbf{k}}^2 + \omega^2)^2} \\ & - \sin \Delta \left(\frac{\cos \phi_{\mathbf{k}+\mathbf{q}} \sin \phi_{\mathbf{k}}}{(4\epsilon_{\mathbf{k}}^2 + \omega^2)} - \frac{\sin \phi_{\mathbf{k}+\mathbf{q}} \cos \phi_{\mathbf{k}}}{(4\epsilon_{\mathbf{k}+\mathbf{q}}^2 + \omega^2)} - 2ss' \frac{\sin \phi_{\mathbf{k}} \cos \phi_{\mathbf{k}}}{(4\epsilon_{\mathbf{k}}^2 + \omega^2)} \right) \left. \right) \\ & \times \left((V(\mathbf{q}, a)^+ - V(\mathbf{q}, a)^-) Q^{s's}(\mathbf{q}, a + \omega)^+ + (Q^{s's}(\mathbf{q}, a)^+ - Q^{s's}(\mathbf{q}, a)^-) V(\mathbf{q}, a + \omega)^+ \right) \\ & - \frac{1}{64\pi^4} \left[\int d\mathbf{k} \left(\frac{(1 + ss' \cos \Delta)^2 \cos \phi_{\mathbf{k}}^2}{\omega^2} + \frac{(4\epsilon_{\mathbf{k}}^2 - \omega^2) \sin^2 \Delta \sin \phi_{\mathbf{k}}^2}{(4\epsilon_{\mathbf{k}}^2 + \omega^2)^2} \right) \right. \\ & \times \left((V(\mathbf{q}, a)^+ - V(\mathbf{q}, a)^-) V(\mathbf{q}, a + \omega)^+ Q^{s's}(\mathbf{q}, a + \omega)^+ \right. \\ & \left. \left. + (V(\mathbf{q}, a)^+ Q^{s's}(\mathbf{q}, a)^+ - V(\mathbf{q}, a)^- Q^{s's}(\mathbf{q}, a)^-) V(\mathbf{q}, a + \omega)^+ \right) \right] \quad (5.42) \end{aligned}$$

Where $\Delta = \phi(\mathbf{k} + \mathbf{q}) - \phi(\mathbf{k})$, and

$$Q^{s's}(\mathbf{q}, a) = \frac{n_F(\epsilon_{\mathbf{k}+\mathbf{q},s'}) - n_F(\epsilon_{\mathbf{k},s})}{\epsilon_{\mathbf{k}+\mathbf{q},s'} - \epsilon_{\mathbf{k},s} - a} \quad (5.43)$$

The form given by equation (5.42) is cumbersome, but readily calculated numerically. The electron-phonon interaction strength for LO-phonons is well known, and is given by $M^2 \approx 0.035/4$ for small q , in our dimensionless units, which are normalized by v_F (1).

In figure 5.5 we present the correction to the optical conductivity which can be attributed to scattering by screened electron-phonon interactions. Firstly, we point out that the difference between the screened results and the unscreened results is negligible. Therefore, the effective interaction given in equation (5.16) can be approximated by the bare electron-phonon interaction with almost no loss of precision. The spectra contains both interband and intraband terms. For an intrinsic sample, these are characterised by a resonant and continuous spectrum respectively.

Both the continuum (intraband) and resonant (interband) spectra are shown in figure 5.5(a). The 30K results are shown in the inset due to their low magnitude. At 30K it can be seen that the primary interband term ($\omega = \omega_{LO}$) is relatively strong, but the multi-phonon processes are negligible. For temperatures $> 100K$, the continuum results dominate so strongly that the resonant terms cannot be seen. At room temperature, it can be seen that the correction to the universal conductivity due to electron-phonon scattering is as much as $0.2\sigma_0$. The resonant (interband) spectrum is shown in figure 5.5(b), and contains terms at $\omega = n\omega_{LO}/3$ where $n = [1, 4]$. The $n = 1$ peak is barely noticeable in the figure, but can become quite prominent at higher temperatures. However, the magnitudes in figure 5.5(b) are negligible, with the continuum spectrum shown in figure 5.5(a) vastly dominating for all but the lowest ($T < 100K$) and highest ($T > 500K$) temperatures.

The temperature dependence of the continuum and resonant peaks at $\omega = \omega_{LO}/2$ and $\omega = \omega_{LO}$ respectively is shown in figure 5.6. It can be seen in (a) that with increasing temperature there is an increased phonon population that facilitates both intra- and inter-band transitions, and so the relationship is roughly

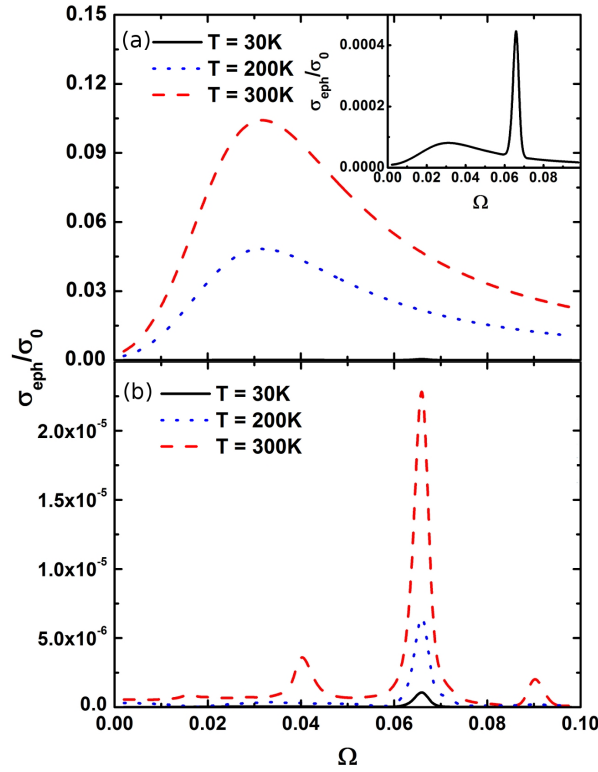


Figure 5.5: The electron-phonon scattering mediated conductivity of graphene. In (a) we present both the intraband and interband contributions. It is found that for $T > 100\text{K}$ the intraband contributions dominate. The $T = 30\text{K}$ results are shown in the inset due to their relatively small magnitude. In (b) we show the interband part which is shown to have several multi-phonon processes, but the magnitude of this contribution is relatively negligible except at very low and very high temperatures.

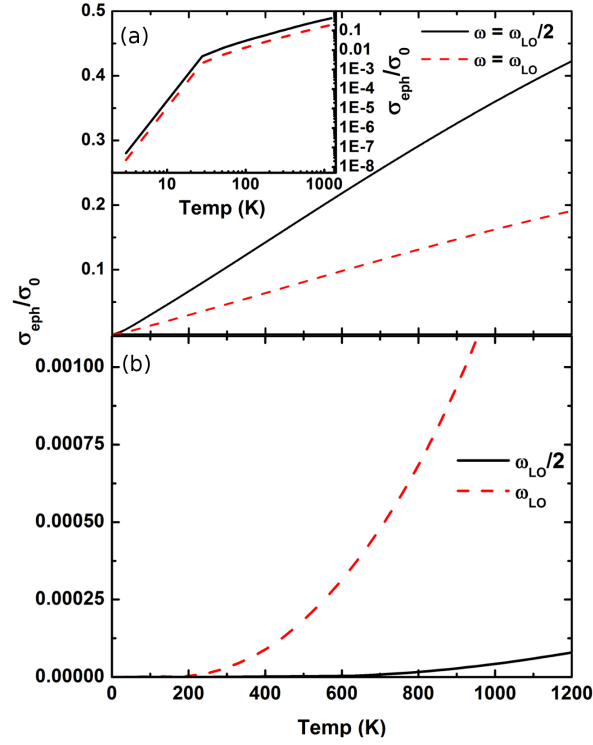


Figure 5.6: The temperature dependence of the magnitude of the conductivity at $\omega = \omega_{LO}/2$ (the continuum peak), and $\omega = \omega_{LO}$, (the dominant resonant peak) from figure 5.5. In (a) we show the inter- and intraband contributions together and obtain a roughly linear relationship. When plotted in log-log form (inset), we see that there is a significant ‘kink’ at $T \approx 30$ K. When considering only interband transitions as in (b), both peaks display an exponential temperature dependence.

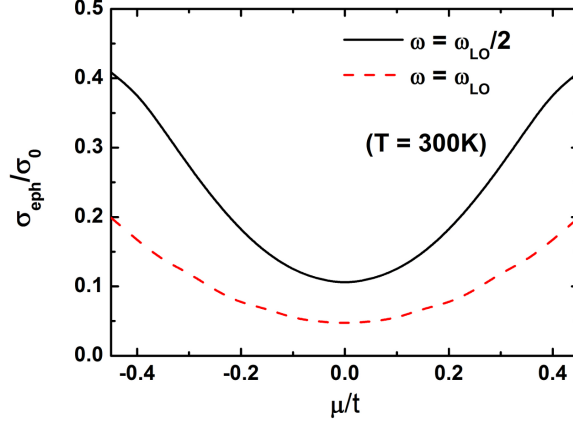


Figure 5.7: The two dominant response peaks increase in magnitude for doped samples, and are symmetric about zero doping due to electron-hole symmetry. This can be attributed to the increased availability of intraband transitions, which are the dominant mechanism.

linear with increasing temperature. In the inset to figure 5.6(a) we show the log-log relationship of the same data, and it can be seen that there is a significant kink at $T \approx 30\text{K}$, above which the roughly linear increase slows somewhat. In figure 5.6(b) we present the temperature dependence of the interband part of the same two dominant peaks. It can be seen that the resonant peak at $\omega = \omega_{\text{LO}}$ increases exponentially with temperature, with the interband part of the continuum peak doing the same, only much more slowly. The interband transitions then, follow an exponential increase in transition rates, whereas the intraband transitions (which are the most dominant) are roughly linear. This explains the condition that interband terms dominate at both high and low temperatures as the linear relationship will, in general, cross the exponential one at two distinct points.

It is worth noting that the qualitative behavior of the phonon scattering mediated conductance is similar at different doping levels. The continuum and resonant structures are essentially identical, however the interband terms also adopt a continuum as well as a resonant structure at finite doping. This is due to the peculiar gapless and linear band-structure of low energy graphene. The doping dependence of the continuum and resonant peaks are shown in figure 5.7, and are

not suprisingly shown to increase with increasing doping magnitude. This is due to the extra availability of intraband transitions. Due to electron-hole symmetry, the doping dependence is symmetric about $\mu = 0$.

5.7 Conclusion

In this chapter we have studied the effect of electron-LO-phonon interaction on the high frequency conductivity of graphene in the regime of massless Dirac fermion. The correction due the LO phonon scattering to the universal optical conductivity of graphene has been calculated which can be as much as 20% at room temperature. The scattering conductivity is dominated by a continuum intraband spectrum which displays a peak at $\omega = \omega_{LO}/2$. We have found that the effect of screening (within the RPA approximation) is insignificant, and that the electron-phonon interaction can be approximately described by a bare phonon propagator. This greatly simplifies calculations, and is in good agreement with the dominant consensus within the field.

It was noted that there are also resonant interband terms observed at $\omega = n\omega_{LO}/3$ where $n = [1, 4]$, which represent single and multi-phonon processes. The single phonon process $\omega = \omega_{LO}$ is dominant over the continuum results only at $T < 50K$, beyond which the continuum results vastly dominate. However it should be noted that the results for $T < 50K$ are extremely small, at around $\sigma_0/1000$ or less.

The temperature and doping dependence of these results was also investigated, and it was found that the spectra scale roughly linearly with increasing temperature, and also increase with doping magnitude. The doping dependence was found to be symmetric about $\mu = 0$ due to electron-hole symmetry.

In conclusion, we have presented a qualitative and quantitative result on the electron-LO phonon interaction in graphene under the massless Dirac fermion approximation. The temperature and frequency dependence of the electron-LO-phonon scattering mediated conductivity has been obtained and various multi-phonon processes have been identified.

Conclusion

It is pertinent at this stage to make some concluding remarks. The optical properties of *intrinsic* graphene-based systems have here been calculated in some detail. We have considered various geometries for flat graphene systems (ie. we have ignored entirely systems such as carbon nanotubes and buckey balls), and performed calculations within the tight-binding approximation.

The relevance of the tight-binding approximation is quite well established. Nevertheless, there has been some first-principles calculations performed over the past couple of years which show that various optical and electronic properties of graphene may deviate from the tight-binding approximation by around 10%. In particular, these calculations incorporate excitonic effects, which can alter the band-gaps in both 2D and 1D graphene. These corrections will not significant alter the two order of magnitude enhancement observed in Dirac bilayer ribbons, but may become significant for smaller scale results, or band-structure specific results. Questions of particular import in this context are: Will the roton mode observed in some non-Dirac armchair ribbons survive the transition to first principles calculations? Will the strong nonlinear response observed in 2D graphene, which is so dependent on the linear bandstructure, survive this same transition? We suspect the answers to these questions will be ‘yes’! Nevertheless, they must be asked, and at the end of the day, experiment will resolve the matter once-and-for-all.

Furthermore, the intrinsic approximation deserves some attention. Graphene is renowned for being a remarkably defect-free material. The electron-electron coupling is amazingly small in most cases, making screening effects relatively unimportant. However, defects such as rippling have been shown to be extremely important, and have resolved more than one outstanding discrepancy between

theory and experiment. For this reason, defects are important, and, in the case of effects such as rippling, perhaps must even be considered part of an ‘intrinsic’ system. The expected effect of defects is, again, small. But the same questions must be asked as before, particularly in the context of relatively ‘small’ or delicate results. And once again, experiments will end any outstanding dispute.

With these two points in mind, we can say that we have thoroughly investigated the optical properties of intrinsic graphene-based systems within the tight-binding regime. The optical properties of these systems have been shown to be remarkably versatile and, at times, suprisingly strong. They are tunable by stretching, cutting at various widths and along different chiral angles, layering, and heating or cooling. It is expected that, as a result of these predictions, further experimental work will be carried out with the final goal being the incorporation of these materials into future photonic devices.

We have also predicted a roton-like mode in the collective excitation spectrum of some non-Dirac armchair graphene nanoribbons. This mode is the first mode of its kind seen since superfluid Helium over 50 years ago. It is expected to shed some light on the physics of rotons, and will undoubtedly have various fascinating consequences that will be revealed in the coming years.

The set of remarkable properties of graphene-based systems has, once again, expanded into new fields of investigation. Graphene is truly a multi-disciplinary material, being researched in many different fields for various potential applications. The optical and superfluid-like properties of graphene represent yet two more potential fields of significant research and application.

A sensible research direction from here which uses the results of this thesis as a starting point is the optical properties of disordered graphene systems. The role of disorder in graphene is currently being studied by several groups, but the specific application to the optical properties of graphene based materials remains open. There have been sufficiently significant predictions that have emerged from this work that warrant confirmation and extension into the theory of disorder. Furthermore, the role of disorder within the context of the roton minimum would be particularly interesting, as the roton-like behaviour begs the question of the presence of vortices (or at least their 1D equivalent) and bulk-edge coupling, both of which are strongly affected by disorder.

Finally, it is worth mentioning that some further work has been completed since the initial submission of this thesis. We have demonstrated some unusual electronic properties of semi-hydrogenated single and bi-layer graphene with variable sized A- or B-hydrogenated domains. We find that the band gap scales linearly with the ratio of the number of A- to B-hydrogenated atoms, reaching zero gap in the case of a single layer at $N_A = N_B$, and at $N_A = 0$ for a bilayer, but independent of the domain size. We also found that the phase at $N_A = N_B$ is an insulator with zero band gap. We confirm this gapless insulator by the zero optical conductance at low frequencies. This gapless insulator is a curious state of matter which ensures robust transport properties and even long term state retention. This work is currently under review for publication in *Physical Review Letters*.

Bibliography

- [1] A. C. Neto, F. Guinea, N. Peres, K. Novoselov, and A. Geim, Rev. Mod. Phys. **81**, 109 (2009). iv, v, 1, 2, 4, 6, 7, 9, 10, 104
- [2] A. Geim, Science **324**, 1530 (2009). 1, 2, 4
- [3] A. K. Geim and K. S. Novoselov, Nature Materials **6**, 183 (2007). 1, 2, 38
- [4] S. Iijima, Nature **354**, 56 (1991). 1
- [5] K. Novoselov *et al.*, Science **306**, 666 (2004). 1
- [6] P. R. Wallace, Phys. Rev **71**, 622 (1947). 1, 19
- [7] J. C. Slonczewski and P. R. Weiss, Phys. Rev. **109**, 272 (1958). 1
- [8] J. W. McClure, Phys. Rev. **108**, 612 (1957). 1
- [9] K. Novoselov *et al.*, Nature **438**, 197 (2005). 2
- [10] Y. Zhang, Y. Tan, H. Stormer, and P. Kim, Nature (London) **438**, 201 (2005). 2
- [11] H. Suzuura and T. Ando, Phys. Rev. Lett **89**, 266603 (2002). 2
- [12] S. Morozov *et al.*, Phys. Rev. Lett. **97**, 016801 (2006). 2
- [13] D. Khveshchenko, Phys. Rev. Lett. **97**, 36801 (2006). 2
- [14] M. Muller, J. Schmalian, and L. Fritz, Phys. Rev. Lett. **103** (2009). 2
- [15] A. C. Neto, F. Guinea, and N. Peres, Physics World **19**, 33 (2006). 2

- [16] M. I. Katsnelson and K. S. Novoselov, Sol. Stat. Comm. **143**, 3 (2007). 2, 5
- [17] R. R. Nair *et al.*, Science **320**, 1308 (2008). 2, 62, 64
- [18] Z. Q. Li *et al.*, Phys. Rev. Lett. **102**, 037403 (2009). 2, 52, 54, 55
- [19] A. Wright, F. Liu, and C. Zhang, Nanotechnology **20** (2009). 2
- [20] C. Zhang, L. Chen, and Z. Ma, Phys. Rev. B **77**, 241402 (2008). 2, 12, 51, 53, 69
- [21] T. Stauber, N. M. R. Peres, and A. K. Geim, Phys. Rev. B **78**, 085432 (2008). 2, 12, 53, 54, 69
- [22] S. Mikhailov and K. Ziegler, J. Phys.:Condens. Matter **20**, 384204 (2008). 2, 73
- [23] A. Wright, X. Xu, J. Cao, and C. Zhang, App. Phys. Lett. **95** (2009). 2
- [24] M. Katsnelson, K. Novoselov, and A. Geim, Nat. Phys. **2**, 620 (2006). 5
- [25] R. Laughlin, Phys. Rev. B. **23**, 5632 (1981). 8
- [26] C. Kane and E. Mele, Phys. Rev. Lett. **95**, 226801 (2005). 13
- [27] M. Ezawa, Phys. Rev. B **73**, 045432 (2006). 26
- [28] S. D. Sarma and E. Hwang, arXiv:0902.3822 . 40, 42
- [29] L. Brey and H. Fertig, Phys. Rev. B **75**, 125434 (2007). 40, 42
- [30] G. D. Mahan, *Many Particle Physics*, 3rd ed. (Kluwer Academic, New York, 2000). 41, 48, 49, 68, 92
- [31] A. Wright and C. Zhang, unpublished . 42
- [32] L. Landau, J. Phys. U.S.S.R. **5**, 71 (1941). 43
- [33] R. Feynman, Phys. Rev. **91**, 1291 (1953). 43
- [34] R. Feynman and M. Cohen, Phys. Rev. **102**, 1189 (1956). 43

- [35] S. Girvin, A. MacDonald, and P. Platzman, Phys. Rev. Lett. **54**, 581 (1985). 43
- [36] S. Girvin, A. MacDonald, and P. Platzman, Phys. Rev. B **33**, 2481 (1986). 43
- [37] Y. Barlas, R. Cote, K. Nomura, and A. H. MacDonald, Phys. Rev. Lett **101** (2008). 43
- [38] J. Yau and M. J. Stephen, Phys. Rev. Lett. **27**, 482 (1971). 43
- [39] S. Beliaev, Sov. Phys. JETP **7**, 289 (1958). 43
- [40] J. Yau and M. J. Stephen, Phys. Rev. Lett. **27**, 482 (1971). 43
- [41] K. F. Mak, C. H. Lui, J. Shan, and T. F. Heinz, Phys. Rev. Lett. **102**. 52, 54
- [42] D. S. L. Abergel and V. I. Fal'ko, Phys. Rev. B **75**, 155430 (2007). 54
- [43] W. Liao, G. Zhou, and F. Xi, J. App. Phys. **104**, 126105 (2008). 59, 60
- [44] J. Liu, A. Wright, C. Zhang, and Z. Ma, App. Phys. Lett. **93**, 041106 (2008). 59
- [45] X. Li, X. Wang, L. Zhang, S. Lee, and H. Dai, Science **319**, 1229 (2008). 60, 64
- [46] R. Saito, M. S. Dresselhaus, and G. Dresselhaus, *Physical Properties of Carbon Nanotubes*, 3rd ed. (Kluwer Academic, New York, 1998). 89
- [47] V. Perel and G. Eliashberg, Sov. Phys. JETP **14**, 633 (1962). 102